Surface Discharges of Buoyant Jets in Crossflows

by

Amir Gharavi

Thesis submitted in partial fulfillment of the requirements for the
Doctorate in Philosophy degree in Civil Engineering

Academic Advisors:

Professor Ioan Nistor and Professor Majid Mohammadian

Department of Civil Engineering

Faculty of Engineering

University of Ottawa

I would like to dedicate my thesis to my family.

My maman and baba who always supported my decisions with love and encouragement during the time I was studying abroad. My brothers, Kaveh and Navid, who are my best friends and talking to them gives me enough motivations to proceed in every step of my life. My beloved wife, Parnian, who believed in me and helped me survive a 4-year long-distance relationship.

Acknowledgment

I would like to thank my supervisors Prof. Ioan Nistor and Prof Majid Mohammadian who are like my family in Canada. Having them as my supervisors is one the best thing ever happened to me in my life. I appreciate all their support and encouragement during the past years. They helped me become a better version of myself.

I would like to thank everyone (Mark Lapointe, Tommy Rigall, Dr. Enrique Peña, Dr. José Anta and Dr. Parnian Hosseini) who helped me in the process of my research specially in the preparation of my experimental set-up.

I would like to thank all my friends (Mehdi, Ali, Ehsan, Majid, Yan, Yarzar, Sepideh, Hossein, Sanaz, Mehran, Aziz, Benyamin, Im4n and Gaven) for their emotional support.

I wanted to thank my Ph.D. thesis defense committee members, Prof. Sam Li, Prof. Paul Van Geel, Dr. Abolghasem Pilechi, Dr. Amir H. Azimi and Dr. David Knox. Additionally, I wanted to thank Dr. Ousmane Seidou and Dr. Tad Murty for being in my proposal defense.

Abstract

Understanding the physics of mixing for two fluids is a complicated problem and has always been an interesting phenomenon to study. Surface discharge is the oldest, least expensive and simplest way of discharging industrial or domestic wastewater into rivers and estuaries. Because of the lower degree of dilution in surface discharges, critical conditions are more likely to occur. Having a better understanding of the mixing phenomenon in these cases will help to predict the environmental effects more accurately. In this study, surface discharges of jets into waterbodies with or without crossflows were investigated numerically and experimentally.

Three-dimensional (3-D) Computational Fluid Dynamics (CFD) models were developed for studying the surface discharge of jets into water bodies using different turbulence models. Reynolds stress turbulence models and spatially filtered Large Eddy Simulation (LES) were used in the numerical models. The effects of inclusion of free surface water in the CFD models on the performance of the numerical model results were investigated. Numerical model results were compared with the experimental data in the literature as well as the experimental works performed in this study.

Experimental works for buoyant and non-buoyant surface discharge of jets into crossflow and stagnant water were conducted in this study. A new setup was designed and built in the Civil Engineering Hydraulics Laboratory at the University of Ottawa to perform the desired experiments. Stereoscopic Particle Image Velocimetry (Stereo-PIV) was used to measure the instantaneous spatial and temporal 3-D velocity distribution on several planes of measurement downstream of the jet with the frequency of 40 *Hz*. Averaged 3-D velocity distribution was extracted on different planes of measurement to show the transformation of the velocity vectors from a “jet-like” to a “plume-like” flow regime. Averaged 3-D velocity distribution and streamlines illustrated the flow transformation of the surface jets. Experimental results detected the formation and evolution of vortices in the surface jet’s flow structure over the measurement zone. Additional turbulent flow characteristics such as the turbulent kinetic energy (k), turbulent kinetic energy dissipation rate (ϵ), and turbulent eddy viscosity (υ_t) were calculated using the measured time history of the 3-D velocity field.

Table of Contents

List of Figures

List of Tables

List of Symbols

Roman Letters

a_0	Jet cross-sectional area	$[m^2]$
b_{ij}	Normalized anisotropy tensor	-
C	Concentration	$[kg/m^3]$
C_μ	Constant in the closure	-
C_s	Smagorinsky constant	-
D	Isotropic diffusion coefficient	$[m^2/s]$
D_{ij}	Diffusion term	$[m^2/s^3]$
D_{ij}^{ν}	Viscous diffusion	$[m^2/s^3]$
D_{ij}^{T}	Turbulent diffusion	$[m^2/s^3]$
E	Total turbulent entrainments	$[m^3/s^2]$
E_h	Horizontal entrainment rate	$[m^3/s^2]$
E_v	Vertical entrainment rate	$[m^3/s^2]$
E_p	Advected puff entrainment rate	$[m^3/s^2]$
E_f	Frontal entrainment rate	$[m^3/s^2]$
E_i	Interfacial entrainment rate	$[m^3/s^2]$
f	Focal length	$[m]$
F	Froude number	–
Fr_0'	Densimetric Froude number	–
g	Gravity acceleration	$[m/s^2]$
g'	Modified gravity acceleration	$[m/s^2]$
g_0'	Discharge buoyant acceleration	$[m/s^2]$
G	Spatial filter	–
H	Height	$[m]$
J	Buoyancy flux	$[m^3/s^3]$
k	Turbulent kinetic energy	$[m^2/s^2]$
l	Turbulent length scale	$[m]$
L_b	Plume-crossflow length scale	$[m]$

L_m	Jet-crossflow length scale	$[m]$
L_M	Jet-plume length scale	$[m]$
L_Q	Discharge length scale	$[m]$
L_T	Jet-plume-crossflow length scale	$[m]$
M	Momentum flux	$[m^4/s^2]$
p	Pressure	$\left[\frac{kg}{m\,s^2}\right]$
P_{ij}	Production term	$[m^2/s^3]$
Pr_t^{SGS}	SGS Prandtl number (or Schmidt number)	$[m^2/s]$
Q	Flow rate	$[m^3/s]$
r̂	Correlation coefficient	–
R	Crossflow parameter, velocity ratio	–
Re	Reynolds number	–
S_{ij}	Strain tensor	$[m^2/s]$
t	Time	$[s]$
T	Temperature	$[°C]$
U	Average velocity	$[m/s]$
W	Inside width of the pipe	$[m]$
X	Longitudinal geometric or length scale	$[m]$
Y	Lateral geometric or length scale	$[m]$
Z	Vertical geometric or length scale	$[m]$

Greek Letters

$\Delta\theta$	Temperature difference between ambient water and measured temperature	[℃]
Δ	Filter size	$[m]$
$\Delta\rho_0$	Discharge density difference	$[kg/s^3]$
ρ	Fluid density	$[kg/s^3]$
τ_{ij}	Viscous stress	$\left[\frac{kg}{m\,s^2}\right]$
τ_{ij}^R	Reynolds stress	$\left[\frac{kg}{m\,s^2}\right]$

μ	Molecular viscosity	$\left[\frac{kg}{m\,s}\right]$
φ	Scalar concentration	$[kg/m^3]$
ϕ_{ij}	Pressure strain rate correlation term	$[m^2/s^3]$
ϵ	Dissipation rate	$[m^2/s^3]$
ϵ_{ij}	Turbulent dissipation rate term	$[m^2/s^3]$
υ	Kinematic viscosity	$[m^2/s]$
υ_t	Turbulent eddy viscosity	$[m^2/s]$
σ_k	Closure coefficient	–
δ_{ij}	Kronecker delta	–
Ω_{ik}	Rotation rate tensor	$[m^2/s]$
Γ	Molecular diffusivity	$[m^2/s]$

Subscripts

0	Represents the parameter related to jet
a	Represents the parameter related to ambient water (or crossflow)

Abbreviations

2-D	Two-Dimensional
3-D	Three-Dimensional
ADCP	Acoustic Doppler Current Profiler
CFD	Computational Fluid Dynamics
CVP	Counter-rotating Vortex Pair
DNS	Direct Numerical Simulation
GGDH	Generalized Gradient Diffusion Hypothesis
HSV	Horseshoe-vortex
LA	Light Attenuation
LDA	Laser-Doppler Anemometry
LES	Large Eddy Simulations
LIF	Laser Induced Fluorescence
LRR	Launder, Reece and Rodi
NPDES	National Pollutant Discharge Elimination Systems

OpenFOAM	Open Field Operation and Manipulation
PIV	Particle Image Velocimetry
PLIF	Planar Laser Induced Fluorescence
PTV	Particle Tracking Velocimetry
PISO	Pressure Implicit with Splitting of Operators
RANS	Reynolds-Averaged Navier-Stokes
RLV	Ring-like vortices
RSTM	Reynolds Stress Turbulence Model
sCMOS	scientific Complementary Metal Oxide Semiconductor
SGS	Sub-Grid-Scale
Stereo	Stereoscopic
UV	Upright-vortices
WV	Wake Vortices
ZOFE	Zone Of Flow Establishment

1 Introduction and Study Objectives

1.1 Introduction and Motivation

Outfall mixing has always been an important field of study for scientists and engineers. Having a better understanding of the mixing phenomenon will help in making accurate predictions. In some cases, an accurate prediction of the mixing could prevent devastating effects on the environment. In this study, the mixing of two types of fluids is considered. Depending on the density difference of the discharging jet and receiving ambient water, three different conditions may occur: non-buoyant, negatively buoyant and positively buoyant. When the density of the discharging jet is less than the ambient water, it is called positively buoyant, and if larger, it is called negatively buoyant. Density difference is caused by changes in temperature, salinity and suspended particles in water. Warm saline discharges from desalination plants may have a lower density as a result of higher temperature compared to sea water (see Figure 1.1).

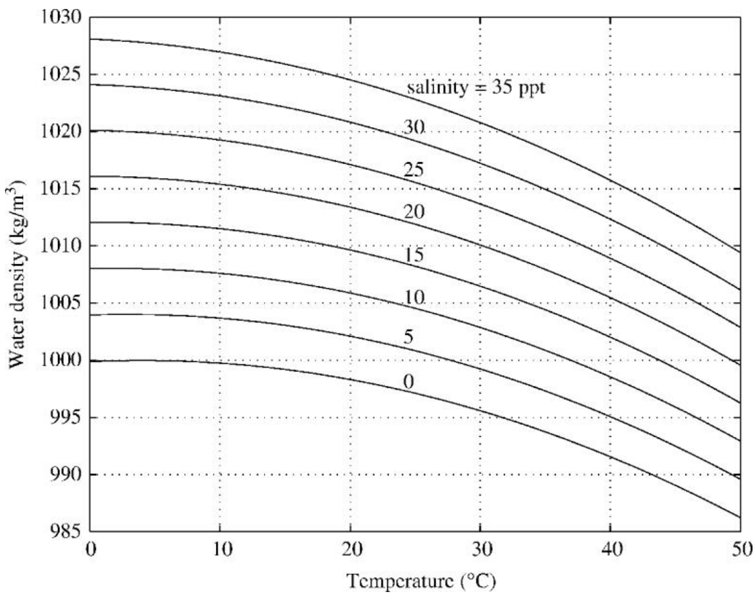

Figure 1.1 Water density changes as a function of temperature and salinity (Millero and Poisson, 1981)

A typical positively buoyant surface plume is caused by discharging cooling water from power plant outfalls via an open channel into a shoreline or a river. Figure 1.2 shows the Fujairah power and desalination plant in the United Arab Emirates as an example.

Figure 1.2 Fujairah power and desalination plant outfall discharging into Persian Gulf

In natural geophysical situations, hypoxia can be created, where a river with fresh water (lower density) is discharged into sea water (higher density). Hypoxia (dead zone) arises where a layer of fresh water (with lower density) isolates the sea water (with higher density) from the air, leading to a creation of a stratified flow with reduced oxygen level in the deeper water. One of the most famous dead zones is the Mississippi River discharge point in the Gulf of Mexico (Figure 1.3). The area inside the green dashed polyline shown in Figure 1.3 represents the dead zone.

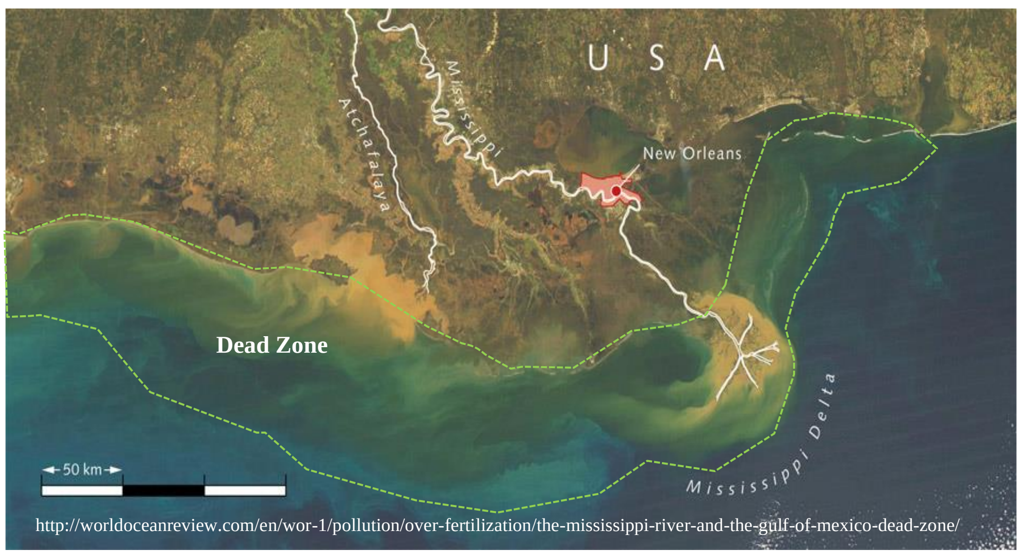

Figure 1.3 Dead zone created in the Gulf of Mexico (inside the green dashed polyline)

Surface discharges are the oldest, typically most inexpensive, and simplest way of discharging treated industrial or domestic wastewater into rivers or coastal waters. Because of a lower degree of dilution (almost 10 or less, (Jones et al., 2007)) surface discharges are not recommended by environmental codes with respect to building new surface outfalls. For example, surface discharges have some limitations, depending on their pre-treatment, in the United States based on the National Pollutant Discharge Elimination System (NPDES).

1.2 Research Objectives and Significance

As discussed in Section 1.1, the process of surface discharge is a critical issue. However, in some cases, surface discharges inevitably exist in nature along with their consequences. In order to gain a better understanding of the mixing of surface buoyant jets discharging into crossflow conditions, it is necessary to study the velocity and concentration distributions in the affected zones. This is a challenging hydrodynamic problem that many studies have considered, but several aspects still need improvement. Furthermore, an accurate method for estimating the mixing of surface jets in crossflows is crucial for prediction purposes.

In the literature, studies in this field have mainly focused on field measurements, experimental works and some entrainment models. New measurement techniques such as nonintrusive methods of measurement will help generate more accurate experimental results, which will lead to higher quality data. In this study, the performance results of Computational Fluid Dynamics (CFD) models were compared with the data measured in experimental studies and field works to evaluate the efficiency of numerical models. Therefore, this study aimed to investigate the following aspects of surface discharges of buoyant jets in crossflow:

1. Improve the understanding of the flow structure of surface jets in crossflow especially the mixing behaviour in the zones closer to the discharge point (near-field of the outfalls).
2. Perform experimental investigation into the characteristics of flow structures by conducting velocity measurements in the laboratory.
3. Study the effect of buoyancy terms by adding the required terms to turbulence models using an open-source CFD software (OpenFOAM).
4. Compare the CFD modelling results with the existing data in the literature and the experimental measurements in the current study.
5. Evaluate the efficiency of different turbulence models and report the best performing model, which has the capability of predicting the mixing behaviour of surface jets in crossflow.

6. Assess the best modelling approach in dealing with surface jets such as considering the effect of free surface conditions on mixing and entrainment.

1.3 Novelty and Contributions of the Research

Most of the studies of jets in crossflows in the literature are related to vertical buoyant jets (chimney-like). For horizontal surface jets, there have been few studies conducted. The free surface effect and the effect of buoyancy for CFD modelling of surface jets in crossflows have not been studied before in the literature. Therefore, the novelties and contributions of this study can be summarized as follows:

- Design and build the experimental setup in the Hydraulics Laboratory to measure three-dimensional (3-D) velocity distributions using Stereo-PIV.
- This is the first study measuring 3-D velocity distribution on two-dimensional (2-D) sections in the mixing zone of horizontal surface jets discharging into crossflow.
- This is the first study to consider the effect of free surface in the mixing of surface jets discharging into crossflow.
- Buoyancy modified solvers for incompressible flow were used for the CFD modelling works in OpenFOAM.
- Assess the turbulence models' performance in terms of predicting the flow structure and mixing of surface jets discharging into crossflow in CFD simulations.

1.4 Thesis Outline

This thesis includes experimental and numerical investigation of surface jets in crossflow (Figure 1.4). In Chapter 2, the background and literature related to surface jets and related topics are reviewed. The methodology of the research is described briefly in Chapter 3. This includes the details of the experimental measurement setup and procedures, as well as the aspects of numerical studies implemented in this research.

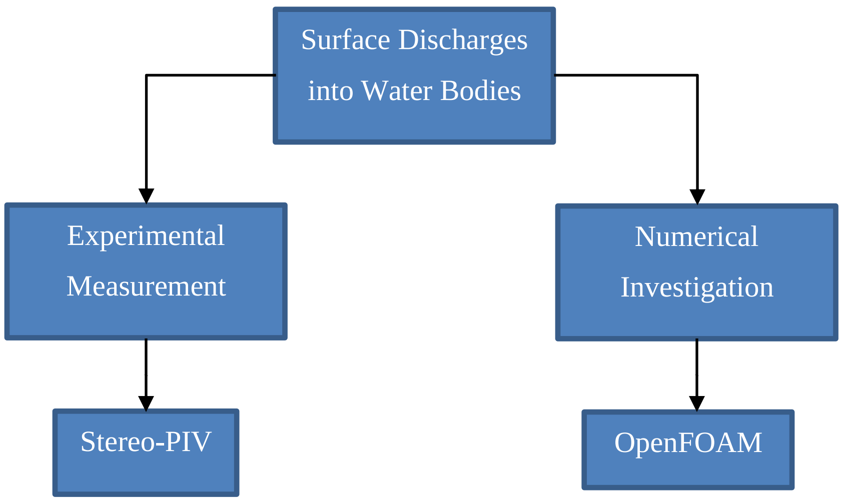

Figure 1.4 Thesis outline

Chapter 4 includes the results of the experimental works conducted in the current study for the mixing of buoyant surface jets in crossflows. Mean velocity distribution and turbulent flow characteristics such as the turbulent kinetic energy (k), turbulent kinetic energy dissipation rate (ϵ), and turbulent eddy viscosity (υ_t) were extracted from the measured experimental data. This chapter has been published in the *Journal of Environmental Fluid Mechanics* (Gharavi et al., 2020).

Chapter 5 presents the numerical investigations of the surface buoyant jets in crossflows. Two experimental cases were chosen to be examined numerically. Case 1 was related to the numerical model built to represent the experimental measurement of temperature studied by Anwar (1987). Case 2 was associated with the numerical model for the experimental works in the current thesis presented in Chapter 4. Chapter 5 is presented in the format of a technical article and will be submitted to the *Journal of Environmental Fluid Mechanics* as a continuation of the previous study published in the same journal.

Chapter 6 contains the summary of the achievements and conclusions presented in the previous chapters and recommendations for future work.

Appendix A describes the numerical and experimental study of surface buoyant jets in stagnant water. Results of the CFD model and measured velocity distributions were compared in this Appendix.

1.5 List of Publications

Journal Articles:

1. Gharavi, A., Mohammadian, A. and Nistor, I. 2022. Numerical simulations of surface discharges into crossflows. *Environ. Fluid Mech.*, (chapter 5 of the current thesis which will be submitted in a couple of weeks)

2. Gharavi, A., Mohammadian, A., Nistor, I., Peña, E. and Anta, J. 2020. Experimental study of surface buoyant jets in crossflow. *Environ. Fluid Mech.*, **20**: 1007–1030. https://doi.org/10.1007/s10652-020-09737-7

Conference Paper:

1. Gharavi, A., Mohammadian, A., Nistor, I., Qiblawey H. M., "Experimental and Numerical Study of Non-buoyant Surface Jet", *3rd International Symposium on Outfall Systems, ISOS 2016*, Ottawa, Ontario, Canada 10th to 13th May 2016.

2 Background and Literature Review

2.1 Introduction

The mixing of discharge jets into water bodies is an important field of study for hydraulic scientists and engineers because of the complicated physics of the mixing phenomenon. Several numerical and experimental studies have been accomplished to provide a better understanding of mixing processes. In this chapter, the background and literature regarding the experimental and numerical works in the mixing field are reviewed.

Surface discharges are one of the most common ways of discharging treated wastewater into water bodies. It happens in nature when a river reaches a sea or when treated wastewater is discharged into a river. Treated wastewater usually has a lower density because of its temperature, which leads to positively buoyant discharges. Unpredictable mixing of treated wastewater may destroy the habitats of aquatic species. Therefore, various studies for mixing of surface discharges have been conducted, which are reviewed in this section.

2.2 Buoyant Surface Jets

The best and most comprehensive flow classification for buoyant surface jets was introduced by Jones et al. (2007). Here, important parameters for buoyant surface discharges are introduced. Figure 2.1 shows a schematic view of the geometry for a surface jet and ambient water. Subscripts of the variables are 0 and a for the surface jet and ambient water, respectively.

2.2.1 Dimensional Analysis of Surface Buoyant Discharges

In Figure 2.1 U is the average velocity, ρ is the density of water, which is a function of salinity and temperature. b, h and a are width, height and cross-sectional area, respectively. It is assumed that the density of ambient water is relatively uniform and not stratified. Flow characteristics are described as Q_0 for jet flow rate, M_0 for jet momentum flux and J_0 for jet buoyancy flux. These parameters may be calculated as:

$$Q_0 = U_0 a_0, \qquad M_0 = Q_0 U_0, \qquad J_0 = Q_0 g_0' \tag{2.1}$$

$$g_0' = \left(\frac{\rho_a - \rho_0}{\rho_a}\right) g \tag{2.2}$$

where $a_0 = h_0\, b_0$, g_0' is reduced gravitational acceleration and g is gravitational acceleration.

Two main assumptions are considered for dimensional analysis of buoyant surface discharges into crossflow. First, viscosity effects are not considered, assuming that the discharges are fully turbulent. Second, the Boussinesq buoyancy approximation for buoyancy-driven flow is considered. The density difference between discharged jets and ambient water is small enough to cause buoyancy forces only. In addition to the flow characteristics of the discharged jet and ambient water, the geometry of the jet and receiving channel play an important role in dimensional analysis. Any flow variable, ϕ, can be described as a function of these independent variables (Jones et al., 2007)

$$\phi = f(U_0,\ U_a,\ g',\ h_0,\ b_0, BS, H, y_0, \sigma_0, \theta) \tag{2.3}$$

where, BS is ambient channel width, H is ambient water depth, y_0 is distance the discharge channel projects into ambient water, σ_0 is discharge angle and θ is ambient bottom slope angle (see Figure 2.1). Some of these independent parameters in equation (2.3) are less important or ineffective for different classifications of surface discharges.

2.2.2 Important Non-dimensional Numbers

The length scales described above may also represent two major non-dimensional parameters. The first non-dimensional parameter is the densimetric Froude number of the discharge jet, which is described as:

$$Fr_0' = \frac{U_0}{\left(g_0'\, a_0^{1/2}\right)^{1/2}} = \frac{L_M}{L_Q} \tag{2.4}$$

A higher value of densimetric Froude number represents a less buoyant jet, smaller jet size or higher velocity. The second non-dimensional parameter is the crossflow parameter, which is described as:

$$R = \frac{U_0}{U_a} = \frac{L_m}{L_Q} \tag{2.5}$$

Lower values of R denote a strong crossflow, which may bend the discharge jet. The ratio of these two non-dimensional parameters (Fr_0'/R) is written as:

$$\frac{Fr_0'}{R} = \left(\frac{L_m}{L_b}\right)^{1/2} \tag{2.6}$$

This is an important factor in determining the jet trajectory constant for free jets classification (Jones et al., 1996). In order to create a small physical model of an existing prototype of surface discharges in crossflow, it is required to have the same values for important non-dimensional numbers (Fr_0' and R). For example, if the model is 100 times smaller than the prototype, the velocities should be 10 times smaller to represent the same conditions and classifications.

2.2.3 Important Length Scales

Important length scales for flow classification are described (McCorquodale, 2007) as

$$L_Q = {Q_0}/{M_0^{1/2}} = a_0^{1/2} \tag{2.7}$$

$$L_M = {M_0^{3/4}}/{J_0^{1/2}} \tag{2.8}$$

$$L_m = {M_0^{1/2}}/{U_a} \tag{2.9}$$

$$L_b = {J_0}/{U_a^3} \tag{2.10}$$

$$L_T = {M_0^{2/3}}/{(J_0 U_a)^{1/3}} = \left[R^{1/3}\, Fr_0'^{2/3}\right] L_Q \tag{2.11}$$

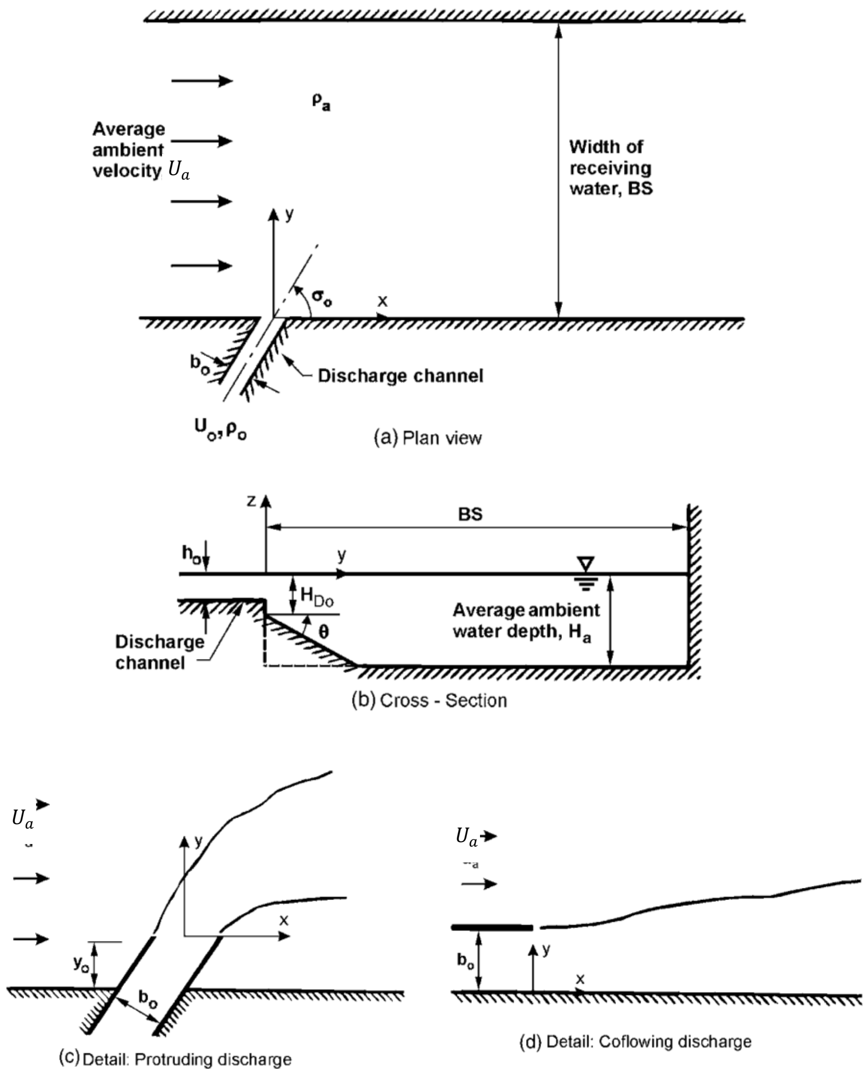

Figure 2.1 Schematic view of surface jet and ambient water (Jones et al., 2007)

where L_Q is discharge length scale (or outlet length scale), and depends on the discharge channel geometry and the zone affected by it. L_M is the jet-plume length scale, which shows the length that flow transforms from a jet (momentum dominated) to a plume (buoyancy dominated). L_M shows the location that the source of jet mixing changes from jet-like to buoyancy induced lateral spreading. L_m is the jet-crossflow length scale and indicates the length at which the jet does not control the flow, and the crossflow dominates and causes the jet to bend at this location. L_b is the plume-crossflow length scale and specifies the length of the upstream intruding flow as a result of higher velocity generated by buoyancy of the jet in the upstream direction. L_T is the jet-plume-crossflow length scale and denotes the length where momentum effects are much higher when comparing the buoyancy and crossflow effects together. Schematic views of these length scales are shown in Figure 2.2.

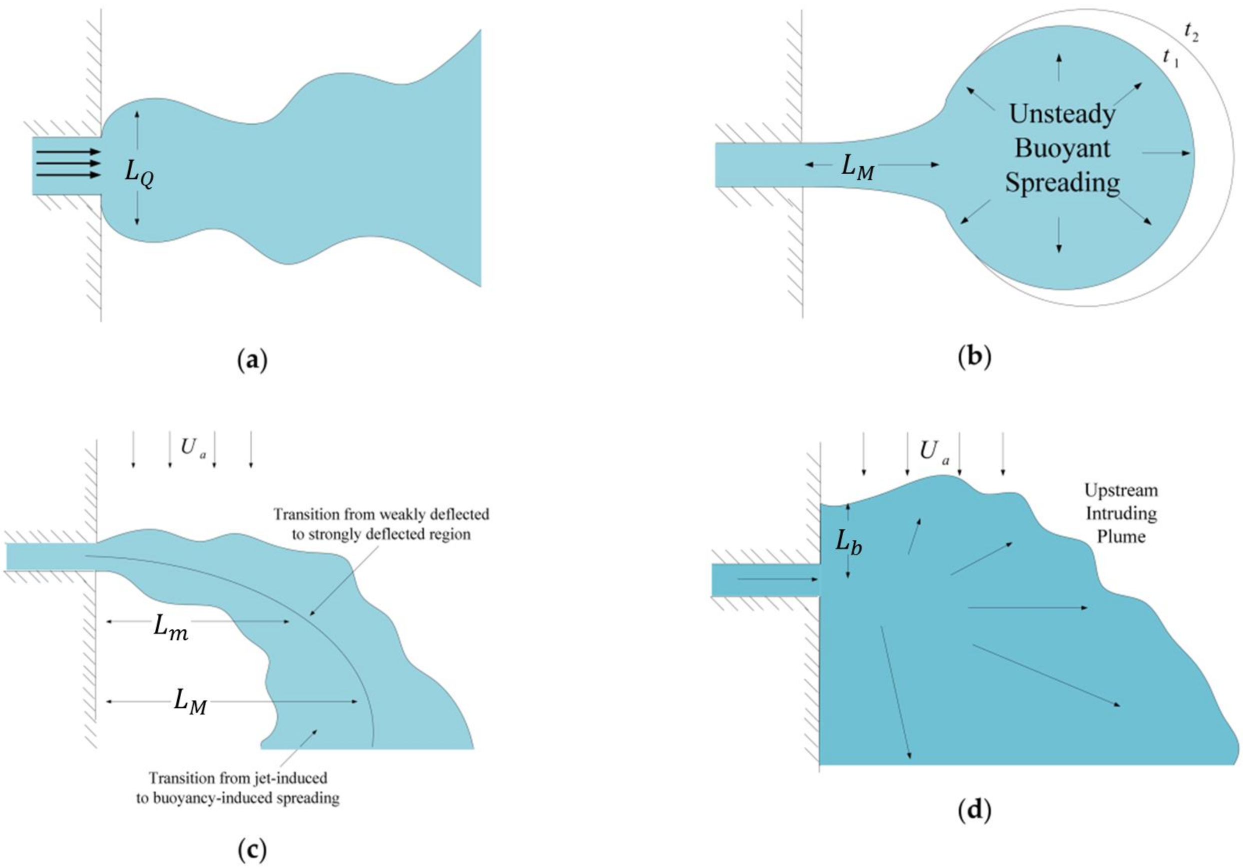

Figure 2.2 Important length scales introduced for different surface discharges into stagnant ambient water (a and b) and crossflow (c and d) (Taherian and Mohammadian, 2021)

2.2.4 Buoyant Surface Discharge Flow Classification

Four major classifications are introduced by Jones et al. (2007). These classifications are based on several different surface discharge experiments performed by scientists such as Nash and Jirka (1995), Abdelwahed (1983) and Jones (1983). Figure 2.3 shows the flow classification flowchart for surface buoyant discharges. The main classes are: free jets, shoreline attached jets, wall jets and upstream intruding plumes.

As can be seen in Figure 2.3, free jets are not dramatically affected by the crossflow, which indicates the relative stronger jet compared to crossflow. Free jets propagate into the crossflow ambient and bend gradually as they go downstream via crossflow. Free jets are the ideal condition for a surface discharge as they do not touch the shoreline. Shoreline attached jets are not as strong as free jets relative to crossflow as they bend right at the outlet of the discharge jet and touch the shoreline immediately downstream. A recirculation zone may be generated downstream of the discharge point in shoreline attached jets. Wall jets are not deflected by crossflow because of the discharge angle. Upstream intruding jets usually happen in the case of a highly buoyant jet in a crossflow with relatively low velocities. In this case, the surface jet velocity in lateral directions caused by buoyancy is relatively higher than ambient crossflow velocity. Upstream intruding jets are generated as a result of a higher lateral velocity of the jet in the upstream direction compared to crossflow velocity.

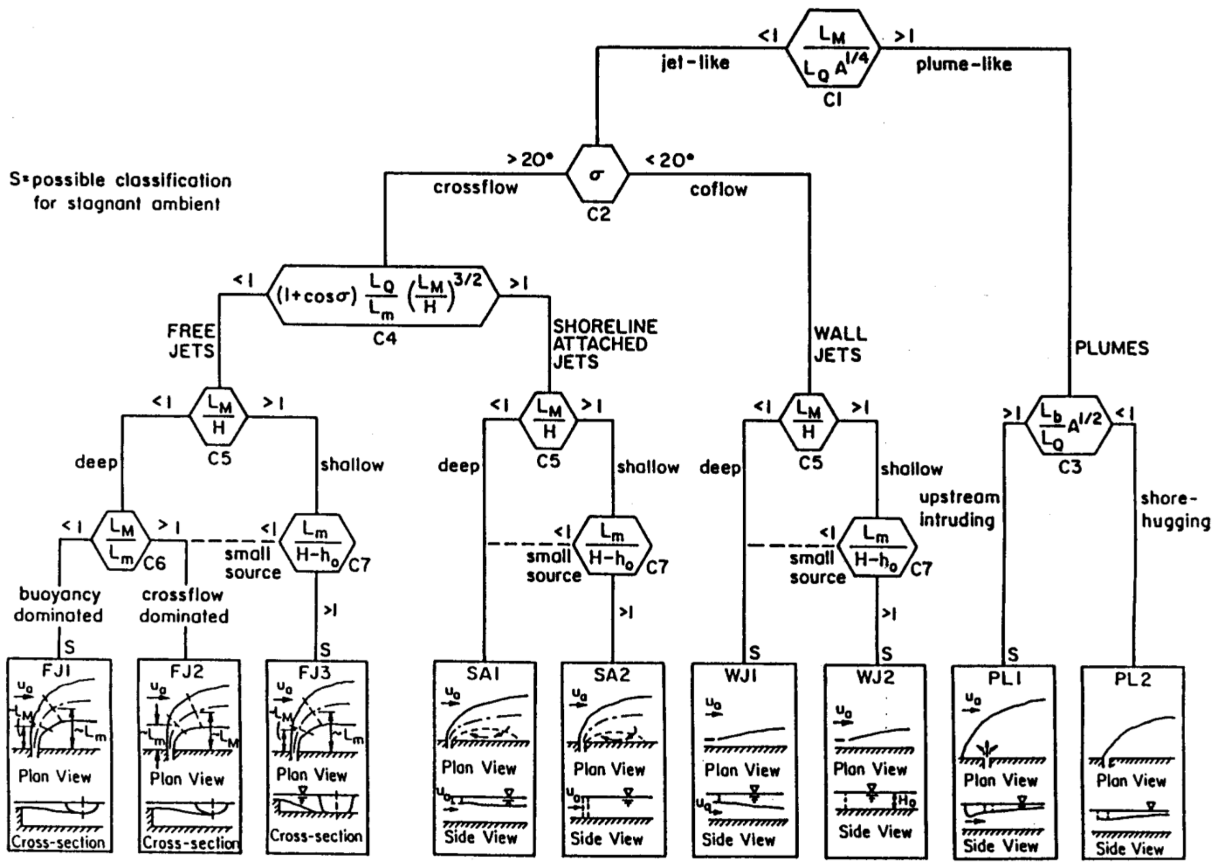

Figure 2.3 Flowchart of buoyant surface discharges flow classification (Jones et al., 2007)

2.3 Jets in Crossflow

Discharging of a steady jet in a uniform crossflow has various industrial applications. It is commonly used in smokestack exhausting, submerged diffusers of desalination plants and fuel mixing in combustion chambers. A schematic view of a jet in crossflow is shown in Figure 2.4. Jets usually discharge from a round nozzle vertically and bend due to crossflow. Jet trajectory has always been an item of interest in these cases and it could be defined as a line created by connecting the locus of maximum concentration, maximum velocity or maximum vorticity.

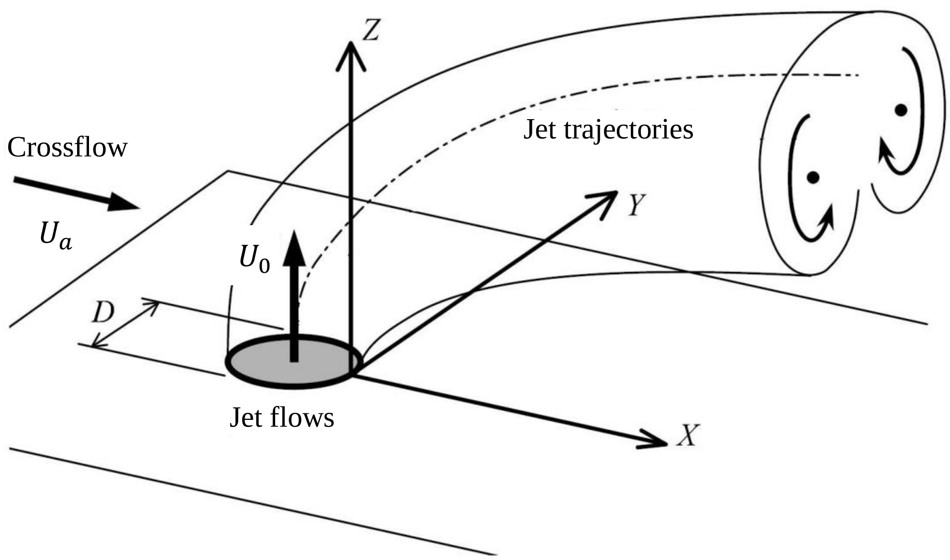

Figure 2.4 Schematic view of jet in crossflow

Jets in crossflow provide a higher mixing capability compared to free jets or mixing layers (Coussement et al., 2012a). One of the reasons is the existence of a counter-rotating vortex pair as the jet expands downstream (L. Cortelezzi and Karagozian, 2001).

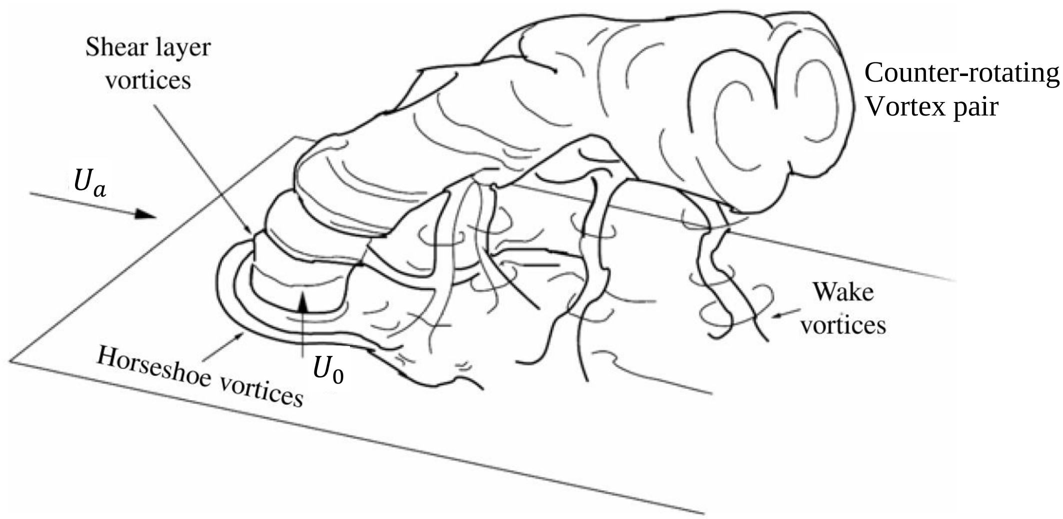

Figure 2.5 Jet in crossflow vortices (Coussement et al., 2012a)

Four major types of vortices may be generated in the discharge of jets in crossflows.

1. Counter-rotating vortex pair (CVP): the CVP is the only vortex that remains in the jet trajectory as it propagates in the ambient water, which enhances the mixing along the jet trajectory (L. Cortelezzi and Karagozian, 2001). The CVP sometimes remains in the flow structure as far as a thousand times that of the jet diameter (Keffer and Baines, 1963).
2. Horseshoe vortex: different Reynolds numbers and velocity ratios of the discharging jet create three forms of horseshoe vortex. A horseshoe vortex of a discharge jet in crossflow is identical to the one generated by a circular cylinder (Figure 2.6). A horseshoe vortex is generated as a result of the adverse pressure gradient upstream of the discharge jet.

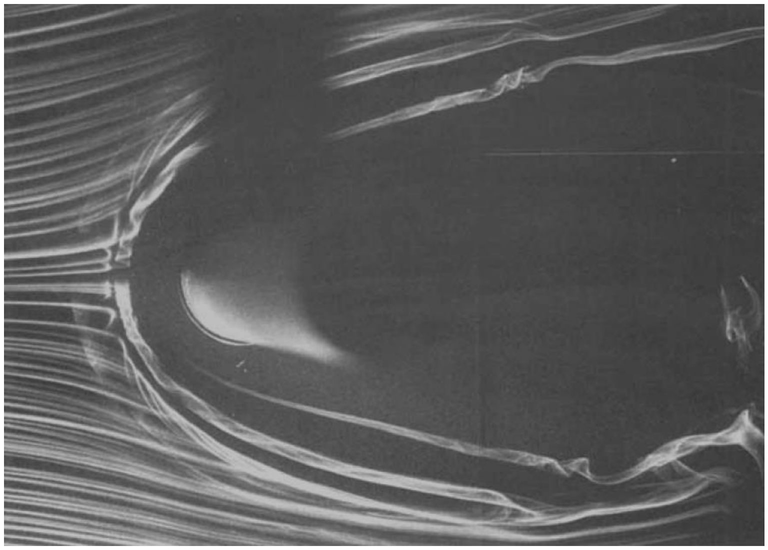

Figure 2.6 Plan view of the horseshoe vortex around a cylinder (Fric and Roshko, 1994a)

3. Shear-layer ring vortices: these vortices are generated in the boundary layer of the jet and are dominant in the initial part of the discharge. The shear-layer contains the source of CVP and generates the roll-up of the leading and trailing edges. Kelvin-Helmholtz instability will be produced during this process (Figure 2.7).

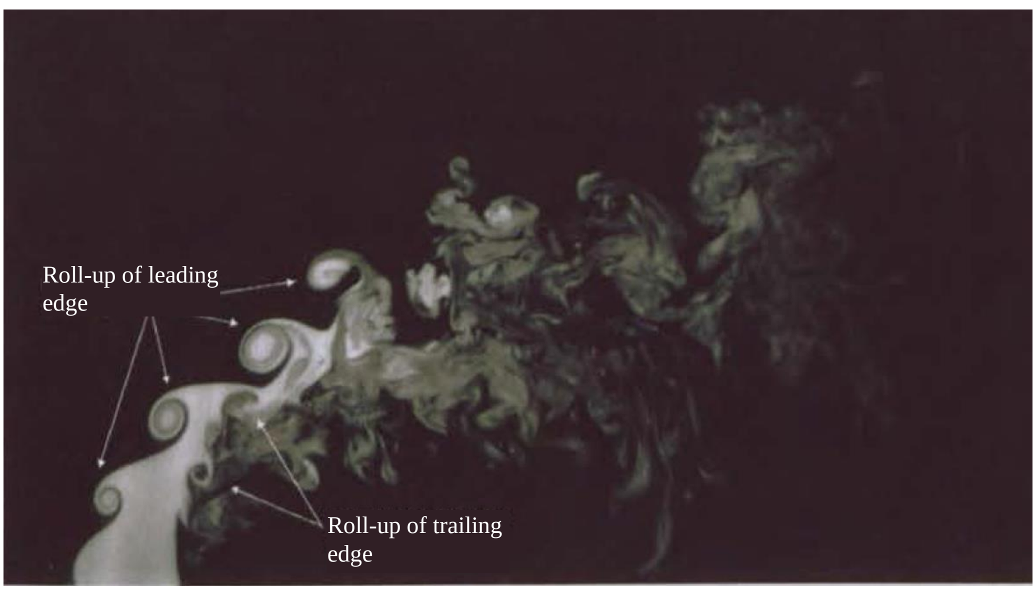

Figure 2.7 Two independent vortices in the jet shear layer structure (Cutler, 2002)

4. Wake vortices: these are the least understood and most complicated among the four types of vortices. Wake vortices generated by discharge of jets in crossflows are similar to those of the vortex shedding from a solid cylinder.

The wake vortices and the shear-layer vortices are naturally unsteady and will be eliminated from the velocity measurements by averaging over time. On the other hand, counter-rotating vortex pair and horseshoe vortices have mean flow characterization in addition to unsteady components (Fric and Roshko, 1994a).

Surface discharges of jets in crossflows have similar conditions to vertical discharges:

- Wall effects may be effective in the formation of vortices in surface discharges similar to bed effects in the vertical discharges
- Velocity ratio (R) is an important parameter in both cases

with the following differences:

- For buoyant surface discharges, gravitational force is not in the same direction as the discharge
- Water surface will change the physics of CVP as it will not be able to develop in pairs (this has been shown by Gharavi et al. (2020))

2.4 Secondary Currents in Open-Channel Bend Flows

There is a similarity between jets in crossflows (that bend) and secondary flow in open-channel bends. Secondary flow is created as a result of vertically sheared and curved flows in open channels. When the water flows into a channel bend, it will be affected by centrifugal acceleration. Water surface slope will not remain horizontal and secondary current forms in the plane normal to the mean flow (Figure 2.8). This condition is similar to surface discharge of water in crossflow as the jet bends as a result of crossflow and centrifugal acceleration and will create secondary current inside the jet structure. The main difference between open-channel bends and surface jets discharging into crossflow is that the jet is not affected by walls or bed friction.

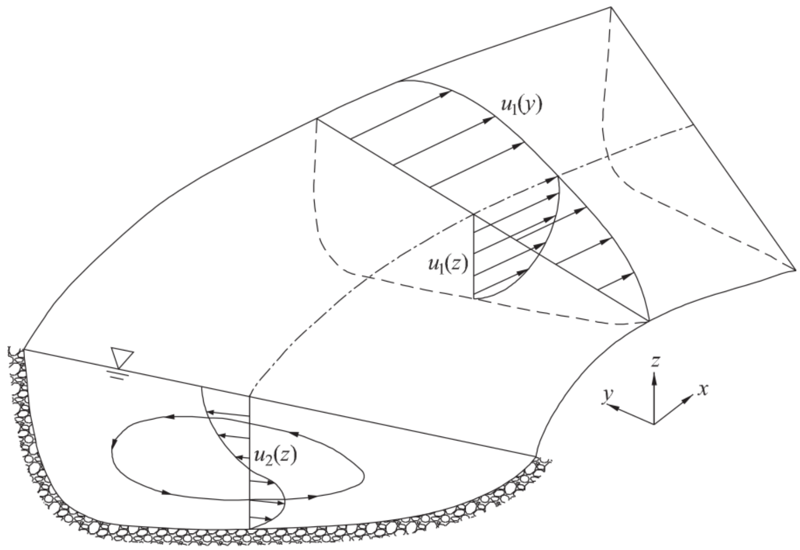

Figure 2.8 Velocity profile distributions and secondary flow in a curved open-channel (Song et al., 2012)

Another case that bears a resemblance to surface discharge of jets in crossflows is that of open-channel junctions. Junctions with sharp edges create a zone of separation immediately downstream of the discharge point in addition to the stagnation point upstream of the discharge point. The zone of separation is caused by the momentum of the lateral branch flow. The intersection between the outer edge of the jet and the crossflow creates the shear plane (Figure 2.9). A river junction is a surface discharge class of SA1 (shoreline attached jets in shallow waters (Jones et al., 2007)). In this study, the crossflow is wide enough, and the walls are far away from the discharge point to avoid reaching the outer edge of the jet.

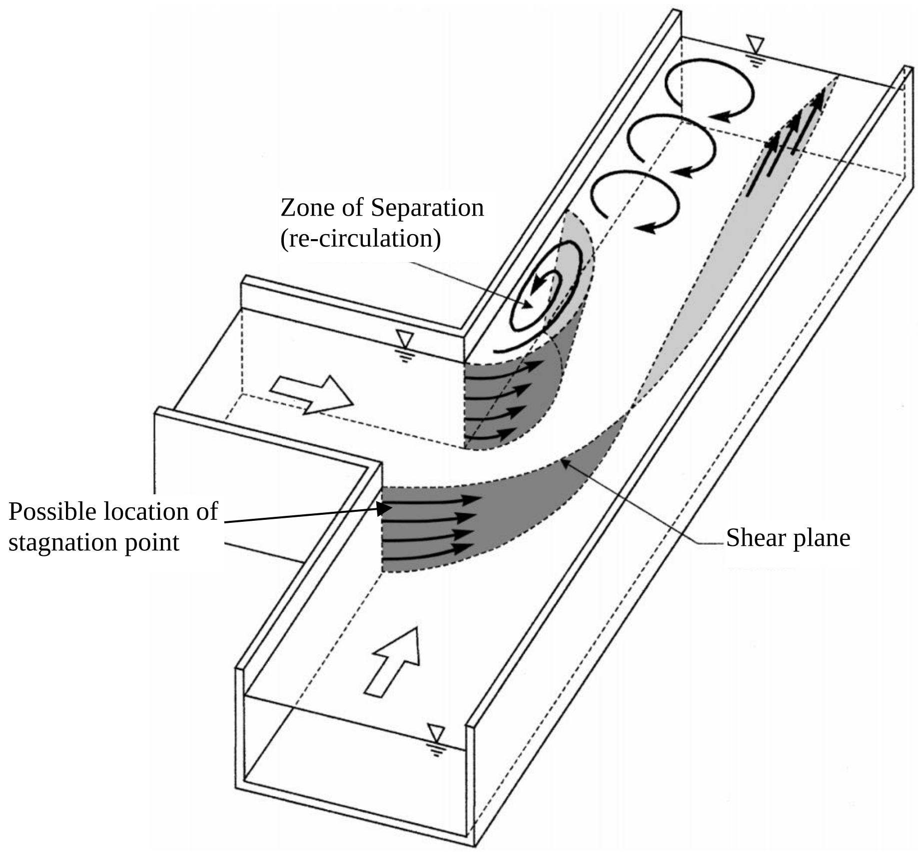

Figure 2.9 Plan view of a river junction (Weber et al., 2001)

2.5 Field Studies

Several field studies have been conducted in the literature for surface discharges such as power plants or desalination plant outfalls. Examples include the field measurements conducted by Miller and Brighouse (1984), Dunn et al. (1975) and Pilechi (2016). Recent improvements in field measuring technologies have led to the creation of new devices allowing for much easier and more accurate field measurements. Some of these devices use the Global Positioning System (GPS) to extract the exact coordinates in the field. This helps to relate the measured data to the position of the device at the time of measurement. Acoustic Doppler Current Profiler (ADCP) instruments measure the velocities of particles inside the water (assuming that the particles have the same velocity as the water current) throughout the depth of the river. ADCP calculates the velocity via the Doppler effect of sound waves scattered back from particles within the water column. In order to measure the concentration at each point in field studies, it is common to use a tracer (usually

Rhodamine WT). By using drone imaging, it is even possible to extract the jet trajectory based on dye distribution (Figure 2.10). In situ dye fluorometry extracts the dilution distribution at certain points.

Conducting field studies is usually more expensive compared to performing similar experiments in the laboratory. Fields studies are more accurate for validating the solution compared to experimental works in the sense that there is no error associated with downscaling the model. Field studies are much more difficult to conduct because of the conditions that are not controlled by humans (such as weather or water level in tidal zones). Because of changing conditions in the field, repeatability of conducting experiments in the laboratory is much easier to achieve and makes it possible to control the effective parameters and perform sensitivity analysis on the effective variables. At the same time, field measured data are the closest representation of reality.

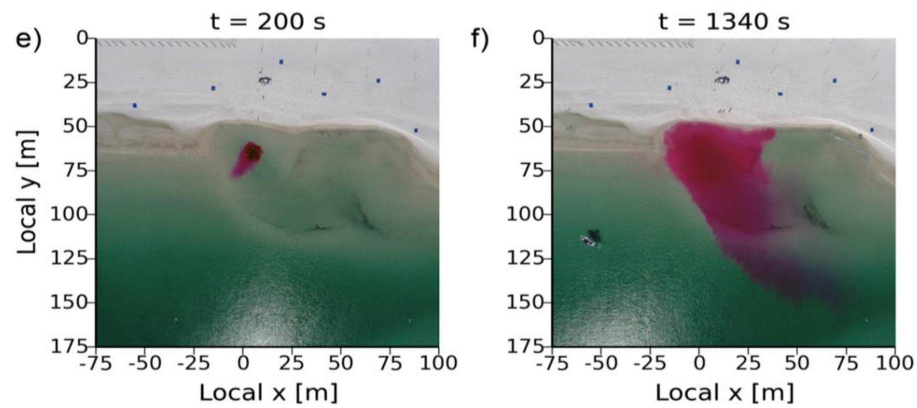

Figure 2.10 Examples of capturing surfzone kinematics on different scales (Brouwer et al., 2015)

2.6 Experimental Studies

In order to study jet mixing in water, various techniques are used to measure flow concentration and velocity distributions. When the discharges have three-dimensional mixing, it is more difficult to measure the concentration and velocity accurately. Different techniques for concentration measurements have been used such as probe sampling systems and conductivity probe systems. Pitot tubes have been used to measure mean velocity of the flow. Using other techniques such as Hot-Wire Anemometry or Laser-Doppler Anemometry (LDA) has the advantage of measuring instantaneous velocity.

Recently, optical measurement methods have become more commonly used as not only are they non-intrusive techniques to measure jet trajectory and concentration, but they can also provide measured values exactly at the same time in an area (also known as whole-flow-field technique) without any additional error caused by interpolation or extrapolation. The most commonly used optical measurement methods for concentration are Light Attenuation (LA) and Laser Induced Fluorescence (LIF). On the other hand, Particle Tracking Velocimetry (PTV) and Particle Image Velocimetry (PIV) are mainly used in the literature for velocity distribution measurements.

Various studies have been performed on jet mixing. Gawad et al. (1996a) evaluated jet trajectory distribution of a circular jet discharged into a trapezoidal channel. Their physical model included a sloped bed covered with gravel to approximate the roughness of the Detroit River. Both buoyant and non-buoyant cases were discharged at surface and in the water, leading to a total of 36 experimental tests. The velocity and concentration distributions were measured in different cross-sections. Anwar (1987) conducted experiments to measure the jet flow temperature distribution of a rectangular channel discharged perpendicular into a flow with a velocity almost equal to that of the jet. Jet temperature was set higher than the ambient water, leading to a buoyant jet. Temperature contours were extracted for different vertical and horizontal slices in the channel. Velocity profiles of different sections along the channel were also extracted.

2.7 Numerical Studies

It is essential to predict environmental impacts of new outfalls or to conduct accurate investigation of existing cases. Numerical simulations may be an inexpensive method to estimate the velocity and concentration of outfalls. Even in experimental studies, it is impossible or very costly to measure the data at every location. Additionally, it is almost impossible to have the same exact conditions in the region of interest. By improving computational capacity, it is possible to simulate three-dimensional analysis of surface jets in crossflow. Numerical simulations help to extract the results for the entire field and evaluate the mixing phenomenon accurately. Validations are necessary to ensure the results are reliable and compatible with experimental studies.

2.7.1 Jet Integral Models

The mixing of surface buoyant jets includes several complicated hydrodynamic processes. These processes are introduced here. Mixing in front of outfalls is affected by the momentum of jets. Pure jet mixing happens in this region and the jet spreads perpendicular to the jet axis due to turbulent mixing. The jet has a rounder shape in this zone, and the velocity distributions are Gaussian parallel to the surface and half Gaussian in depth (section A-A in Figure 2.11). The jet loses its momentum because of the buoyant damping as it goes further and it starts to have lateral spreading and becomes more plume-shaped with linear velocity distribution (section B-B in Figure 2.11). After the jet loses its momentum completely, a density current will be generated at the front of the jet and will continue to spread (e.g., Figure 2.12).

In addition to the above-mentioned phenomena, internal hydraulic jump may also occur. Internal hydraulic jumps are the same as hydraulic jumps but they happen in fluids with different densities. In this condition, hydraulic jump happens for super-critical flow with high speed and changes it to sub-critical flow with an increase in the depth of the mixing zone. Figure 2.13 shows the schematic of a submerged jet.

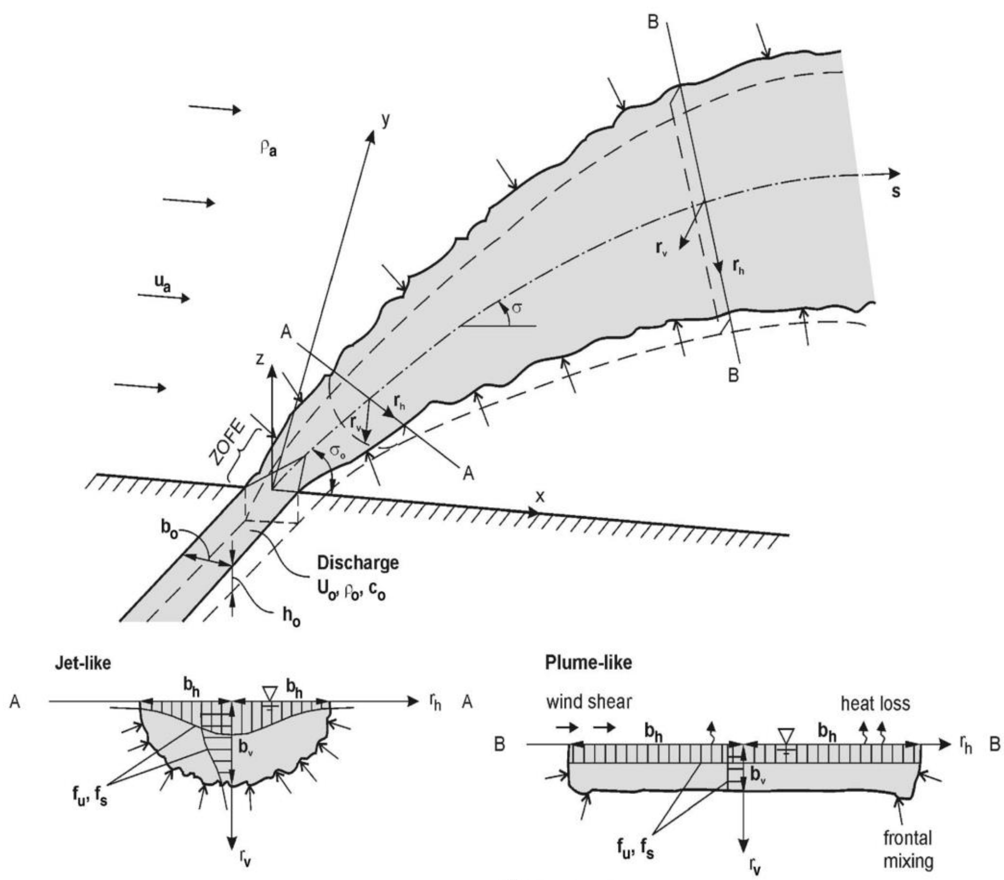

Figure 2.11 Schematic propagations of surface jets in deep water condition crossflow (Jones et al., 2007)

Figure 2.12 Density Current Formation in Lake Cayuga in Ithaca, NY.

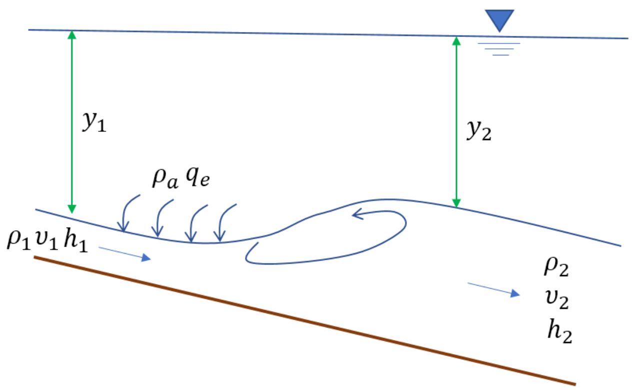

Figure 2.13 Schematic view of a Submerged Hydraulic Jump

Zone of Flow Establishment (ZOFE in Figure 2.11) is dependent on the L_Q (discharge length scale), which is related to the discharge channel geometry.

In some classifications of surface jets, wall (shoreline) attachment happens. The two most common types of attachment are Coanda attachment and wake attachment (Jones et al., 1996). Coanda attachment happens when a jet starts moving parallel to a surface because of the entrainment demand of the jet itself, and after traveling a distance, it starts to expand. These cases are more common, especially in the wall jet classification ($\sigma < 20°$). In wake attachments, the jet starts to bend rapidly due to a strong crossflow and attaches to the inner wall, and this interaction leads to a recirculation zone downstream of the jet.

One of the first numerical methods used to simulate the outfalls was integral models; for example, CORMIX3 developed by Jones et al. (1996) or PDS developed by Shirazi and Davis (1974). One of the most comprehensive models in terms of formulations was introduced by Adams et al. (1975). This model was able to consider bottom and shoreline attachments.

The latest jet integral formulations were introduced by Jirka (2007) for surface discharges into crossflow via the CorSurf predicting module of CORMIX3. In addition to all the complicated hydrodynamic processes mentioned in this part, this module is able to consider the surface heat loss of the jet and its effect on the changes in buoyancy forces. It also considers the wind effects on the surface jet and the wind-induced mixing. In this model, turbulent entrainment into the buoyant surface jet is calculated based on:

$$E = E_h + E_v + E_p + E_f + E_i \tag{2.12}$$

where E is total turbulent entrainments, E_h is the horizontal entrainment rate, E_v is vertical entrainment rate, E_p is advected puff entrainment rate, E_f is frontal entrainment rate and E_i is interfacial entrainment rate. For more information regarding the details of CorSurf formulations, please see (Jirka, 2007).

2.7.2 CFD Models

Kheirkhah et al. (2014) used a buoyancy modified solver to simulate negatively buoyant jets in the OpenFOAM software and found the best performing Reynolds Stress Turbulence Models (RSTM). Moreover, they created a modified version of the PisoFoam solver that includes the density equation as a function of salinity and temperature. Zhang et al. (2016) performed a numerical simulation of a negatively buoyant jet in OpenFOAM using the twoLiquidMixingFoam solver with both the Smagorinsky and Dynamic Smagorinsky sub-grid scale (SGS) models. They also conducted experiments to validate their numerical study.

The numerical study of surface discharges has not been investigated extensively, and it is necessary to assess the numerical model’s capabilities and different modelling approaches. In recent years, Khosravi and Javan (2020, 2022) numerically investigated the lateral thermal plume flow structures by modelling the experimental research conducted by Abdelwahed (1981). They used the *buoyantBoussinesqPimpleFoam* solver with realizable $k - \epsilon$ turbulence model in OpenFOAM. They also showed the effectiveness of using dynamic adaptive mesh refinement in OpenFOAM on the computational time and modelling results. They compared the numerical results with the experimental works conducted by Abdelwahed (1981) and concluded that the modelling approach is capable of predicting the experimental measured results of recirculation zone size, time-averaged excess temperature, half-width and half-thickness of the maximum time-averaged excess temperature, and jet trajectory along the mixing zone. Their modelling results were in good agreement with reported experimental data. Numerical simulations help extract the results for the entire field and evaluate the phenomenon accurately. Validations are necessary to ensure the results are valid and compatible with experimental studies.

A more in depth review of CFD modelling for jets in crossflow is provided in the introduction section of Chapter 5.

3 Methodology

3.1 Experimental Program

Experimental studies of surface jets in crossflows and stagnant water bodies have been conducted in this research. All experiments were conducted in the Hydraulics Laboratory of the Civil Engineering Department at the University of Ottawa. Planar and stereo particle image velocimetry techniques were used to measure the two-dimensional (planar) velocity distributions with two and three components, respectively.

3.1.1 Experimental Setup

The main components of the experimental setup are shown in Figure 3.1. Details of the experimental setup and equipment were: A) laser box for PIV, B) laser delivery arm, C) laser lenses, D) sCMOS cameras, E) moving cart, F) ultrasonic flow meter, G) rails and supports, H) electric motor, I) nozzle, J) discharging arm and K) pump and discharging fluid reservoir.

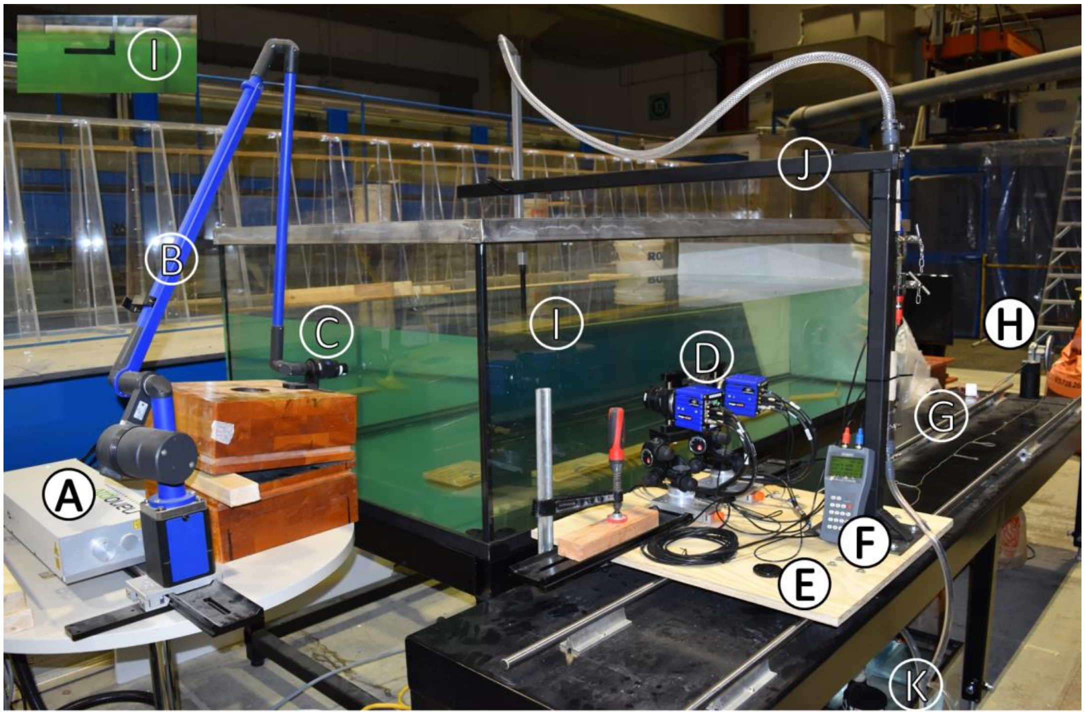

Figure 3.1 Experimental setup with the components

The nozzle was a squared cross-section pipe with an inside width of *W*=8 *mm*. The length of the nozzle before the outlet was 8.5 *cm*. It was long enough to ensure that a well-controlled flow was exiting the nozzle. An ultrasonic flow meter was installed on a stainless-steel pipe with a diameter of 19 *mm* to measure the flow rate of the system. The validity of the flow rates measured by ultrasonic flow meter examined separately by measuring the certain volume of fluid over time. The discharge rate shown on the ultrasonic flow meter was used for the experimental discharges to ensure that the discharge values were accurate at the time of the experiments.

The main reservoir had two separate zones (Figure 3.2). Zone 1 was connected to the nozzle through the discharge hose and always had a constant water level at the top. This was to ensure that the discharge rate remained constant during the experiment. A pump was used to maintain a constant water level in Zone 1 by providing a constant flow through the insulated thermal path from Zone 2 shown by the red arrow in Figure 3.2. The excess water from Zone 1 overflowed back to Zone 2.

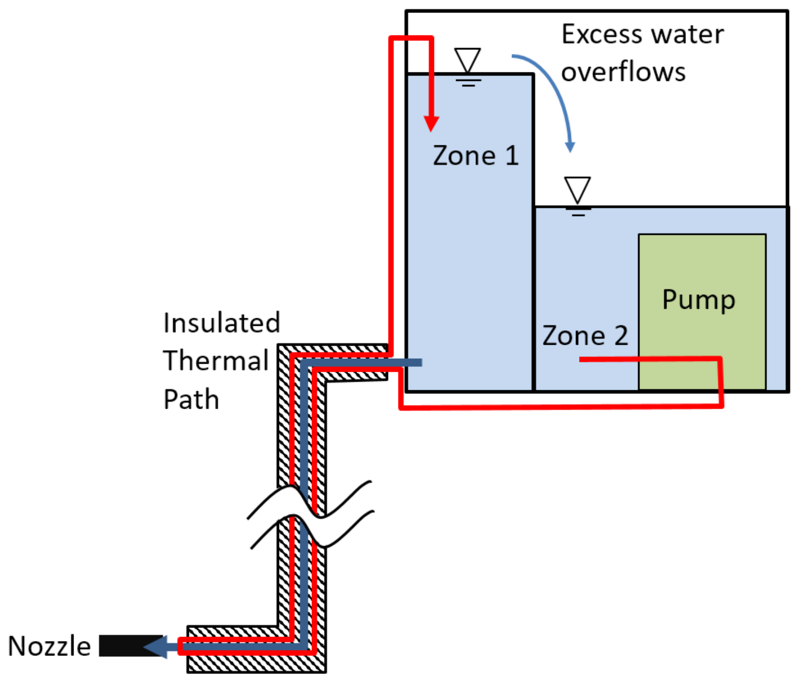

Figure 3.2 The main reservoir included two separate zones and a pump

The insulated thermal path included three main items shown in Figure 3.3. First, a flexible hose was connected to the pump to convey a constant flow of warm water from Zone 2 to Zone 1. Hose

A in Figure 3.3 shows the flow of water from Zone 2 towards the nozzle. Hose B in Figure 3.3 shows the flow of water in the flexible hose back to Zone 1. Second, discharge hose that was surrounded by the flexible hose. Third, insulation that surrounded the discharge hose and flexible hose prevented any environmental heat loss.

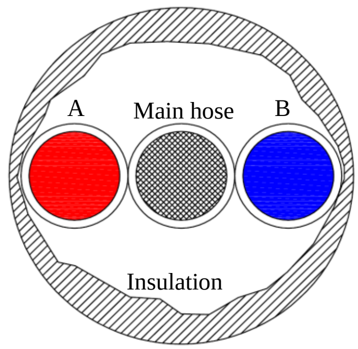

Figure 3.3 Insulated thermal path around main discharge hose

Water with the required temperature flowed in the insulated thermal path to make sure temperature losses in the system were minimal. Water temperatures in the flume, discharge reservoir and outlet of the nozzle were monitored using digital thermometers. The main flume was 2.4 *m* long, 1.2 *m* wide and 0.7 *m* high. The water was stationary inside the flume but the nozzle was movable with adjustable speed.

Experiments mainly included two different cases, stagnant and crossflow. In the case of discharging the jet into crossflow, the nozzle moved with a constant speed. The discharge unit was installed on a rail cart system connected to an electric motor with adjustable speed. Current in the crossflow case was simulated by moving the jet instead of having the flow in the main flume. This is a common approach in the literature (e.g., Abessi and Roberts (2016) for LIF experiments). Cameras were installed on the cart and moved with the same speed as the nozzle. It was challenging to move the cameras only in the X direction without any oscillations or misalignments. As the cameras were almost 0.7 m away from the plane of measurement in the flume, a small amount of rotation in the camera would lead to a large amount of displacement in the depth of focus (Figure 3.4).

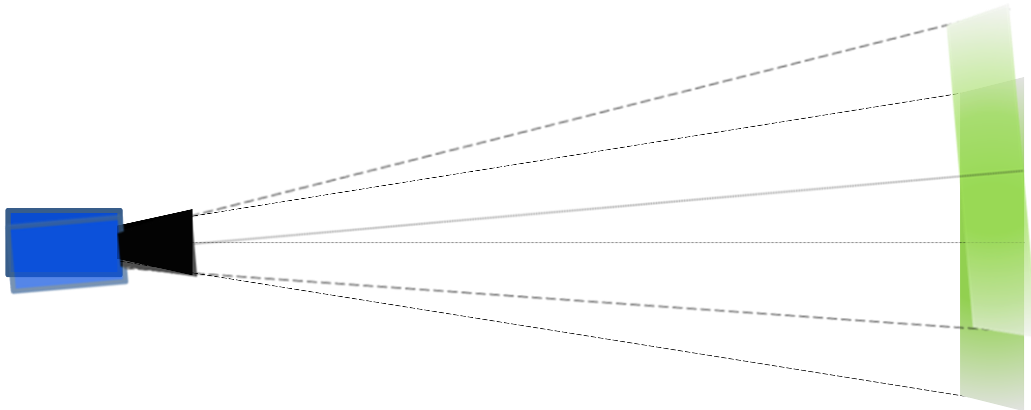

Figure 3.4 Small misalignment of the camera will lead to large errors in the measurement zone

Laser was used as the light source in the PIV system. The laser illuminated a vertical sheet along the length of the flume and various measurements were conducted to ensure that the laser was fully vertical and parallel to the flume walls. The image quality of the camera was controlled in multiple locations along the length of the flume to ensure that the camera was moving parallel to the vertical laser sheet and particles were set in the camera's depth of focus.

Stereo-PIV measurement needs two cameras (Figure 3.5) to evaluate the third velocity component perpendicular to the plane of measurement. Stereo-PIV imaging created perspective distortion because of the angle of view. Perspective error caused image distortion in a way that the closer edge of the calibration target looked larger compared to the farther edge. In this study, data close to the surface were important, so both cameras were rotated to have the edge of the images parallel to the water surface. Figure 3.6 shows the mapped images together, indicating that the red dot is at the same location in the mapped image.

Three-dimensional calibration with dots at the front and rear planes was used to calibrate the recorded images. These dots were also used to scale the images based on the real dimensions of the target. Scaling maps the pixel size of the recorded images to the actual length on the calibration target. For example, one millimeter in the laser plane represents a certain number of pixels in the image. A 3rd order polynomial was used for mapping of the recorded images. At the end of the calibration process, the results appeared as in Figure 3.7.

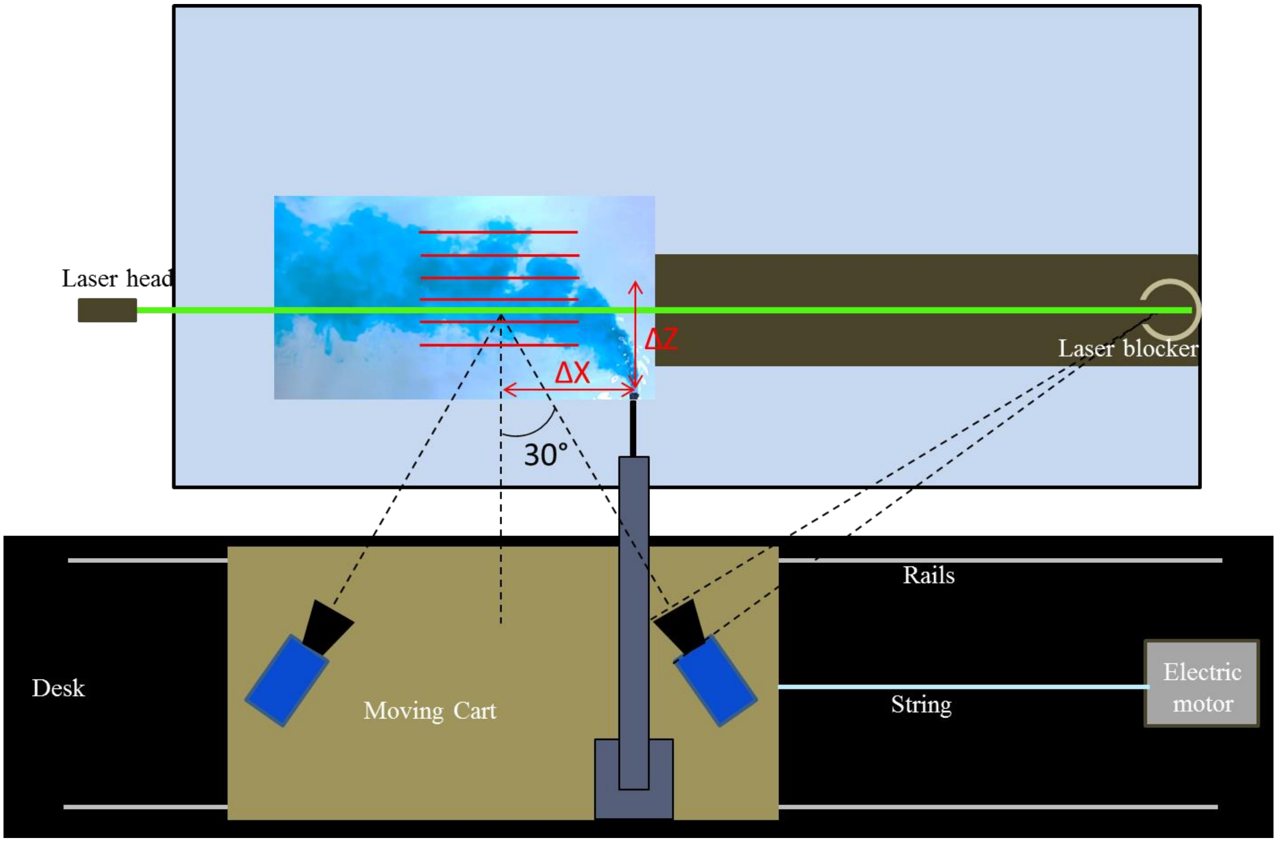

Figure 3.5 Schematic drawing of the experimental setup (plan view)

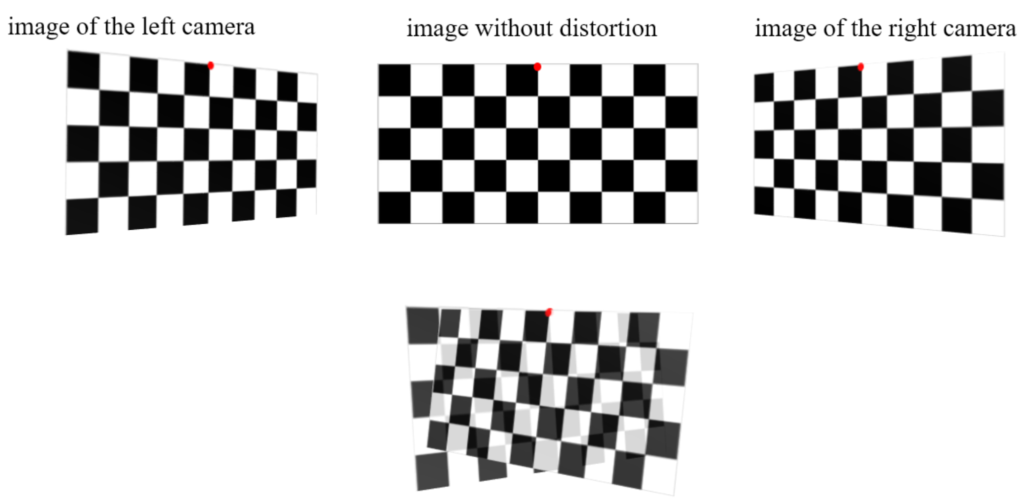

Figure 3.6 Perspective distortion of the two cameras and calibration target edge parallel with surface

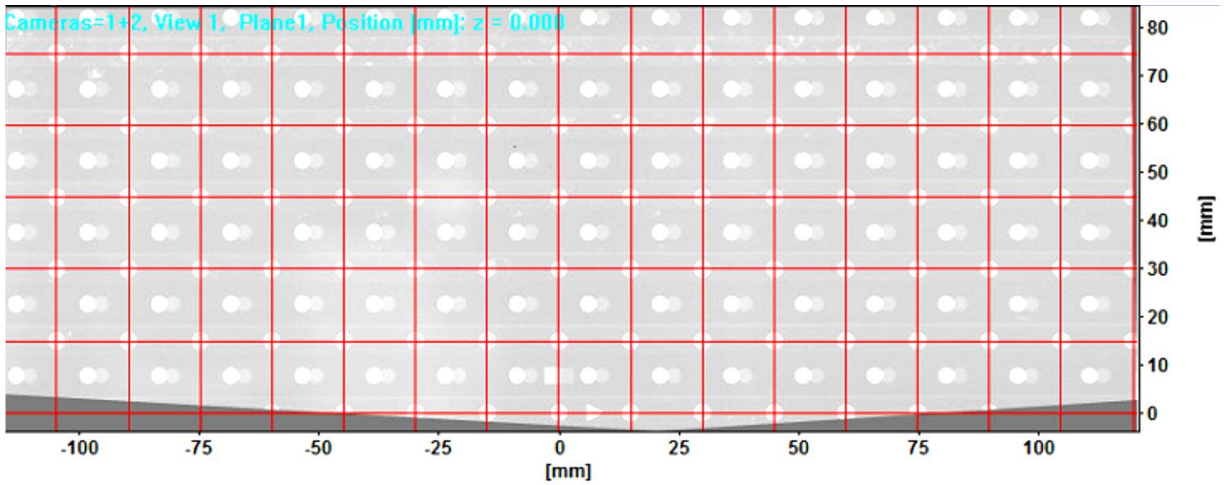

Figure 3.7 Calibrated image on front plane of the target

One of the challenges of the crossflow experiment was that the laser intensity dropped along the flume as it propagated to the end of the flume. As a result, there was a limitation with respect to aperture size in the cameras on both ends of the flume. When the cart is closer to the laser, the aperture should be narrow enough to prevent saturation of the particles. However, the camera aperture size farther from the laser should be wide enough to measure images with reasonable quality. Saturation of particles happens in a case that light intensity is more than the camera sensor sensitivity. In this case, it is not possible to take acceptable images of the saturated particles and it will cause errors in the measurements. The sCMOS cameras used in the experiments had a sensitivity count of 64,000.

In Stereo-PIV measurements, the left camera was facing toward the end of the flume where the laser plane hit the barrier and created some reflections back to the camera. In order to solve this problem, a 3" pipe was used to block the reflections (Figure 3.8). This pipe had an opening alongside for the emitted laser sheet. Similarly, there was a black non-reflective material at the bottom of the flume to prevent the laser reflections from the bottom glass.

In order to prevent the reflections from the surface of the water, the laser lens was rotated to have the laser sheet expansion line parallel to the water surface. At the time of the experiments the flume appeared as in Figure 3.9.

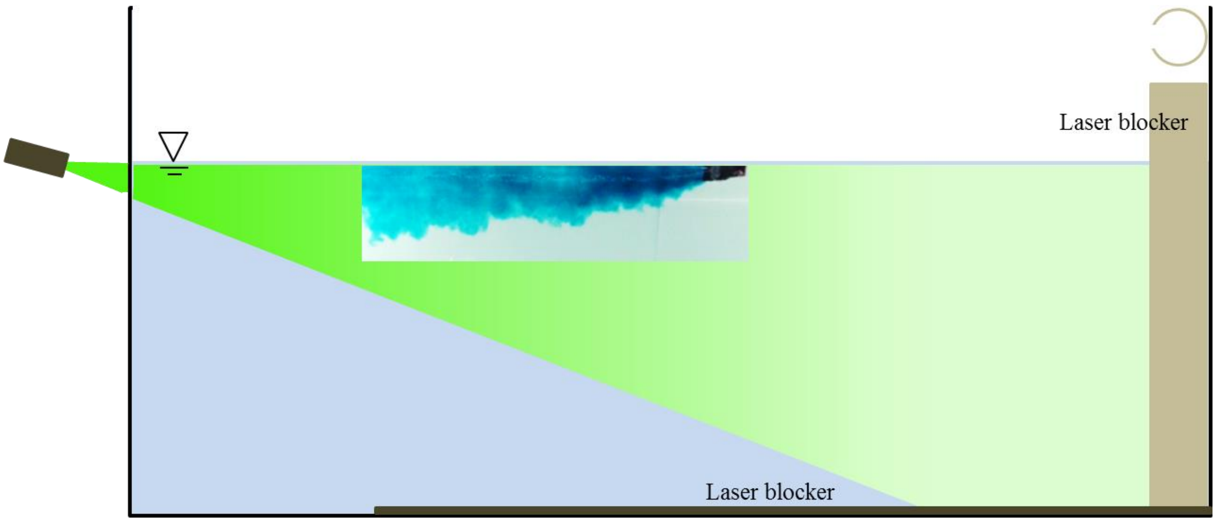

Figure 3.8 Laser intensity gradient along the flume

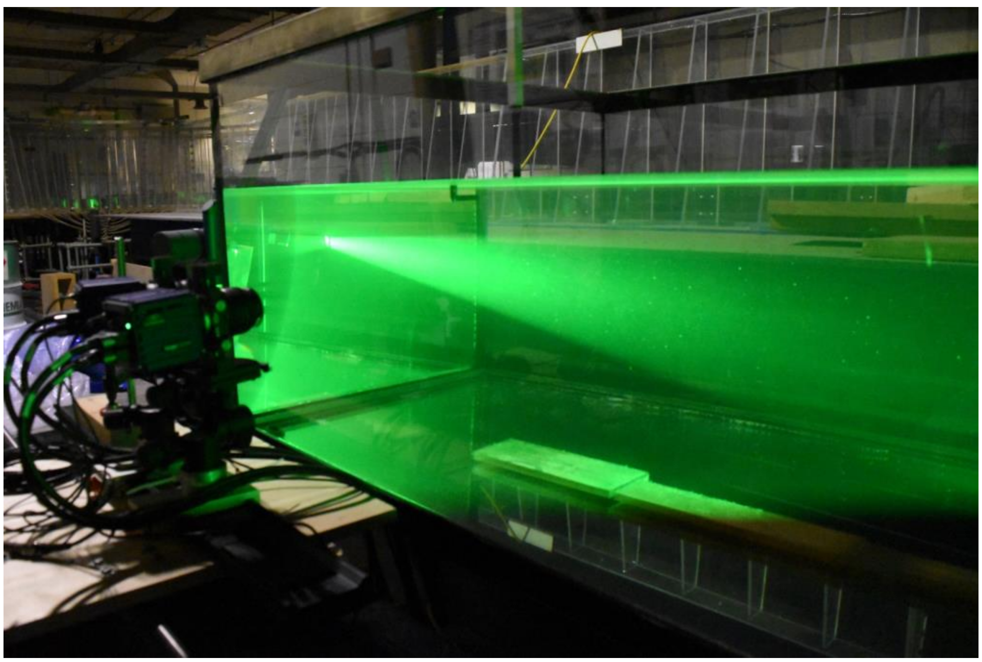

Figure 3.9 Experimental system operating in the lab

The reason that laser emission was not from the top or bottom of the flume was the oscillations of the water surface in the cases related to surface jets. Water surface oscillations cause reflections and misalignment in the laser plane. As an example, Figure 3.10 shows how local changes in water surface elevation alters the direction of light passing through the surface. It shows that two vortices are propagating in a pool and their shadows are created at the bottom of the pool. A shadow is generated as a result of the bending of sunlight rays. This happens because of the local changes in the water surface inclination and different refractive indices of air and water.

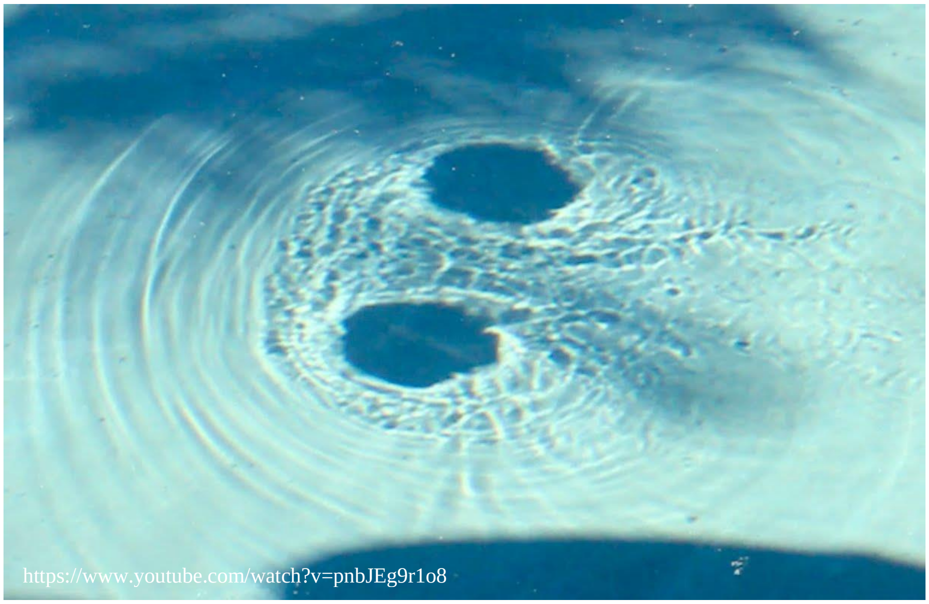

Figure 3.10 Shadow of two vortices at the bottom of the pool because of inclination of water surface

3.1.2 PIV Measurements

Experimental works in the current research include buoyant and non-buoyant cases. Squared pipe was used as a discharge nozzle to simulate the geometry of hydraulic channels in the experiments as follows:

- Buoyant discharges into crossflow;
- Non-buoyant surface discharges into stagnant water.

Planes of interest are shown in Figure 3.11 for both cases. For discharge into crossflow (Figure 3.11(a)), planes of interest are perpendicular to the nozzle or parallel with the crossflow. Different planes were measured to ensure that the width of the jet was captured in the mixing zone. For discharge into stagnant water (Figure 3.11(b)), two different groups of planes were chosen to be parallel and perpendicular to the jet axis to extract velocity distributions.

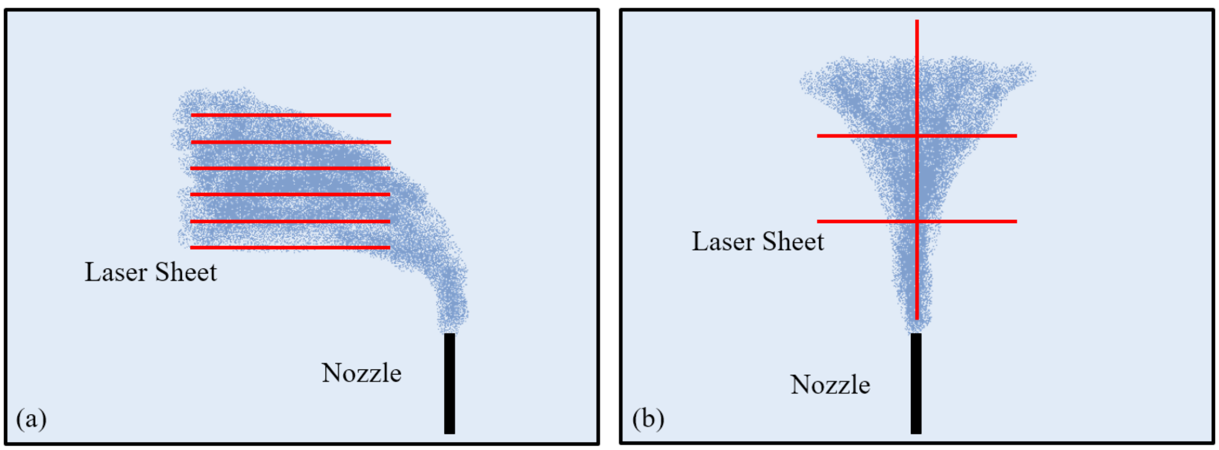

Figure 3.11 Plan view of planes of interest for PIV measurements (a) crossflow (b) stagnant water

3.1.3 Errors and Limitations

In the experimental part of the present research, two major types of errors were likely to happen. The first type of error was called precision error or repeatability error, and was caused by using analog instruments (e.g., using a caliper, measuring tape or L square ruler). The second type of error was bias error or systematic error; the source of this error was calibration of the measuring instruments. Bias error could be constant, a scale error or a combination of both. A hidden type of bias error, which was likely to happen, was conceptual error. This is related to the condition that the researcher is not aware of the existence of the error and that the data being measured is not the reality.

In this research, errors might affect the following parameters:

- Crossflow velocity: non-uniform cart movement was the major source for this parameter. The strategy to deal with this error was to eliminate the noisy data of the velocity measurements at the beginning or end of each experiment. Measurements were conducted only in the middle part of the cart's movement.
- Discharge rate: the discharge rate of the jet was measured by calculating the time of filling the known volume by a chronometer in addition to the use of an ultrasonic flow meter. In order to deal with this error, the size of the tank was relatively large ($10l$) and the water level was at a constant elevation.
- Temperature measurements: digital thermometers were used with the precision of $0.1°C$. The nozzle sensor was right before the nozzle exit and the discharging path was insulated to minimize the temperature variations in the buoyant cases.
- PIV errors: these errors are explained in Section 3.1.1

This experimental work has some limitations that can be summarized as follows:

- The flume dimensions were limited for the experiments, which dictated a smaller nozzle size in order to make sure that the wall effect (the width of flume is $1.1m$) would not impact the measurements.
- Crossflow velocity was limited due to the length of the flume.
- The maximum temperature in the warm water was limited due to image quality required for PIV. When temperature difference was more than $30°C$, the PIV images were blurry and were not useful for PIV algorithm.
- Surface heat exchange was not considered to be an effective parameter in this study. The reason was that it took less than three seconds for the surface jet to advect to the plane of measurement due to the crossflow current. Therefore, this scaled down experiment might not be a suitable representation of the real phenomenon in terms of surface heat exchange, but it is a suitable representation of the mixing phenomenon.

3.1.4 Experimental Procedure

Current velocity was generated by the movement of the cart containing the camera and nozzle. The current velocity was exactly the same as crossflow velocity. PIV experiments were performed to assess the velocity of the cart, which was almost constant in the entire field of view (average $U_x = 0.11\ m/s$ in Figure 3.12a). The value of the standard deviation is also shown for the current velocity in Figure 3.12b.

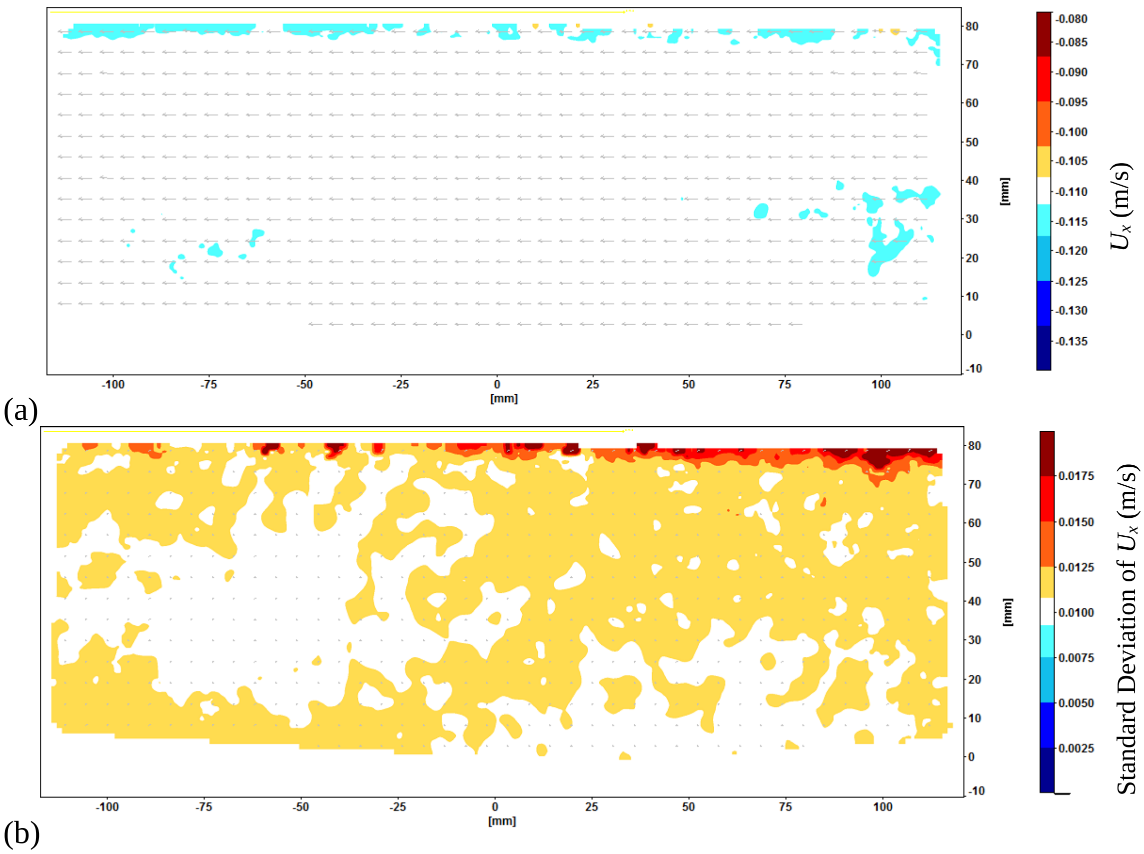

Figure 3.12 Current (cart) velocity in X direction (a) average velocity in X direction U_x (b) standard deviation of velocity U_x in X direction

Figure 3.13 shows that the surface jet had a higher density of seeding particles in order to have enough particles for the stereo cross-correlation algorithm (image number 124 for crossflow non-buoyant case). Image dimensions were 2560×1026 pixels and they represented the area of $0.220 \times 0.85\ m$ on the plane of interest. In other words, $1mm$ was almost 11 pixels in the images.

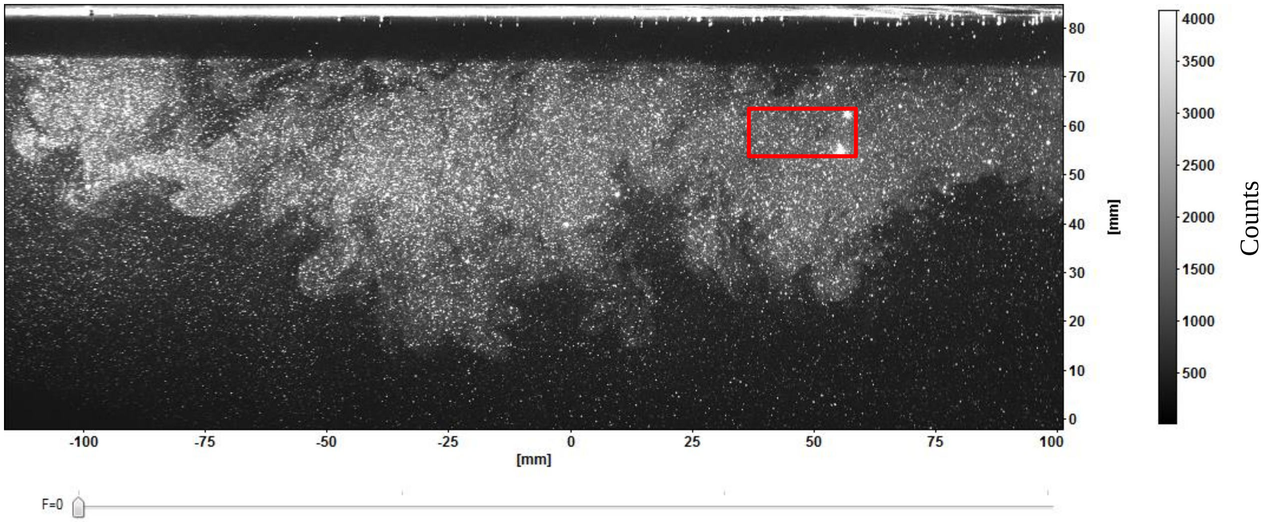

Figure 3.13 Seeding particle density difference between the surface jet and crossflow

The first step before using the image processing algorithm for velocity calculations was image preprocessing. Average of particle brightness count was calculated for all of the captured images for each pixel. By deducting this calculated average value from the original images, a new series of images were created and used for image processing. This led to a higher contrast in the images as shown in Figure 3.14(b).

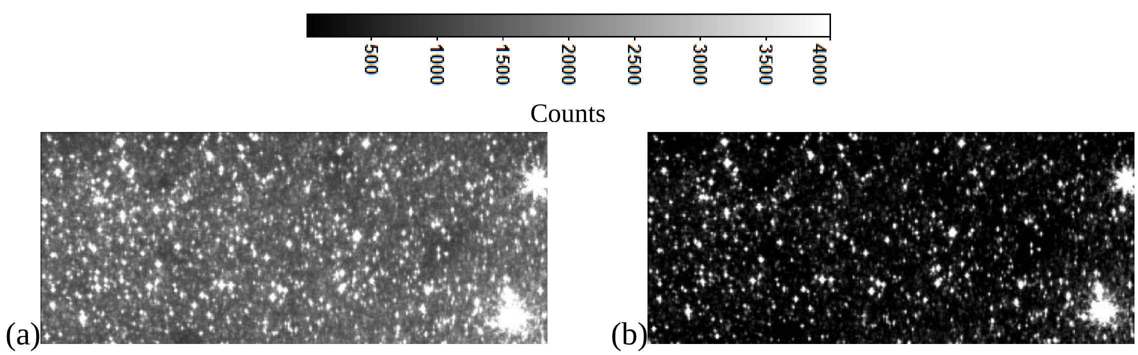

Figure 3.14 Seeding particle density inside of the discharge jet (red rectangle in Figure 3.13): (a) original image (b) new image after removing the average light intensity

3.2 Numerical Simulations

3.2.1 Introduction

In order to predict the velocity and concentration distributions of new outfalls or conduct an investigation of the mixing in the existing outfalls, numerical simulation is necessary. Even in the experimental studies, it is costly to measure the data at every location within the region of interest. One of the first numerical methods to simulate the outfalls was via the integral models introduced in Chapter 2. By improving the computational capacity, it is possible to simulate three-dimensional surface jets in crossflow. Numerical simulations help extract the results for the entire field and evaluate the phenomenon accurately. The validation of numerical results is necessary to understand the reliability of the numerical models in predicting the mixing characteristics in the region of interest.

In this research, numerical studies are mainly divided into two major categories. The first category is related to the similar experimental studies in the literature. The second category is related to experiments conducted in the current study and presented in Chapter 4 and Appendix A. This chapter introduces the numerical models and methodology used in this research.

3.2.2 Theoretical Background

Most of the flows in nature and in outfalls are turbulent. Turbulent flows have oscillatory characteristics. This means that each variable of the flow varies by time and location. In order to evaluate these kinds of flows accurately, it is necessary to study different kinds of turbulence models. Equations and turbulence models used in this study are introduced in this part. As the focus of this research is on mixing of jets, which mainly represent outfalls, equations are considered for Newtonian incompressible flow.

3.2.3 Turbulence Modelling

Navier-Stokes equations for Newtonian incompressible flow describe the governing equations for fluid motion mainly based on Newton's second law. Momentum conservation equations in Einsteinian notation are described as:

$$\rho \frac{\partial u_i}{\partial t} + \rho \frac{\partial (u_j u_i)}{\partial x_j} = \frac{\partial \tau_{ij}}{\partial x_j} - \frac{\partial p}{\partial x_i} + \rho g_i \quad (3.1)$$

where u_i is velocity, p is the pressure, ρ is the fluid density, t is time, g is gravitational acceleration and x_i is the coordinates in the Cartesian frame.

The viscous stress is considered as:

$$\tau_{ij} = \mu_t \left(\frac{\partial u_i}{\partial x_j} + \frac{\partial u_j}{\partial x_i} \right) \quad (3.2)$$

where μ_t is the turbulent molecular viscosity.

The continuity equation based on the conservation of mass leads to:

$$\frac{\partial u_i}{\partial x_i} = 0 \quad (3.3)$$

The advection-diffusion equation for scalar parameters is considered as:

$$\frac{\partial (\varphi)}{\partial t} + \frac{\partial (u_i \varphi)}{\partial x_i} = D \frac{\partial^2 \varphi}{\partial x_i^2} \quad (3.4)$$

where φ is the scalar concentration and D is the isotropic diffusion coefficient. There are three major approaches used in order to solve these equations: Direct Numerical Simulation (DNS), Large Eddy Simulation (LES) and Reynolds-Averaged Navier-Stokes (RANS). DNS is used to solve the equations directly without using any turbulence models, and consequently, it needs very fine mesh and very small time steps. In this research, LES and RANS methods were used to solve the governing equations, which are described below.

Reynolds Averaged Navier-Stokes Equations

In order to simplify the solution of governing equations, in RANS method, it is assumed that every variable consists of the summation of an average part and an oscillatory part. Therefore, the velocity can be written as:

$$u(x,t) = \bar{u}(x) + u^{'}(x,t) \text{ or } u = U + u^{'} \quad (3.5)$$

where the average can be defined as:

$$\bar{u}(x) = \lim_{T \to \infty} \frac{1}{T} \int u(x,t)\, dt \text{ or } \bar{\varphi}(x) = \lim_{T \to \infty} \frac{1}{T} \int \varphi(x,t)\, dt \quad (3.6)$$

After averaging, Navier-Stokes equations can be written as:

$$\rho \frac{\partial \bar{u}_i}{\partial t} + \rho \bar{u}_j \frac{\partial \bar{u}_i}{\partial x_j} = -\frac{\partial p}{\partial x_i} + \frac{\partial}{\partial x_j}\left[\mu \left(\frac{\partial \bar{u}_i}{\partial x_j} + \frac{\partial \bar{u}_j}{\partial x_i}\right) - \rho \overline{u_i^{'} u_j^{'}}\right] + \rho g_i \quad (3.7)$$

$$\frac{\partial \bar{u}_i}{\partial x_i} = 0 \quad (3.8)$$

$$\tau_{ij}^R = -\overline{u_i^{'} u_j^{'}} \quad (3.9)$$

The term τ_{ij}^R is called Reynolds stress and it is considered to be similar to viscous stress (τ_{ij}). The tensor index notation ($\overline{u_i^{'} u_j^{'}}$) includes six unknowns. In order to estimate these terms, different approaches were used and turbulence models were developed. In this study one turbulence model was used from each category (two equation eddy viscosity, Reynolds Stress Transport Models and Large Eddy Simulation) to assess the efficiency of different turbulence models with respect to surface jets. These models were chosen based on similar studies (Kheirkhah et al., 2014) related to mixing.

k* − *ϵ* *Model

The $k - \epsilon$ model is one of the most popular two-equation eddy viscosity turbulence models. This model is based on two equations for k and ϵ. Here, a brief description of this model is presented. ϵ is called the dissipation rate and k is the turbulent kinetic energy, which is considered as:

$$k = \frac{1}{2}\overline{u_i^{'} u_i^{'}} = -\frac{1}{2}\tau_{ii}^R \quad (3.10)$$

Two main approximations are required to create the main equation for k as:

$$\frac{\partial k}{\partial t} + \bar{u}_j \frac{\partial k}{\partial x_j} = \tau_{ij}^R \frac{\partial \bar{u}_i}{\partial x_j} - \varepsilon + \frac{\partial}{\partial x_j}\left[\left(\nu + \frac{\nu_t}{\sigma_k}\right)\frac{\partial k}{\partial x_j}\right] \quad (3.11)$$

where ν is kinematic viscosity, υ_t is the turbulent eddy viscosity and σ_k is a closure coefficient. One of the main approximations is the Boussinesq approximation related to Reynolds stress tensor:

$$\tau_{ij}^R = 2\nu_t S_{ij} - \frac{2}{3}k\delta_{ij}, \quad S_{ij} = \frac{1}{2}\left(\frac{\partial u_i}{\partial x_j} + \frac{\partial u_j}{\partial x_i}\right) \quad (3.12)$$

where δ_{ij} is the Kronecker delta and S_{ij} is the strain tensor. Turbulent eddy viscosity is calculated as:

$$\upsilon_t = C_\mu \frac{k^2}{\epsilon} \tag{3.13}$$

where C_μ is a constant in the closure.

Considering all of the 6 equations until this point (1 continuity, 3 momentums, 1 concentration and k equation), there are 7 unknown variables (3 velocity components, 1 pressure, 1 concentration, k and ϵ)

One more equation is needed to obtain a closed system of equations. So ϵ equation is introduced as:

$$\frac{\partial \epsilon}{\partial t} + \overline{u}_j \frac{\partial \epsilon}{\partial x_j} = C_{\epsilon 1} \frac{\epsilon}{k} \tau_{ij} \frac{\partial \overline{u}_j}{\partial x_j} - C_{\epsilon 2} \frac{\epsilon^2}{k} + \frac{\partial}{\partial x_j}\left[\left(\nu + \frac{\nu_t}{\sigma_\epsilon}\right)\frac{\partial \epsilon}{\partial x_j}\right] \tag{3.14}$$

Table 3.1 Coefficients of $k - \epsilon$ model

$C_{\epsilon 1}$	$C_{\epsilon 2}$	C_μ	σ_k	σ_ϵ
1.44	1.92	0.09	1	1.3

Launder, Reece and Rodi Model

The Launder-Reece-Rodi (LRR) model is one of the Reynolds Stress Transport Models (RSTM). In this method, there is a main transport equation for Reynolds stress derived from subtracting the averaged momentum equation from the instantaneous one as:

$$\frac{D\overline{u_i u_j}}{Dt} = \frac{\partial \overline{u_i' u_j'}}{\partial t} + \overline{u}_k \frac{\partial \overline{u_i' u_j'}}{\partial x_k} = D_{ij}^{\nu} + D_{ij}^{T} + \phi_{ij} + P_{ij} + \epsilon_{ij} \tag{3.15}$$

where P_{ij} is the production term, D_{ij} is the diffusion term, ϕ_{ij} is the pressure strain rate correlation term, and ϵ_{ij} is the turbulent dissipation rate term.

The production or generation rate of Reynolds stress by mean velocity is calculated directly as:

$$P_{ij} = -\overline{u_i' u_k'} \frac{\partial \overline{u}_j}{\partial x_k} - \overline{u_j' u_k'} \frac{\partial \overline{u}_i}{\partial x_k} \tag{3.16}$$

Diffusion terms are mainly divided by two parts; viscous diffusion D_{ij}^{ν} and turbulent diffusion D_{ij}^{T}. Viscous diffusion is closed and is calculated directly as:

$$D_{ij}^{\nu} = \nu \frac{\partial^2 \overline{u_i' u_j'}}{\partial x_k \partial x_k} \tag{3.17}$$

where ν is kinematic viscosity. Turbulent viscous diffusion includes the pressure diffusion and turbulent convection. It requires modelling, and the most popular way of representing it is using the Generalized Gradient Diffusion Hypothesis, GGDH, which can be written as:

$$D_{ij}^{T} = -\frac{\partial}{\partial x_k}\left(\overline{u_i' u_j' u_k'} + \frac{\overline{p'}}{\rho} u_j' \, \delta_{ik} + \frac{\overline{p'}}{\rho} u_i' \, \delta_{jk}\right) = \frac{\partial}{\partial x_l}\left(C_s \frac{\epsilon}{k} \, \overline{u_l u_k} \, \frac{\partial \overline{u_i u_j}}{\partial x_k}\right) \tag{3.18}$$

where $C_s = 0.22$.

The dissipation term is modelled as:

$$\epsilon_{ij} = -2\nu \overline{\frac{\partial u_i'}{\partial x_k}\frac{\partial u_j'}{\partial x_k}} \tag{3.19}$$

$$\frac{\partial \epsilon}{\partial t} + \overline{u}_k \frac{\partial \epsilon}{\partial x_k} = C_{\epsilon 1} \frac{P_k \epsilon}{k} - C_{\epsilon 2} \frac{\epsilon^2}{k} + \frac{\partial}{\partial x_j}\left(C_\epsilon \frac{k}{\epsilon} \overline{u_i' u_j'} \frac{\partial \epsilon}{\partial x_j}\right) \tag{3.20}$$

where P_k is defined as:

$$P_k = -\overline{u_i' u_j'} \frac{\partial \overline{u}_i}{\partial x_j} \tag{3.21}$$

and $C_{\epsilon 1}$ and $C_{\epsilon 2}$ are the coefficients shown in Table 3.2.

Table 3.2 Coefficients of the LRR model

C_1	C_2	C_3	C_4	$C_{\epsilon 1}$	$C_{\epsilon 2}$
3.0	0.8	1.75	1.31	1.44	1.90

Pressure-strain correlation is the most important part of this model because it has the same order as the production term. In the LRR model the unknowns are modelled by:

$$\phi_{ij} = -\frac{1}{\rho}\,\overline{p'\frac{\partial u_i'}{\partial x_j}} - \frac{1}{\rho}\,\overline{p'\frac{\partial u_j'}{\partial x_i}} \tag{3.22}$$

$$\begin{aligned}\phi_{ij} = -C_1\,\epsilon\, b_{ij} + C_2\, k\, S_{ij} + C_3\, k\left(b_{ik}S_{jk} + b_{jk}S_{ik} - \frac{2}{3}b_{mn}S_{mn}\delta_{ij}\right) \\ + C_4\, k\big(b_{ik}\Omega_{jk} + b_{jk}\Omega_{ik}\big)\end{aligned} \tag{3.23}$$

where b_{ij} is the normalized anisotropy tensor and Ω_{ik} is the rotation rate tensor as:

$$b_{ij} = \frac{a_{ij}}{2k} = \frac{\overline{u_i'u_j'}}{2k} - \frac{1}{3}\delta_{ij} \tag{3.24}$$

$$S_{ij} = \frac{1}{2}\left(\frac{\partial \overline{u}_i}{\partial x_j} + \frac{\partial \overline{u}_j}{\partial x_i}\right) \tag{3.25}$$

$$\Omega_{ij} = \frac{1}{2}\left(\frac{\partial \overline{u}_i}{\partial x_j} - \frac{\partial \overline{u}_j}{\partial x_i}\right) \tag{3.26}$$

The constant values of C_1 to C_4 are presented in Table 3.2.

Large Eddy Simulation Model

The Large Eddy Simulation (LES) turbulence model has the advantage of simulating the large sized eddies compared to RANS models. Eddies play an important role in the mixing of two fluids because they contain most of the energy. The LES model is able to consider eddies in the flow more accurately than the other methods described earlier. The downside of this model is the need for a finer mesh, and consequently, higher computational cost. The main difference between RANS and LES modelling approaches is that in LES spatial filter is applied on the equations, however, time averaging filter is applied in RANS modelling approach.

Filtering is the first step in this model. It decomposes velocities into resolved (filtered) and residual (sub-grid) parts and removes the scales smaller than the grid size. The filter width is related to the cell volume and is a limit in simulating the smallest eddy.

$$u(x,t) = \widetilde{U}(x,t) + u'(x,t) = \widetilde{u_i} + u_i' \tag{3.27}$$

The spatial filtered value of $\widetilde{u_i}$ is defined as integral over the volume:

$$\widetilde{u_i}(x,t) = \iiint G(x-\xi;\Delta)u_i(\xi,t)d^3\xi \tag{3.28}$$

where G is the spatial filter used as:

$$G(x-\xi;\Delta)=\begin{cases}1/\Delta^3, |x_i-\xi_i|<\Delta x_i/2\\ 0 \qquad otherwise\end{cases} \tag{3.29}$$

and $\Delta=(\Delta x\ \Delta \mathrm{y}\ \Delta z)^{1/3}$ is the filter size.

Filtered Navier-Stokes equations for LES methods after applying the spatial filter are written as:

$$\frac{\partial \widetilde{u_i}}{\partial x_i}=0 \tag{3.30}$$

$$\rho\frac{\partial \widetilde{u_i}}{\partial t}+\rho\frac{\partial\left(\widetilde{u_i u_j}\right)}{\partial x_j}=-\frac{\partial p}{\partial x_i}+\frac{\partial}{\partial x_j}\left[\mu\left(\frac{\partial \widetilde{u_i}}{\partial x_j}+\frac{\partial \widetilde{u_j}}{\partial x_i}\right)\right] \tag{3.31}$$

The interactions between large scale filtered eddies $\widetilde{u_i}$ and the Sub-Grid-Scale (SGS) modelled eddies u' lead to the nonlinear term of $\widetilde{u_i u_j}$ written as:

$$\widetilde{u_i u_j}=\widetilde{u_i}\widetilde{u_j}+\widetilde{u_i u_j'}+\widetilde{u_i' u_j}+\widetilde{u_i' u_j'}=\widetilde{u_i}\widetilde{u_j}-\tau_{ij}^{SGS} \tag{3.32}$$

This will change equation (3.31) as:

$$\rho\frac{\partial \widetilde{u_i}}{\partial t}+\rho\widetilde{u_j}\frac{\partial \widetilde{u_i}}{\partial x_j}=-\frac{\partial \tilde{p}}{\partial x_i}+\frac{\partial \widetilde{\tau_{ij}}}{\partial x_j}-\rho\frac{\partial \tau_{ij}^{SGS}}{\partial x_j} \tag{3.33}$$

It is almost similar to the RANS equation. The only difference is that the first term on the left side of the equation (3.33), which is the continuity equation, is equal to zero. Reynolds stress, τ_{ij}^{R}, in RANS equations is also replaced by SGS stress tensor τ_{ij}^{SGS}.

The Smagorinsky SGS model is one of the most popular SGS models in the literature. It considers the SGS stress tensor τ_{ij}^{SGS} and the SGS turbulent concentration flux (Q_j) for incompressible flow as:

$$\tau_{ij}^{SGS}=-2\nu_{SGS}S_{ij},\quad S_{ij}=\frac{1}{2}\left(\frac{\partial \widetilde{u_i}}{\partial x_j}+\frac{\partial \widetilde{u_j}}{\partial x_i}\right) \tag{3.34}$$

Turbulent eddy viscosity is calculated from:

$$\nu_{SGS} = (C_s \Delta)^2 \sqrt{S_{ij} S_{ij}} \tag{3.35}$$

where C_s is the Smagorinsky constant, which can be chosen between 0.1 and 0.24. Here it is set to 0.17 in the model (Zhang et al., 2016).

3.2.4 OpenFOAM

OpenFOAM (Open Field Operation and Manipulation) was used for numerical simulation in this study. OpenFOAM is an open-source software installed on the Ubuntu Linux operating system (recently the Windows version was also released). It is a free software with a wide range of turbulence models and solvers. The source code of the solvers and turbulence models are accessible for modification. OpenFOAM is written in the C++ programming language and it is object oriented (Weller et al., 1998). It is necessary to learn the functions inside the OpenFOAM environment to implement modifications of the source code. Figure 3.15 shows the typical structure of a simulated problem in OpenFOAM.

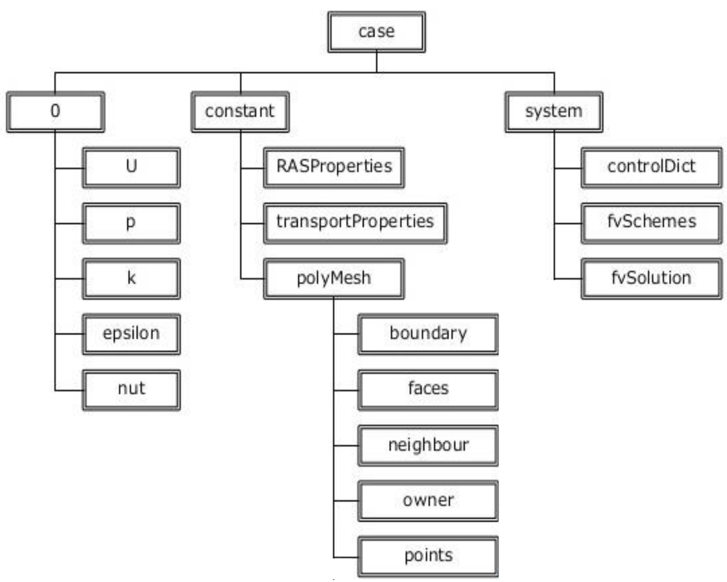

Figure 3.15 Description of the folder structure of OpenFOAM

Geometry, mesh, solvers, initial conditions and boundary conditions are the components of an OpenFOAM project.

4 Experimental Study of Surface Buoyant Jets in Crossflow[1]

Abstract

The dispersion of surface jets in crossflows such as rivers or channels can cause critical environmental problems in the form of chemical or thermal pollution of these water bodies. The turbulent flow structures occurring in such crossflows play an important role in the mixing of surface jets with the surrounding water bodies. In this study, experimental measurements of the time history of the 3-D velocity field were conducted to better understand the flow structure of surface jets in crossflow conditions. Stereoscopic Particle Image Velocimetry (Stereo-PIV) was used to measure the instantaneous spatial and temporal velocity distribution downstream of the jet's discharge point. In addition to the mean velocity distribution, turbulent flow characteristics such as the turbulent kinetic energy (k), turbulent kinetic energy dissipation rate (ϵ), and turbulent eddy viscosity (υ_t) were calculated. The formation and evolution of a vortex in the surface jet's flow structure was detected over the measurement zone. The vortex in the surface jets in crossflows resembled to half of the vortices in a counter-rotating vortex pair (CVP) of submerged jets in crossflows. It can be inferred that the water surface performed like a plane of symmetry.

Keywords Surface jets . Turbulent flow structure . Stereoscopic particle image velocimetry . Turbulent kinetic energy dissipation rate . Turbulent stress .

4.1 Introduction

In general, discharges of jets into crossflows can happen either at the surface of the receiving water body or as a submerged jet. The mechanisms of mixing of jets in crossflows have been previously

[1] This section of the study has been published as: Gharavi, A., A. Mohammadian, I. Nistor, E. Peña, and J. Anta. 2020. "Experimental study of surface buoyant jets in crossflow." *Environ. Fluid Mech.*, 20 (4): 1007–1030. https://doi.org/10.1007/s10652-020-09737-7.

investigated by researchers and are of significant importance for engineers designing discharge systems. Surface discharges are the oldest, simplest, and, typically, the most inexpensive way of discharging pollutants into rivers or coastal waters. Because of a lower level of dilution (typically 10 or less, (Jones et al., 2007)), surface discharges are more likely to have negative environmental impacts compared to the submerged ones. Heated cooling-water discharges from power plants and treated industrial or municipal wastewater discharged into rivers are some examples of surface jets in crossflows. Furthermore, the case of a river reaching the sea or becoming a tributary of another river represents a surface jet discharged into a water body (stagnant or crossflow). To better understand the turbulent flow characteristics of surface jets in crossflows, it is necessary to study their spatial and temporal evolutions.

One of the first studies on jets was conducted by Pratte and Baines (1967), who extracted jet trajectories under different jet-to-crossflow velocity ratios (R), which is defined as $R = u_0/u_a$, where u_0 is initial jet velocity and u_a is crossflow velocity. Also, earlier efforts using mathematical models to predict surface discharge behaviours were made by Dunn et al. (1975) and McGuirk and Rodi (1978, 1979). In order to understand the mechanisms and characteristics of discharges into stagnant ambient water and/or crossflow conditions, Jirka et al. (1981) developed length-scale parameters for buoyant jets: the first classification of buoyant surface jets in crossflows was proposed by Chu and Jirka (1986). Additionally, Jones et al. (2007) introduced a comprehensive classification scheme and divided jets into four major classes: free jets, shoreline-attached jets, wall jets, and upstream intruding plumes. Free jets flow class are shown by FJ, when jets are not affected dramatically by the crossflow which indicates the relative stronger jet compared to crossflow. Free jets propagate into the crossflow ambient and bend gradually as they get carried downstream by the crossflow. They are the ideal condition for a surface discharge as they do not touch the shoreline. Shoreline-attached jets flow class are shown by SA, and are not as strong as free jets, relative to crossflow. They are bent right at the outlet of the discharged jet location and touch the shoreline in downstream. A recirculation zone could be generated downstream of the shoreline attached jets closer to shoreline. Wall jets are shown by WJ, and are not deflected by crossflow because of the discharging angle. Upstream intruding jets are shown by PL, and usually occur in the case of a highly buoyant jet in a crossflow with relatively small velocities. In this case, the surface jet velocity in lateral directions caused by buoyancy is relatively higher than that of the ambient crossflow. Upstream intruding jets are generated as a result of the higher lateral velocity of jet in upstream direction compared to crossflow velocity. Jones et al. (2007) also considered the deep and shallow ambient water classification depending on the bottom contact of the discharged jet.

Flow characteristics are denoted as:

$$Q_0 = \overline{u_0}a_0,\ \ M_0 = Q_0\overline{u_0},\ \ J_0 = Q_0 g_0',\ \ g_0' = g(\Delta\rho_0/\rho_a),\ \ R = u_0/u_a \tag{4.1}$$

where Q_0 is the jet flow rate, a_0 is the jet cross-sectional area, M_0 is the jet momentum flux, J_0 is the jet buoyancy flux, g_0' is the discharge buoyant acceleration, g is the gravitational acceleration ρ is the density of water, $\Delta\rho_0$ is discharge density difference ($\Delta\rho_0 = \rho_a - \rho_0$) and R is the jet-to-crossflow velocity ratio. The length scales defined for buoyant surface jet classifications (Jones et al., 2007; Wright Steven J., 1984) are shown in Table 4.1.

Table 4.1 Dynamic length scales of jets

Type of scale	Length scale
Discharge length scale	$L_Q = Q_0 / M_0^{1/2}$
Jet-to-plume length scale	$L_M = M_0^{3/4} / J_0^{1/2}$
Jet-to-crossflow length scale	$L_m = M_0^{1/2} / \overline{u_a}$
Plume-to-crossflow length scale	$L_b = J_0 / \overline{u_a}^3$

When surface jet discharges into the crossflow, significant transition processes occur. In the initial region in front of the nozzle (known as zone of flow establishment), flow velocity distribution transforms to a strongly sheared jet-like velocity distribution. The influence of the buoyancy in the jet-like region is negligible and flow is mainly controlled by the discharged jet momentum. Excess velocity and concentration profiles in this region follow a Gaussian distribution. When the momentum of the surface jet decreases, it bends towards the direction of the crossflow and the flow regime changes to a plume-like condition. Excess velocity and concentration profiles in the plume-like region have a more or less uniform distribution. Buoyancy effects and secondary flows are the only sources of mixing in the plume-like zone. All the above-mentioned regions form the near-field zone as the mixing is controlled mainly by initial discharge momentum and buoyancy flux. When surface jet reaches to the far-field, mixing is mainly controlled by the buoyant spreading or the passive diffusion.

Jirka (2007) developed an integral surface jet model (CorSurf), which was capable of simulating all flow classifications of jets in shallow and deep water conditions. He considered the turbulent entrainment of buoyant surface jets, which includes: horizontal entrainment, vertical entrainment, advected puff entrainment, frontal entrainment, and interfacial entrainment. The results from Jirka's model have been validated using results of a wide range of experiments and field studies.

Anwar (1987) conducted physical experiments to measure the vertical and horizontal isotherms of warm ($73°$ C) surface jets discharged from a rectangular channel into a cold ($15°$ C) crossflow with an R value of 1.11. He found that the jet axis was strongly depth-dependent and that the mutual deflection of the buoyant surface jet and the crossflow created a zone with overshoot velocity at the outer edge of the jet. They also captured a slow-moving zone on the lee side of the buoyant jet and a return flow closer to the inner wall (closer to the discharging point) of the flume. Gawad et al. (1996b) experimentally investigated the effects of horizontal surface and submerged jets in crossflows for buoyant and non-buoyant cases, and showed that both the excess jet velocity and concentration have similar Gaussian distributions in the lateral and vertical directions for cases where strong bank reattachment and recirculation do not occur.

A comprehensive review of the physical behaviour of vertical jets in crossflow conditions in incompressible and compressible flow regimes, focusing on experimental work, was conducted by Mahesh (2013). Andreopoulos and Rodi (1984) measured the three velocity components of vertical jets in crossflows with R values of $0.5, 1,$ and 2, using a three-sensor hot-wire probe, and indicated that a wake region with lower velocity was generated on the lee side of the jet and that the size of this region increased with an increase in the value of R. For lower values of R, the crossflow acted like a partial cover over the jet exit and created a non-uniform exit velocity profile. Later, Kelso et al. (1996) used phase-averaged flying-hot-wire measurements and smoke visualization to study the structure of a round jet in a crossflow, and introduced a graphical summary of vortex systems for a jet in a crossflow relating the range of phenomena to R and the Reynolds number (Re), which is defined as $\mathrm{Re} = ul/\upsilon$, where u is the velocity of the fluid, l is the characteristic linear dimension and υ is the kinematic viscosity of the fluid. Additionally, Camussi et al. (2002) conducted experimental studies of jets at very low Reynolds numbers ($Re \simeq 100$) by means of flow visualization and phase-averaged Particle Image Velocimetry (PIV). They detected two distinct flow regimes based on the value of R with a transitional value of $R \simeq 3$. Lai and Lee (2014) studied the inclined dense jet in perpendicular crossflows and found that the mixing behaviour is governed by crossflow Froude number (F), which is defined as $F = u/\sqrt{gl}$, where g is the gravitational acceleration. They found that the mixing is jet-dominated and governed by shear entrainment when $F < 0.8$ and the mixing is dominated by vortex entrainment when $F \geq 0.8$. Meftah et al. (2018) investigated the jet vortex structures in two distinct phases: rapid ascent phase and gradually descending phase. The experimental result confirmed the formation of CVP within the jet cross-section with opposite rotational direction for each phase. Similarly, Malcangio et al. (Malcangio, Ben Meftah, and Mossa, 2016; Malcangio, Ben Meftah, Chiaia, et al., 2016) studied the effects of currents on vertical buoyant and dense jets in crossflows and showed the importance of physical measurements in the complex jet-current hydrodynamic phenomena. Furthermore, several other studies related to vertical and inclined jets in crossflows have used PIV and Planar Laser Induced Fluorescence (PLIF) measurements (Luca Cortelezzi and Karagozian, 2001; Han et al., 2000; Han and Mungal, 2003; Haven and Kurosaka, 1997; Shan and Dimotakis, 2006; Shao and Law, 2010; Smith and Mungal, 1998; Thompson et al., 2016). However, the discharge of surface jets into crossflows has not been studied as extensively as that of vertical jets, and as such, further study of the discharge of surface jets in crossflows using accurate techniques is warranted.

The above-mentioned studies led to a better understanding of the complex flow structure of vertical jets in crossflows, and showed that these discharges generate four main types of vortices: counter-rotating vortex pairs (CVPs), horseshoe vortices, jet shear layer vortices, and wake vortices (Figure 4.1). Jets discharged in crossflows provide a higher mixing capability compared to free jets or mixing layers (Coussement et al., 2012b), and one of the reasons for this is the formation of CVP vortices as the jet expands downstream into the crossflow (Luca Cortelezzi and Karagozian, 2001). The wake vortices and shear-layer vortices are naturally unsteady and are eliminated from the velocity measurements by averaging over time. In contrast, the CVP and horseshoe vortices have a mean flow characterization in addition to their unsteady components (Fric and Roshko, 1994b).

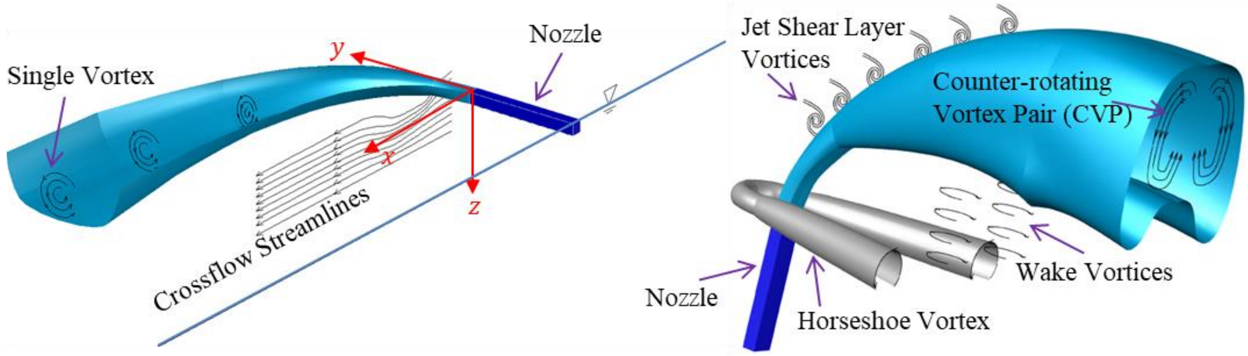

Figure 4.1 Schematic of surface jet (left) and submerged vertical jet (right) (Fric and Roshko, 1994b) in crossflow

In this study, estimating the turbulent kinetic energy and its dissipation rate helps to better understand the physics of turbulent flows. The energy dissipation rate is calculated from the derivatives of the velocity fluctuations, while the PIV method is used to capture the spatial and temporal variations of the velocity field. Finally, by extracting the gradient of the velocity fluctuations, one can quantify the turbulent dissipation rate (Doron et al., 2001; Hoque et al., 2015). This approach provides accurate information to quantify the turbulent flow, which affects the dispersion of surface jets in crossflows. The novelty of this study is that mean and turbulent flow characteristics of the jets were extracted in the mixing zone, which is useful for the study and design of the jet dispersion systems.

The purpose of this study is to provide a better understanding of the dispersion mechanisms of surface jets in crossflows. The authors investigated experimentally the instantaneous three-dimensional velocity distributions of surface jets in crossflows by using the Stereo-PIV technique. The Stereo-PIV measurement technique allowed to extract three-dimensional velocity fields on planes of measurement (2D3C). To the best knowledge of the authors, it is the first time Stereo-PIV measurement was used to study the mixing and flow structure of the surface jets in crossflows. Several planes of measurement have been selected to thoroughly investigate the mixing areas of jets, downstream of their discharge points.

The first section of the paper explains in detail the experimental setup and Stereo-PIV measurement techniques used in this study. Then, the experimental results are presented, analyzed, discussed, and interpreted. Subsequently, important turbulent flow characteristics such as the turbulent kinetic energy and the turbulent shear stress are calculated together with the turbulent kinetic energy dissipation rate and the eddy viscosity. Finally, a summary of the results and the concluding remarks are presented.

4.2 Experimental Setup and Procedure

In this study, a body of stagnant water was contained inside a glass flume with horizontal dimensions of $2.40 \times 1.1\ m^2$ and a depth of $0.50\ m$, referred herein as ambient water. The surface jet was generated by means of a nozzle with a square cross-section ($8 \times 8\ mm^2$) connected to a reservoir. The jet velocity distribution at the nozzle exit plays an important role in the jet downstream development (especially in the near field of the discharging point). In this study, the length of the horizontal section of the nozzle was sufficiently long (more than 12 times the nozzle width) to ensure that a well-controlled flow regime was discharged from the nozzle. Additionally, PIV measurements were conducted on the symmetry plane of the nozzle exit to ensure that the mean velocity distribution in front of the nozzle was fully developed for the selected jet Reynolds number ($Re = 9200$). This approach was also used by Shao and Law (Shao and Law, 2009). The nozzle's exit was positioned such that the jet direction was parallel to the surface of the ambient water. The horizontal section of the nozzle was set parallel to the water surface and top of the nozzle was located at the same elevation as the water surface while it was pulled along (Figure 4.2).

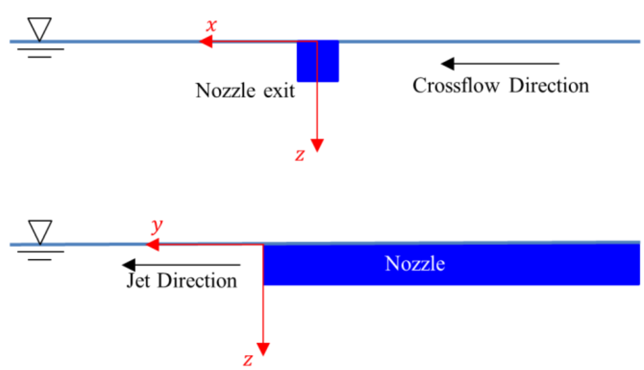

Figure 4.2 Location of the nozzle relative to the water surface

In order to reproduce a crossflow perpendicular to the discharged jet, the nozzle and Stereo-PIV cameras moved lengthwise along the flume through the stagnant water with the desired crossflow (current) velocity. This is a common approach in literature. As an example, Abessi and Roberts (2016) employed this approach to perform LIF measurements of the concentration distributions of submerged dense jets in crossflows. Wakes and surface waves were generated as the nozzle pulled along in these experiments. These wakes and surface waves are also observed in real cases of surface discharges intocrossflows when the crossflow flows past the discharging nozzles or channels. Since this is not the focus of this study, the measurement zone in this study was chosen such that it is not affected by these wakes and surface waves were generated because of the nozzle movement. The jet-to-crossflow velocity ratio ($R = 5.8$) was chosen such that it created a mixing zone away from these generated disturbances. Initial dye tests and PIV measurements without any discharge were performed to ensure that the chosen R was appropriate to achieve this goal.

The nozzle and the Stereo-PIV cameras were placed on a moving cart, which was driven by an electric motor (Figure 4.3). The system was calibrated with a series of tests checking a constant velocity of the moving cart in the domain of the results presented here. Warm water with a temperature (T) of 42.5 ℃ was discharged from the nozzle into colder ambient water with a temperature of 22.4 ℃. As the density of the jet was lower than that of the ambient water, the jet was positively buoyant in the ambient water. Constant discharging rate was achieved by creating a constant head reservoir and the temperature of the discharging warm water was measured at reservoir and in the nozzle exit point to make sure the experiments are in the same conditions. The main components of the experimental setup are shown in Figure 4.3. The location of the nozzle in surface discharges during the experiments is shown in Figure 4.3 (inset I). Green color of laser and the illuminated particles are also shown.

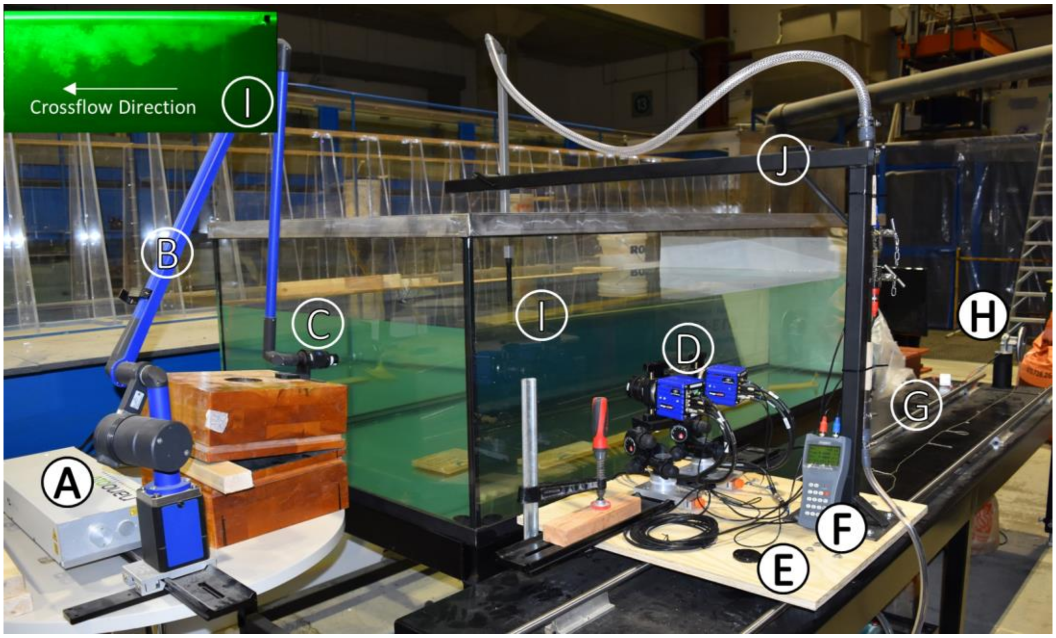

Figure 4.3 Experimental setup with main components: A) laser box for Stereo-PIV; B) laser delivery arm; C) laser lenses; D) scientific Complementary Metal Oxide Semiconductor (sCMOS) cameras; E) moving cart; F) ultrasonic flow meter; G) rails and supports; H) electric motor; I) nozzle; and J) discharging arm.

The instantaneous velocity components are u_1, u_2, and u_3, representing the velocities in the streamwise (longitudinal or x), span-wise (transverse or y), and vertical (z) directions, respectively (please see red arrows in Figure 4.1). The parameters related to the ambient water and the jet are subscripted by a and 0, respectively. As mentioned previously, the velocity of the moving cart simulating the crossflow current is in the x-direction referred here in as $\overline{u_a}$. The overbar indicates time-averaged variables. The Stereo-PIV system was used to measure the mean velocity of the crossflow, which was constant for the entire field of view ($\overline{u_a} \approx 0.12\ m/s$).

The length scales defined for buoyant surface jet classifications for this study are as follows: $L_Q = 0.008$, $L_M = 0.204$, $L_m = 0.043$ and $L_b = 0.002$. The flow in this study is classified as belonging to the FJ2 category (i.e., free jet in deep water with dominant crossflow).

The jet-to-crossflow and jet-to-plume length scales were used to determine the behaviour of the jet in a crossflow as well as the measurement zone used in this study. The measurement zone includes 6 different $x - z$ planes (y changes between L_m and L_M away from the jet exit). In this study, all the axes are non-dimensionalized by the jet exit width ($W = 8\ mm$), and the origin of the coordinates system ($x/W = 0,\ y/W = 0,\ z/W = 0$) was set at the water surface right in front of the nozzle (see Figure 4.2) such that the center of the nozzle was spatially located at $(0,0,{}^{1}/_{2})$. The closest plane was located at $y/W = 7.8$ from the nozzle exit, while the farthest one was located $y/W = 21$ away. For each plane, the area of measurement was at least $\Delta x/W = 22$ wide and $\Delta z/W = 7$ deep, depending on the experimental conditions of each plane. Details of the location of the planes are presented in Table 4.2 and shown in Figure 4.4. The mean values of the velocity presented in this study are calculated over at least 700 individual measurements and 2 or 3 round of experiment, for each of the six planes introduced in Table 4.2. The measurement zone in the current study was set such as to assess the flow structure of the zone of transition of the surface jet to a buoyant plume.

Table 4.2 Location of the planes of measurements

Plane	y/W	x/W	z/W
(A)	7.8	11.8 to 39.0	0.8 to 9.8
(B)	11.1	11.8 to 39.0	0.8 to 9.7
(C)	14.3	11.8 to 39.0	0.8 to 9.7
(D)	17.3	14.3 to 36.7	0.7 to 8.0
(E)	19.1	13.2 to 38.7	0.8 to 9.7
(F)	21.0	15.9 to 36.6	0.7 to 8.2

The location of these planes was selected with the intention of facilitating the extraction of the time-history of the jet velocity on the planes, which encompass the jet-mixing zone in the crossflow. A mixing zone is the region where the initial dilution of discharge occurs.

Each plane in Table 2 was measured in a different experiment with the same experimental conditions. Initial dye tests were performed to check that the jet did not reach the flume walls during the measurements, such that no reflection affected the experimental results. Figure 4.4 shows the top view of the dyed surface jet discharging in the crossflow and was obtained by using a camera whose field of views was set perpendicular to the water surface.

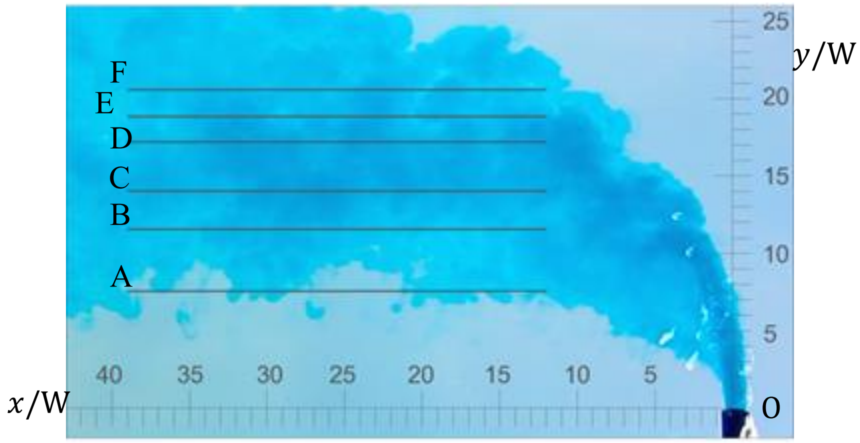

Figure 4.4 Plan view of the zone of measurement with the longitudinal projection of the $(x - z)$ measurement planes

4.3 Stereo-PIV Measurement Setup

The Stereo-PIV system employed in this study was a LaVision system, schematically shown in Figure 4.5. The data acquisition system and the processing of the Stereo-PIV measurements were performed using the DaVis 8.4 (proprietary) software. The laser arm emits light along the flume from one end of the flume to generate a laser plane at the locations selected for the jet velocity measurements. To prevent reflections of the laser light from the flume glass, the bottom and far end of the flume were covered by light-absorbent, dark material. The cameras for the Stereo-PIV measurements were located outside of the flume and directed to one side of the laser planes.

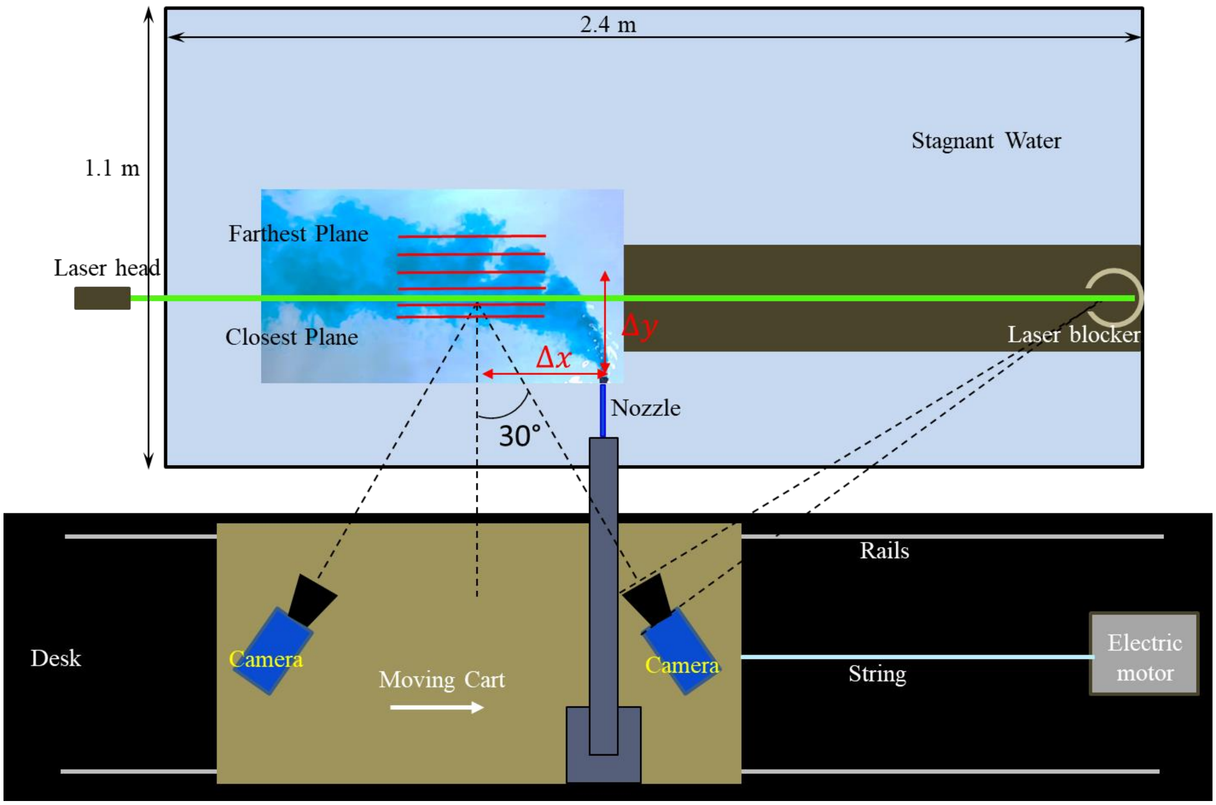

Figure 4.5 Plan view of the Stereo-PIV system layout (nozzle and the Stereo-PIV cameras on the cart moving in the direction of the arrow using the electric motor)

The Stereo-PIV measured the three components of velocity (u_1, u_2 and u_3) over the two-dimensional longitudinal ($x - z$) planes (2D3C), with the specifications mentioned in Table 4.2. Hollow glass particles with a diameter of 20 μm and a specific gravity of 1.1 were used as seeding particles and added to the ambient water and the jet. The seeding particle concentration was sufficient to use a cross-correlation algorithm for the Stereo-PIV calculations. The laser sheet thickness varied from 3 mm to 5 mm and was generated by two Nd-Yag pulsed laser beams (100 mJ per pulse at the wavelength of 532 nm) via an articulated light delivery arm. The time intervals between the laser shots was calculated based on the velocity of the flow, and ranged between 1 ms and 3 ms.

The images were obtained by two dual-frame sCMOS cameras with 1028×2560 pixel resolution at 40 fps and pixel size of 65×65 μm^2. The cameras captured two full-resolution frames in very quick succession, adequate for Stereo-PIV experiments with high-velocity flows and a lower frequency of velocity measurements. Each velocity measurement includes 4 different images from the two sCMOS cameras. The camera lenses have a $50\ mm$ focal length and $f/1.8$ aperture, where f is the focal length. The angle between each camera and the laser plane of measurement was $30°$ (shown in Fig. 4), which led to some of the seeding particles in the field of view to be out of focus. Scheimpflug adapters were used to ensure a uniformly focused image of the particles. The aperture of the cameras was chosen such that the light reflected from the seeding particles did not saturate the images.

The images captured using the Stereo-PIV system had to be mapped on the object plane. The object plane is the area in the flow directly in front of the calibration target. The aim of this step was to have an accurate mapping of the captured images to the object plane. A three-dimensional calibration target (two-level LaVision standard calibration plate) with white dots on the front and rear plane was used to scale and calibrate the recorded images. Polynomials of the 3rd order were used for this mapping. Additionally, stereo self-calibration of the images was conducted in order to minimize the errors caused by misalignment of the calibration plane and image plane (refer to Wieneke (2005) for more information on this procedure).

Fast-Fourier-transform based stereo cross-correlation algorithms were used for the experimental image pairs to evaluate the velocity distribution. Decreasing the interrogation window size with a multi-pass processing iteration scheme was used for image processing. The interrogation window sizes ranged from 128×128 pixels in a rectangular shape down to 64×64 pixels in a circular shape, with three refinement passes for each window size and a 50% overlap. High-accuracy modes for the final passes were used. Allowable vector range filter in addition to a median filter (Westerweel, 1994) were applied in the postprocessing of the vector fields, and a standard deviation filter was used to remove the spurious vectors.

4.4 Experimental Results and Discussions

The results of the mean velocity distributions for the jet velocity measurements along the longitudinal $(x - z)$ planes are shown in Figure 4.6.

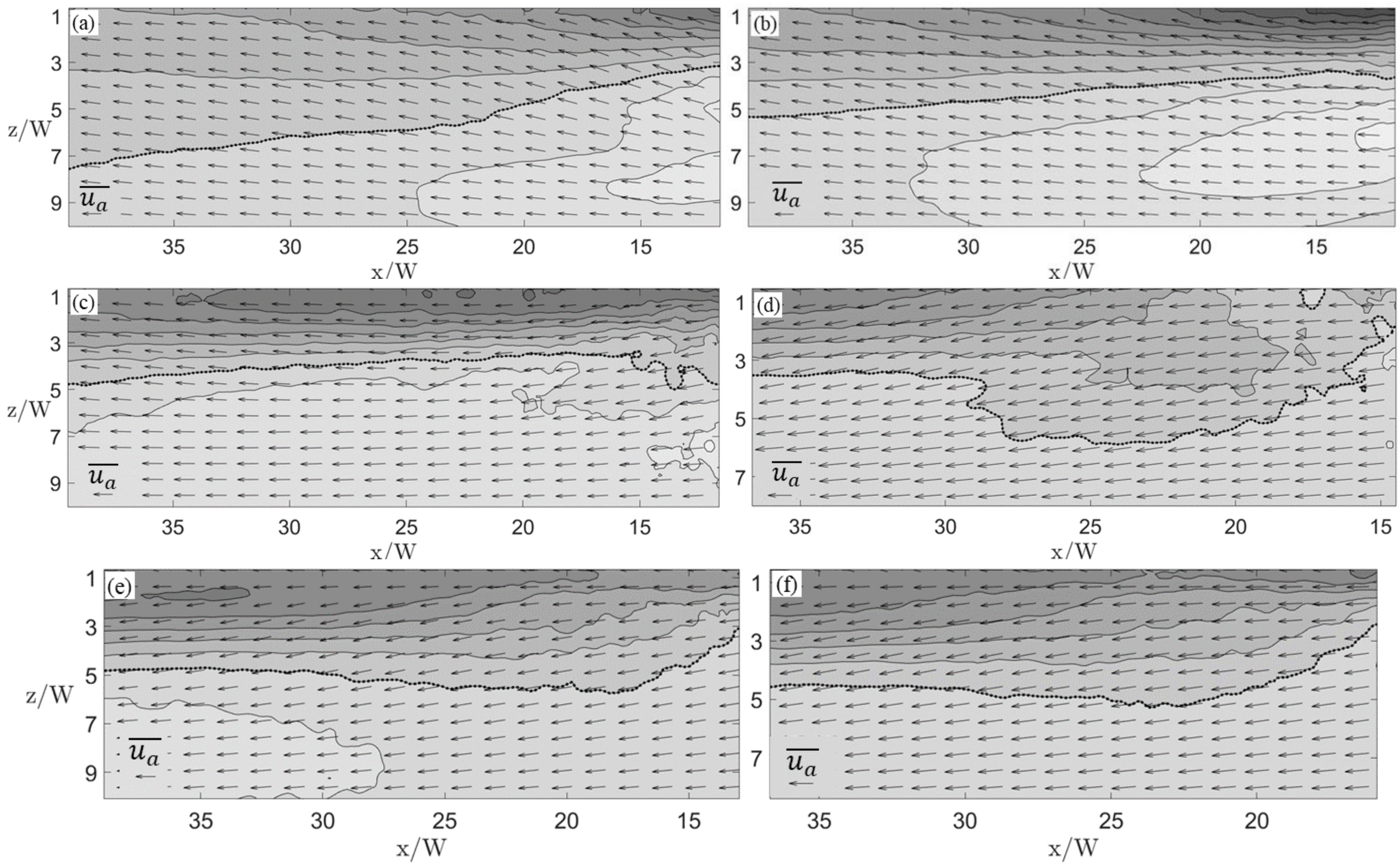

Figure 4.6 Mean jet velocity distributions: **a** at $y/W = 7.8$; **b** at $y/W = 11.1$; **c** at $y/W = 14.3$; **d** at $y/W = 17.3$; **e** at $y/W = 19.1$; and **f** at $y/W = 21.0$; (dotted contour line corresponds to $\overline{u_2} = 0$ and the positive values are shown in darker gray shades with the counter intervals of 0.01 (m/s), $\overline{u_a}$ are shown as vector to use as a vector scale)

The velocity components u_1 (streamwise) and u_3 (vertical) are the in-plane components and are shown by vectors in Figure 4.6a-f. The component u_2 represents the velocity in the transverse (y) direction (perpendicular to the planes of measurement) and is shown by the contour lines in the figure. The thick dotted line is the contour line corresponding to $\overline{u_2} = 0$ in Figure 4.6. Darker grey shades represent negative values of $\overline{u_2}$, while brighter grey shades indicate positive values of $\overline{u_2}$. Each contour interval is equal to 0.01 (m/s).

The transverse velocity contours in Figure 4.6 show the regions where the lateral gradient of $\overline{u_2}$ is maximum. These regions are in the interval $x/W = 12$ to $x/W = 25$ near the discharge point for the case of the planes closer to the cameras (such as (A), (B) and (C)). However, the lateral gradient of $\overline{u_2}$ happens in the regions between $x/W = 30$ to $x/W = 36$ downstream of the jet axis at the farther planes of measurements (such as (D), (E) and (F)). The high gradient of $\overline{u_2}$ at these regions leads to velocity fluctuations, and, implicitly, to higher turbulent kinetic energy. This increases the mixing capability of the jet. The three-dimensional evolution of the mean velocity components is illustrated in Figure 4.7.

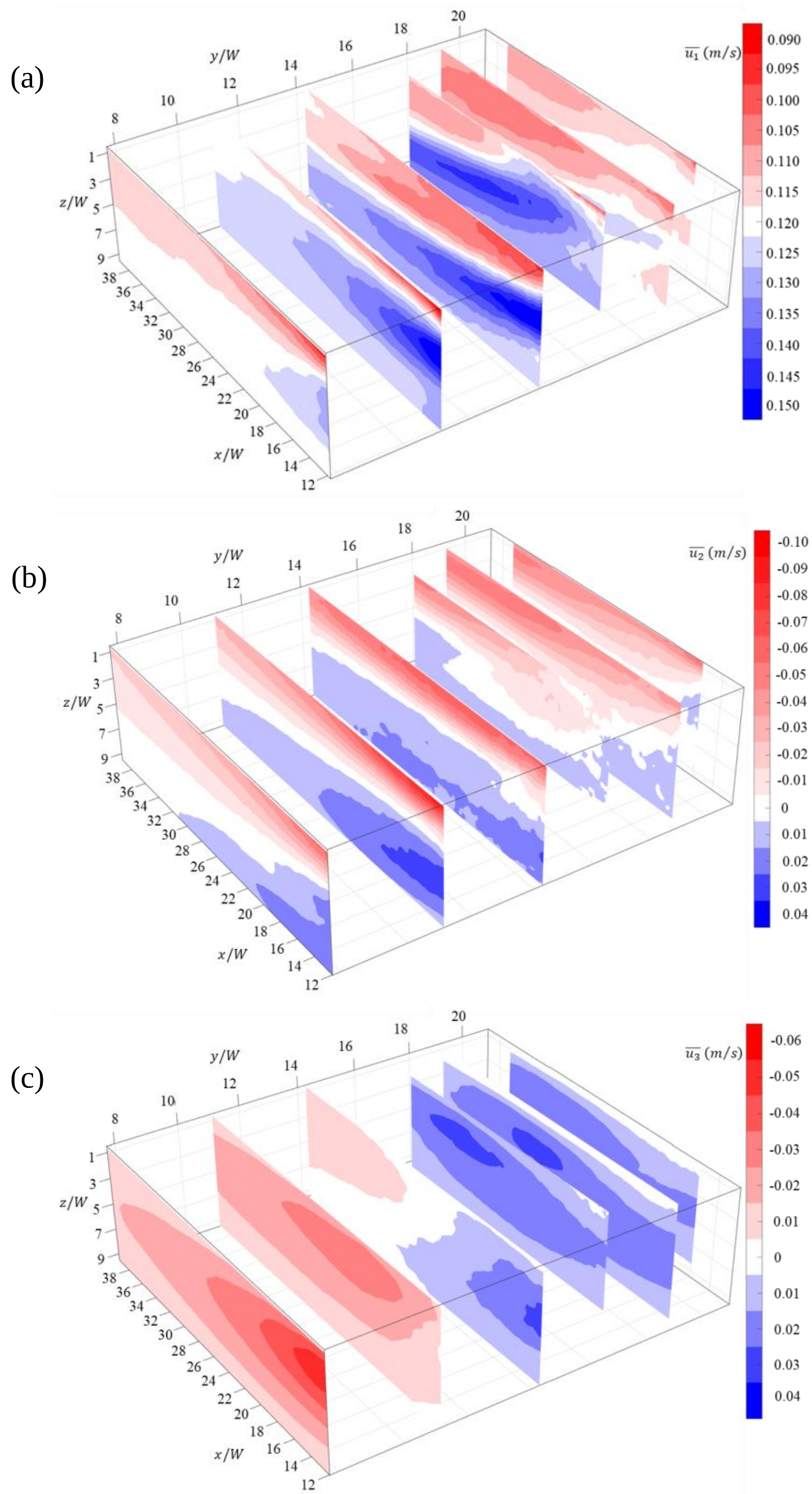

Figure 4.7 Contours of the mean velocity components: **a** $\overline{u_1}$; **b** $\overline{u_3}$; and **c** $\overline{u_2}$

The evolution of the streamwise velocity contours ($\overline{u_1}$) in Figure 4.7a show that, maximum deviation of $\overline{u_1}$ from mean crossflow velocity $\overline{u_a}$, occurs in the middle of the measurement zone, in the regions closer to the discharging point.

Figure 4.7b shows that the maximum magnitude of the transverse velocity ($\overline{u_2}$) occurred in the regions close to the water surface in all planes of measurement, and then decreased as the jet expanded downstream. The maximum magnitude of the $\overline{u_2}$ contours in plane (B) is of $0.09\ (m/s)$, and has the same direction as the initial jet velocity. This occurred at a water depth of $z/W = 1$, and then changed to $0.05\ (m/s)$ in plane (F) as the jet expanded to a water depth of $z/W = 2.1$.

It is important to note the changes in the sign of the vertical velocity from negative (upward) to positive (downward) in the measurement planes (see Figure 4.7c). The maximum magnitude of the vertical velocity ($\overline{u_3}$) is $0.05(m/s)$, and is shown in red (water moves toward the water surface) as occurring at a depth of $z/W = 3$ in plane (A). Positive values of $\overline{u_3}$ show the movement of water away from the water surface at a depth of $z/W = 5$ at planes (D) and (E), as shown in blue shade in Figure 4.7c. In the middle of the mixing zone (plane (C)), both positive and negative vertical velocities were observed at the same plane.

The location of the maximum mean streamwise velocity ($\overline{u_1}$) is described by:

$$z/W = M\ (x/W)^N \tag{4.2}$$

where M and N are non-dimensional constants (same equation used in (Anwar, 1987) for surface buoyant jets). Using the least-square linear regression over the four middle planes of measurement led to the values of M and N described in Eq. (4.2). These non-dimensional constants, i.e., the correlation coefficient of the fitted curve ($\hat{r}$) and the range of the region (x/W) that they were applicable to, are summarized in Table 4.3.

Table 4.3 Non-dimensional coefficients used in Eq. (4.2)

Plane	x/W	M	N	$\hat{r}$
(B)	11.8 to 24	1.817	0.309	0.693
(C)	11.8 to 39	1.791	0.395	0.975
(D)	16.5 to 36.7	0.159	1.033	0.985
(E)	13.2 to 38.7	0.633	0.721	0.985

Equation (4.2) can be effectively used (for values of $\hat{r}$ greater 0.975) to estimate the location of the maximum magnitude of $\overline{u_1}$. For example, the contours of $\overline{u_1}$ for plane (C) are shown in Figure 4.8. The dashed line in Eq. (4.2) is the fitted curve, while the red ones are sections perpendicular to the curve which was further used to extract the varying parameters of the flow characteristics along the jet as it propagated downstream.

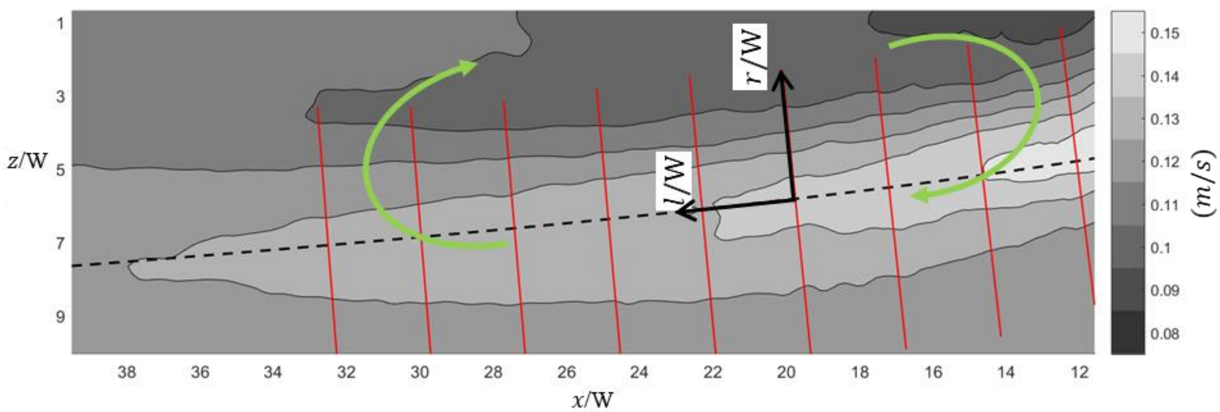

Figure 4.8 Contours of the mean streamwise velocity, $\overline{u_1}$, at plane (C)

The maximum value of the streamwise velocity ($\overline{u_1}$) is measured as 0.15 (m/s) in plane (C), and the minimum velocity of $\overline{u_1}$ is 0.09 (m/s) in the same plane. Notably, the average value of the minimum and maximum $\overline{u_1}$ in almost all the planes of measurement is close to the value of the crossflow velocity ($\overline{u_a}$). This implies the occurrence of circulation in plane (C) with excess velocity ($u^* = \overline{u_1} - \overline{u_a}$) of ± 0.03 (m/s) which was carried by the crossflow away from the jet and stretched over a larger area (see the curved arrows in Figure 4.8). This circulation caused a higher degree of mixing between the jet and the ambient water and enhanced the dilution factor of the mixing zone.

The isosurfaces for $\overline{u_1}$ in Figure 4.9 show the evolution of the streamwise velocity. Lower magnitude streamwise velocity in the regions closer to the water surface created a slow-moving flow zone. This occurred due to the blockage of the crossflow by the surface jet with high momentum in the y-direction. Additionally, because of this blockage, crossflow is redirected to underneath the jet and created a zone with higher streamwise velocity deeper in the water.

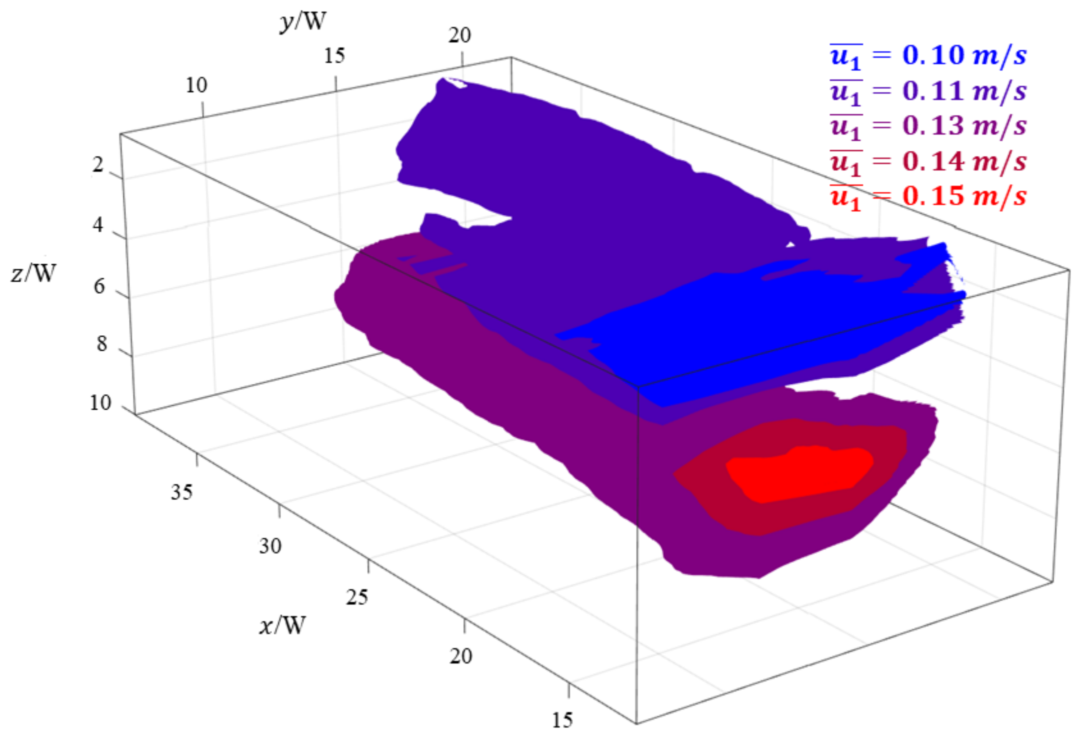

Figure 4.9 Isosurfaces of $\overline{u_1}$

In order to obtain the velocity distribution in the $y - z$ planes, the results of the linear interpolation of the data are calculated over the zone of measurement. Flow streamlines in the measurement zone are shown in Figure 4.10. The streamlines in the $x - z$ planes which show the changes in the crossflow as a result of the surface discharge (Figure 4.10a) are generated using u^* and $\overline{u_3}$. The streamlines in plane (C) reveal that circulation occurred in the middle of the measurement zone at $(24, 3, 14.3)$, which explains the change in sign for $\overline{u_3}$ as previously mentioned. These flow features reveal the three-dimensional evolution of $\overline{u_3}$. The source of this circulation may be due to the blockage of the crossflow by the jet as the effect of this blockage was also clear in the isosurfaces of $\overline{u_1}$. As a result of this blockage, the streamlines of the crossflow bend away from the water surface and after passing the surface jet start to return to the surface; this is also shown in Figure 4.10a at plane $y/W = 11.1$. The center of this circulation moves in the measurement zone from $(12, 2, 11.1)$ in plane (B) to $(39, 5, 17.3)$ in plane (D).

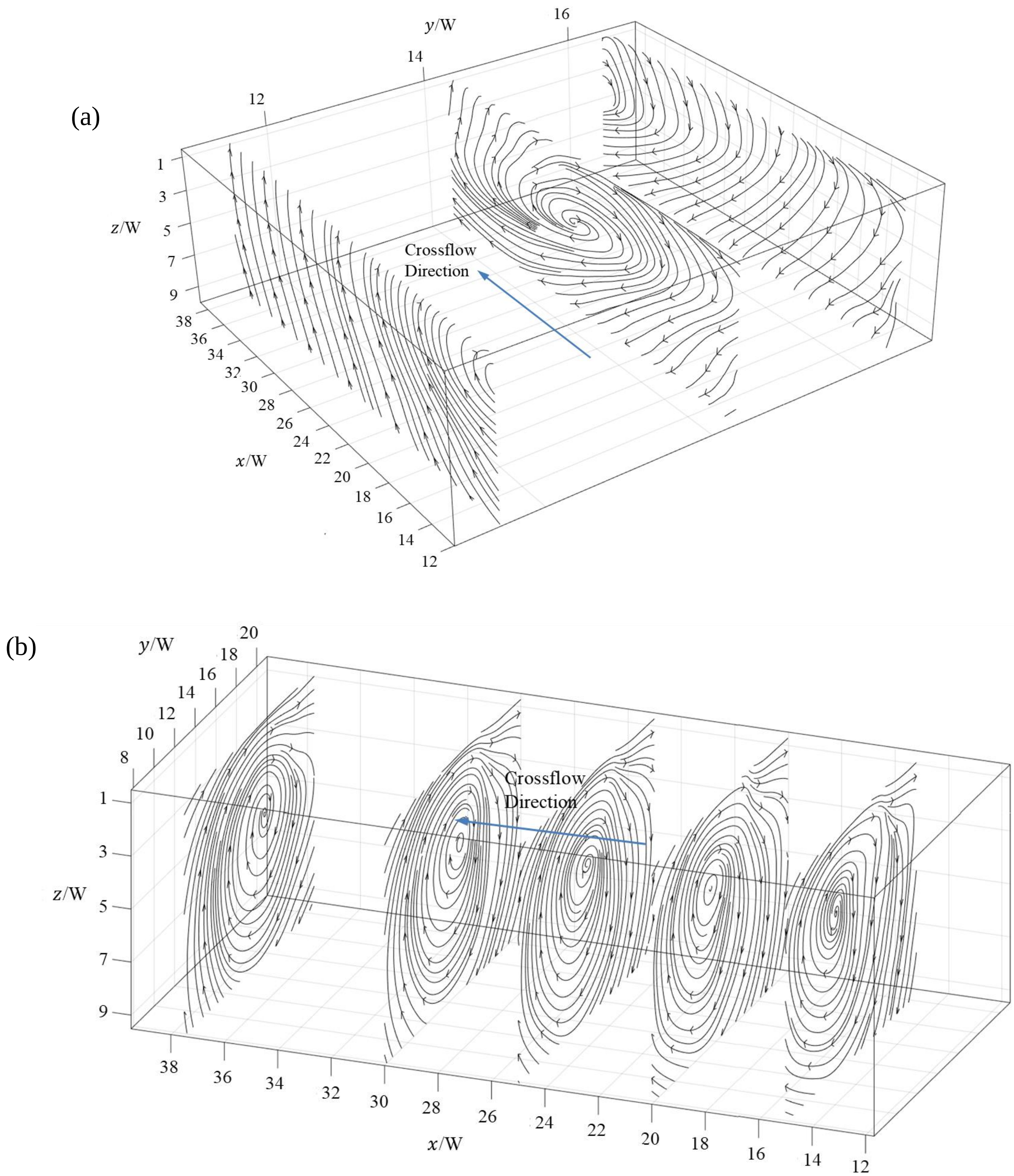

Figure 4.10 Mean excess velocity streamlines along the $y-$ axis **a** and mean velocity streamlines along $x-$ axis **b**

Another circulation pattern was generated perpendicular to the planes of measurement and is illustrated in the $y-z$ planes shown in Figure 4.10b. This circulation is similar to a Counter-rotating Vortex Pair (CVP) in the case of vertical jets in crossflows. The most notable difference with a CVP is the existence of the vortex pair (one on each side of the plane of symmetry) which occurred about the plane of symmetry in vertical jets compared to the single circulation (vortex) of surface jets. One can hypothesize that the presence of the water surface eliminates one of the vortices of a CVP and acts like a plane of symmetry for the flow structure. The maximum flow velocity in this vortex occurred closer to the water surface. This vortex propagated downstream and slowly moved in the transverse (y) direction from the discharge point, and remained in the flow structure in the zone of measurement. The center of the vortex moves $3.5W$ in the transverse direction as it moves between the first and last sections: i.e., moves from point $(15, 3.5, 12)$ to $(37.5, 4, 15.5)$, as shown in Figure 4.10b. The maximum magnitudes of the vortex velocities occurred in the z-direction and in the regions closer to the water surface, and they were higher in the sections closer to the discharge point. Also, the maximum magnitude of the vortex velocity dropped from 12% of the initial jet speed at $x/W = 12.5$ to 8% at $x/W = 35$. Additionally, this vortex enhanced the mixing capability of the jet while it propagates in the crossflow, as this was the dominant motion after the jet lost momentum in the far field. The reduction in velocity demonstrates the loss of jet momentum and consequently the initial concentration.

In summary, these two vortices induced the circulation observed in the turbulent zone and enhanced mixing by vertical and transverse entrainment of the surrounding fluid into the jet. The vortex in the $y - z$ plane plays an important role in the transverse mixing and causes most of the scalar mixing in the flow by large-scale momentum transport, similar to a CVP in vertical jets in a crossflow (Luca Cortelezzi and Karagozian, 2001; Hasselbrink and Mungal, 2001a; b; Zhang and Yang, 2017).

4.5 Turbulent Flow Characteristics

4.5.1 Turbulent Kinetic Energy and Turbulent Stresses

The velocity fluctuations (u') are extracted for each measurement such that $u = \overline{u} + u'$. The six independent turbulent stress terms ($\overline{u'_i u'_j}$) were extracted from the measured data, and the mean values of the three normal stress terms ($\overline{u_i'^2}$) are shown in Figure 4.11. These values were used to calculate the turbulent kinetic energy as follows:

$$\overline{k} = {}^1/_2 \left(\overline{u_1'^2} + \overline{u_2'^2} + \overline{u_3'^2} \right) \tag{4.3}$$

where $\overline{k}$ is the mean turbulent kinetic energy.

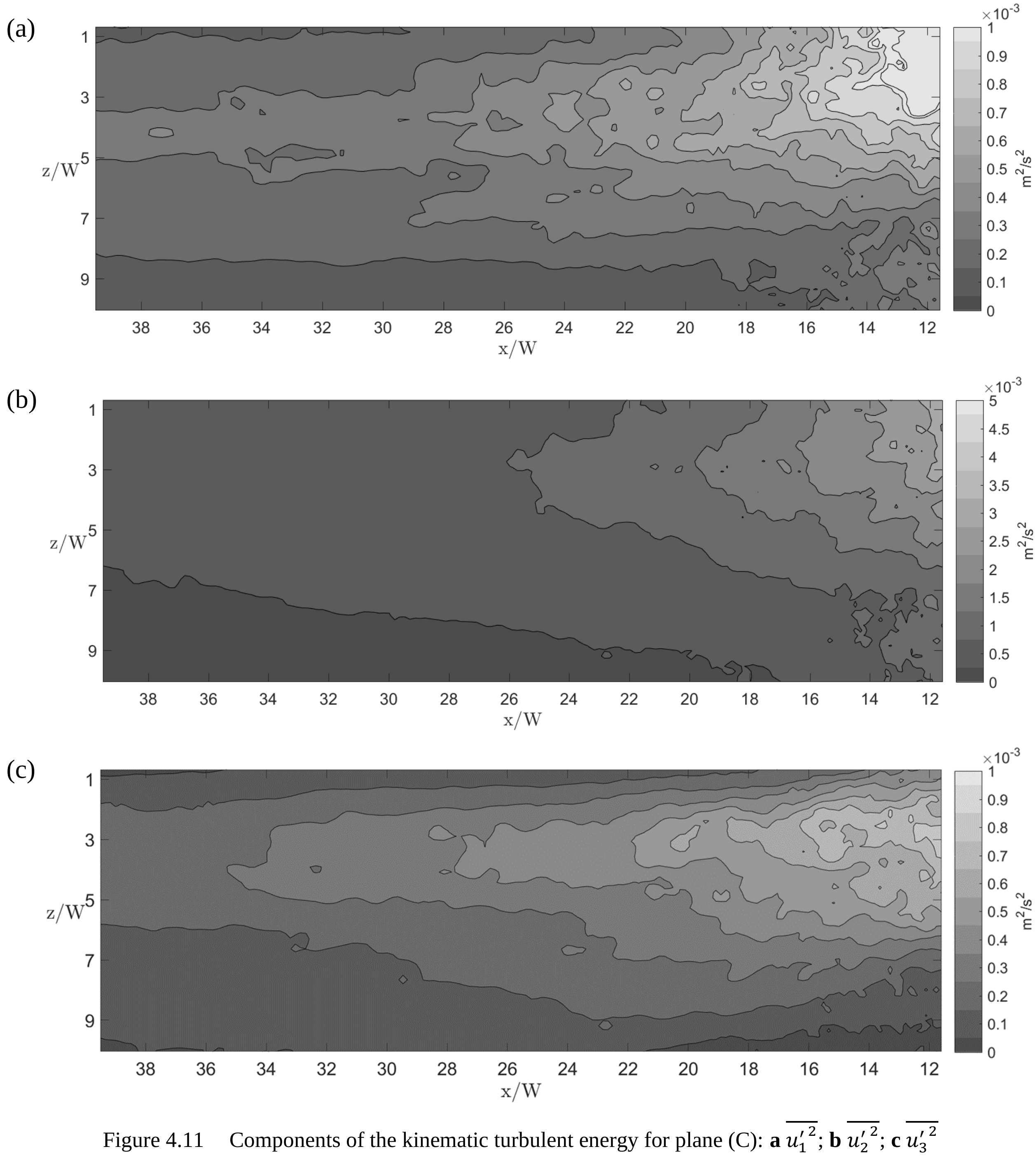

Figure 4.11 Components of the kinematic turbulent energy for plane (C): **a** $\overline{u_1'^2}$; **b** $\overline{u_2'^2}$; **c** $\overline{u_3'^2}$

The largest magnitudes of $\overline{u_i'^2}$ occurred at locations with high velocity gradients. The maximum magnitude of $\overline{u_2'^2}$ (Figure 4.11b) was approximately four times larger than the other two turbulent kinetic energy components ($\overline{u_1'^2}$ and $\overline{u_3'^2}$) of $\overline{k}$ at plane (C). This implies that the structure of the turbulence was anisotropic in the y-direction compared to the x and z-directions. As a result, the mean turbulent kinetic energy was shown to exhibit a similar distribution to that of $\overline{u_2'^2}$, especially for the regions closer to the discharge point (Figure 4.11b and Figure 4.12). It is important to note that u_2' is one of the main velocity components of the vortex in the $y-z$ plane. The same trend was also observed for the other planes of measurement. The maximum magnitude of $\bar{k}$ is 0.003 (m^2/s^2), occurred at planes (C) and (D). The locus of the maximum $\bar{k}$ occurred at the same location as the center of the two types of vortex observed in the flow structures (i.e., the vortex in the $y-z$ plane and the vortex that causes the excess streamwise velocity in the $x-z$ plane). This demonstrates that the flow was highly turbulent with high mixing capabilities in this region.

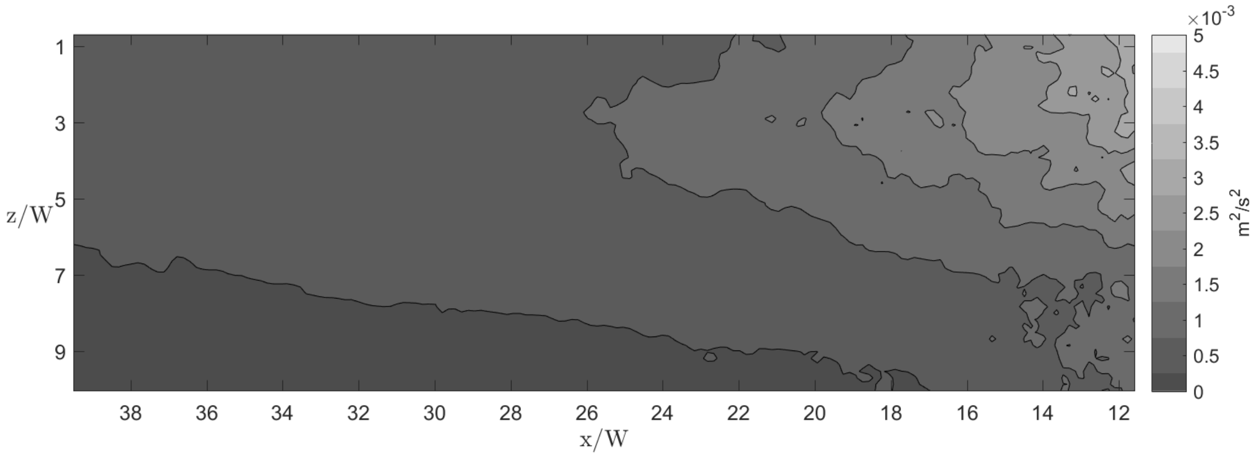

Figure 4.12 Mean turbulent kinetic energy $\bar{k}$ at plane (C)

The three tangential shear stress terms for plane (C) are shown in Figure 4.13. Large negative magnitudes of $\overline{u'_1u'_3}$ were found at the initial region closer to the water surface (darker grey shades in Figure 4.13a), while below this zone, high positive magnitudes were found (brighter grey shades in Figure 4.13a). The region of negative $\overline{u'_1u'_3}$ expanded in the vertical direction as the jet spread downstream into the crossflow. This observation is in agreement with the results of Mungal and Su (Su and Mungal, 2004). These stresses are produced from the span-wise vorticity present in the flow which is due to the Kelvin-Helmholtz instability (Yuan et al., 1999). The other two tangential shear stresses ($\overline{u'_2u'_3}$ and $\overline{u'_1u'_2}$) are twice larger than $\overline{u'_1u'_3}$. As an example, the maximum magnitude of $\overline{u'_2u'_3}$ is 0.0004 (m^2/s^2) in Figure 4.13b compared to maximum magnitude of $\overline{u'_1u'_3}$ (0.0002 (m^2/s^2)).

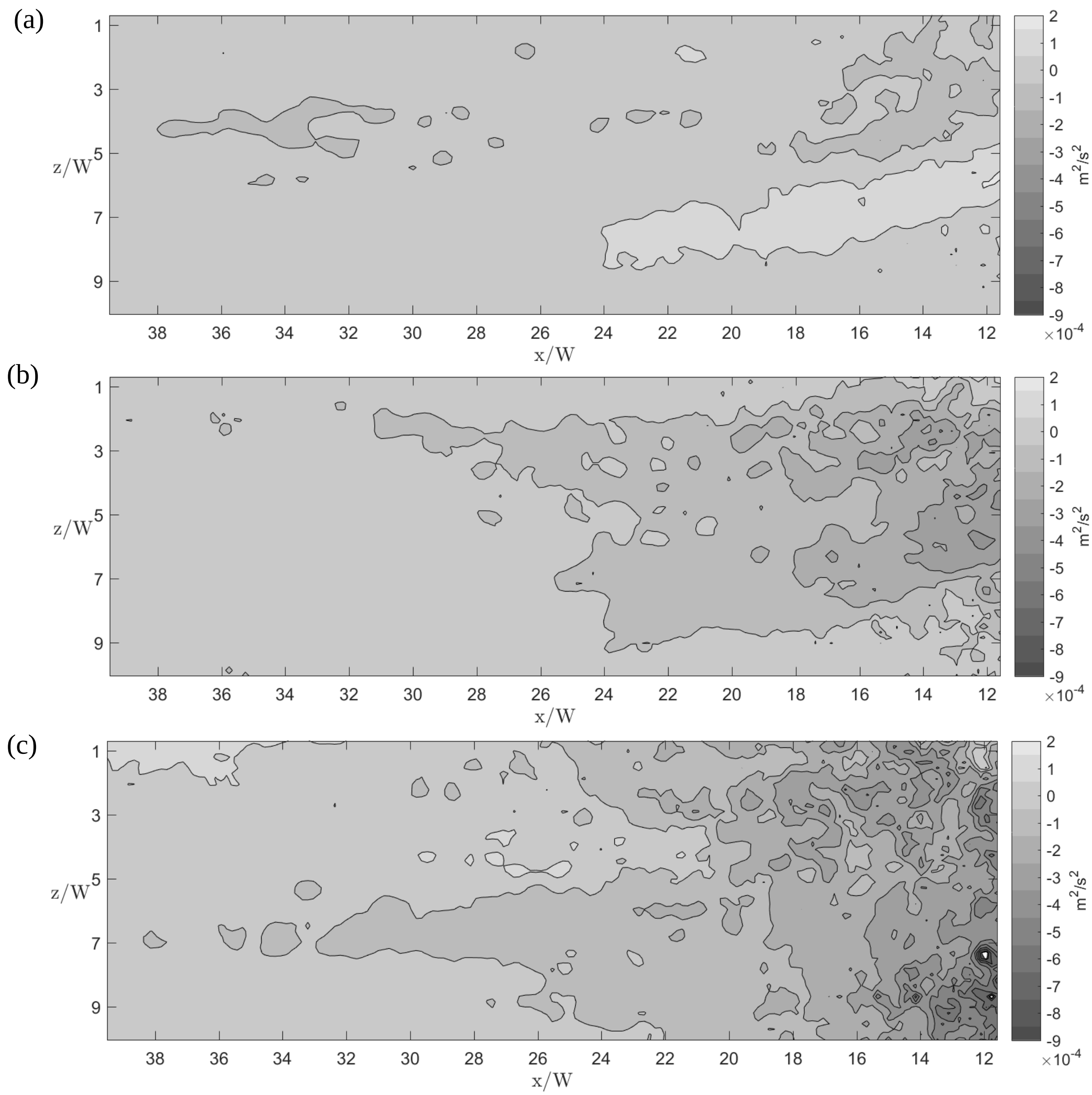

Figure 4.13 Components of turbulent shear stress at plane (C): **a** $\overline{u'_1u'_3}$; **b** $\overline{u'_2u'_3}$; and **c** $\overline{u'_1u'_2}$

The values of the streamwise excess velocity are extracted for several sections perpendicular to the fitted curve introduced previously in Eq. (4.2) for different planes of measurement (Figure 4.14a). The horizontal axis represents the non-dimensional distance (r/W) from the location where the maximum value of $\overline{u_1}$ occurs along the x-axis in each plane of measurement. Red doted curves in Figure 4.14 are closer to the discharging point and blue dotted curves are further from it. The positive value of r/W is related to the regions closer to the water surface, as shown in Figure 4.8. The normalizing scales are the maximum local excess velocity (u^*_{max}) for u^* and $\overline{u_a}^2$ for the normal and tangential shear stresses.

A clear asymmetrical trend exists in the normalized streamwise excess velocity (u^*/u^*_{max}) in the sections along planes (B) and (C), as shown in Figure 4.14a. This trend shows that the flow is self-preserving. The drop in u^*/u^*_{max} is much higher in the zones closer to the water surface (from 1 to -1) compared to the zones in deeper in the water (from 1 to 0). This trend changes as the jet bends and loses the initial momentum in planes (D) and (E), and it appears more symmetrical. Higher magnitudes of the normal shear stress were observed in the sections closer to the discharge point (red colors in Figure 4.14b) and these generated a higher degree of mixing in the flow as a result of the higher gradient of streamwise velocity. The value of non-dimensional Reynolds shear stresses ($u_1'u_3'/\overline{u_a}^2$) in Figure 4.14c ranged from -0.01 to 0.01. This range is comparable with similar experimental investigations of jets in crossflows (e.g., data measured by Coletti et al. (2013)). The value of $u_1'u_3'/\overline{u_a}^2$ is maximum in the regions located between r/W from 1 to 3 and is zero at $r/W = 0$ in all the planes of measurements.

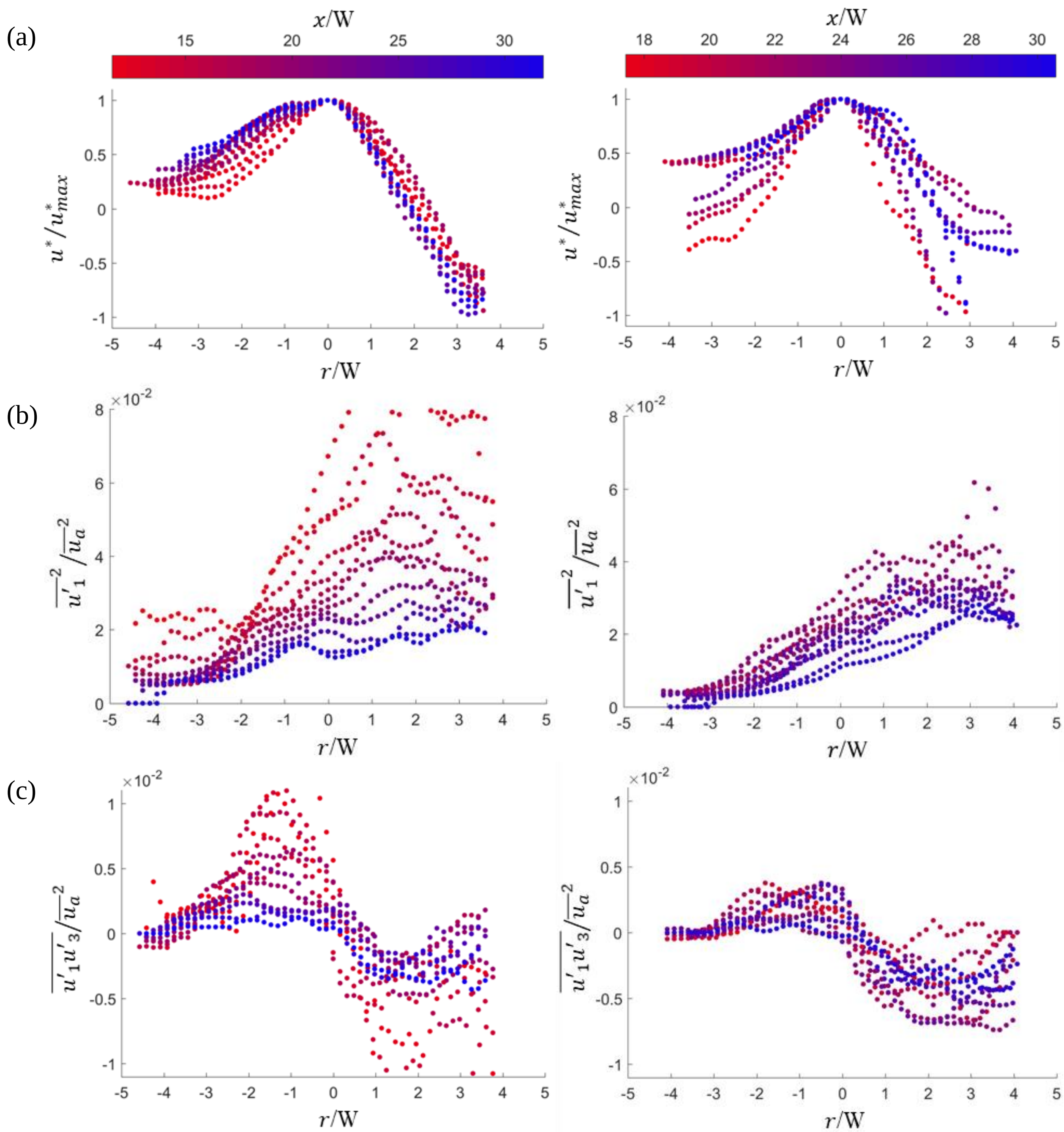

Figure 4.14 Non-dimensional profiles of streamwise mean excess velocity **a**, normal **b** tangential and **c** shear stresses. Planes (B) and (C) in the left side graphs while planes (D) and (E) are shown in the right side graphs

4.5.2 Turbulent Kinetic Energy Dissipation Rate and Eddy Viscosity

The turbulent kinetic energy dissipation rate (ϵ) was calculated using the Stereo-PIV data. The main equation for the turbulent kinetic energy dissipation rate, ϵ, for a Newtonian fluid is:

$$\epsilon = \frac{1}{2}\upsilon\overline{\left(\frac{\partial u_i'}{\partial x_j}+\frac{\partial u_j'}{\partial x_i}\right)^2} = \upsilon\left\{\begin{array}{c} 2\left(\overline{\left(\frac{\partial u_1'}{\partial x_1}\right)^2}+\overline{\left(\frac{\partial u_2'}{\partial x_2}\right)^2}+\overline{\left(\frac{\partial u_3'}{\partial x_3}\right)^2}\right) \\ +2\left(\overline{\frac{\partial u_1'}{\partial x_2}\frac{\partial u_2'}{\partial x_1}}+\overline{\frac{\partial u_1'}{\partial x_3}\frac{\partial u_3'}{\partial x_1}}+\overline{\frac{\partial u_2'}{\partial x_3}\frac{\partial u_3'}{\partial x_2}}\right) \\ +\overline{\left(\frac{\partial u_1'}{\partial x_2}\right)^2}+\overline{\left(\frac{\partial u_2'}{\partial x_1}\right)^2}+\overline{\left(\frac{\partial u_1'}{\partial x_3}\right)^2} \\ +\overline{\left(\frac{\partial u_3'}{\partial x_1}\right)^2}+\overline{\left(\frac{\partial u_2'}{\partial x_3}\right)^2}+\overline{\left(\frac{\partial u_3'}{\partial x_2}\right)^2} \end{array}\right\} \tag{4.4}$$

where υ is the kinematic viscosity of the fluid, u_i' are the oscillatory components of the velocity, and x_i are the coordinates in the Cartesian frame. In order to estimate ϵ, a common approach (Doron et al., 2001; Fincham et al., 1996; Xu and Chen, 2013) is to extract the derivatives of the velocity components ($\frac{\partial u_i'}{\partial x_j}$) directly from captured PIV data. In planar PIV (two-dimensional measurements with two components or 2D2C), only $5/12$ of the constitute terms are calculated directly from the measured data. Also, by considering the continuity equation, one can use:

$$\frac{\partial u_2'}{\partial x_2} = -\left(\frac{\partial u_1'}{\partial x_1}+\frac{\partial u_3'}{\partial x_3}\right). \tag{4.5}$$

The other 6 terms (missing velocity gradients) of Eq. (4.4) are estimated by adopting the local isotropy assumption introduced by Doron, Bertuccioli, Katz and Osborn (2001). The local isotropy assumption implies that all lateral fluctuations have similar average magnitudes locally, which requires the turbulent fluctuations to be statistically uniform in all directions. Here, as the jet is far from the boundaries, the authors used this simplified assumption to facilitate the study of the turbulent flow. The local isotropy assumption assumes that:

$$\overline{\left(\frac{\partial u_1'}{\partial x_2}\right)^2} = \overline{\left(\frac{\partial u_2'}{\partial x_1}\right)^2} = \overline{\left(\frac{\partial u_3'}{\partial x_2}\right)^2} = \overline{\left(\frac{\partial u_2'}{\partial x_3}\right)^2} = \frac{1}{2}\left[\overline{\left(\frac{\partial u_1'}{\partial x_1}\right)^2}+\overline{\left(\frac{\partial u_3'}{\partial x_3}\right)^2}\right] \tag{4.6}$$

$$\overline{\frac{\partial u_1'}{\partial x_3}\frac{\partial u_3'}{\partial x_1}} = \overline{\frac{\partial u_2'}{\partial x_3}\frac{\partial u_3'}{\partial x_2}} = \overline{\frac{\partial u_1'}{\partial x_2}\frac{\partial u_2'}{\partial x_1}}. \tag{4.7}$$

By substituting Eqs. (4.5)-(4.7) into Eq. (4.4), ϵ can be expressed as:

$$\epsilon = \upsilon \left\{ \begin{array}{c} 4\left(\overline{\left(\frac{\partial u_1'}{\partial x_1}\right)^2} + \overline{\left(\frac{\partial u_3'}{\partial x_3}\right)^2} + \overline{\frac{\partial u_1'}{\partial x_1}\frac{\partial u_3'}{\partial x_3}}\right) + 3\left(\overline{\left(\frac{\partial u_1'}{\partial x_3}\right)^2} + \overline{\left(\frac{\partial u_3'}{\partial x_1}\right)^2}\right) \\ +6\left(\overline{\frac{\partial u_1'}{\partial x_3}\frac{\partial u_3'}{\partial x_1}}\right) \end{array} \right\}. \tag{4.8}$$

In the case of Stereo-PIV measurements, terms such as $\frac{\partial u_2'}{\partial x_3}$ and $\frac{\partial u_2'}{\partial x_1}$ can be calculated directly from the measured components of velocity. After inserting the above mentioned terms into Eq. (4.8), one obtains:

$$\epsilon = \upsilon \left\{ \begin{array}{c} 4\left(\overline{\left(\frac{\partial u_1'}{\partial x_1}\right)^2} + \overline{\left(\frac{\partial u_3'}{\partial x_3}\right)^2} + \overline{\frac{\partial u_1'}{\partial x_1}\frac{\partial u_3'}{\partial x_3}}\right) + 2\left(\overline{\left(\frac{\partial u_1'}{\partial x_3}\right)^2} + \overline{\left(\frac{\partial u_3'}{\partial x_1}\right)^2}\right) \\ +6\left(\overline{\frac{\partial u_1'}{\partial x_3}\frac{\partial u_3'}{\partial x_1}}\right) + \overline{\left(\frac{\partial u_2'}{\partial x_1}\right)^2} + \overline{\left(\frac{\partial u_2'}{\partial x_3}\right)^2} \end{array} \right\} \tag{4.9}$$

The accuracy of the calculated ϵ in this case is higher compared to the case using the planar PIV data (Delafosse et al., 2011; Xu and Chen, 2013) due to the existence of the in-plane distribution of the third component of the velocity field. Additionally, the local isotropy assumptions used in Eq. (9) are weaker than for Eq. (4.8). The value of ϵ calculated from Eq. (4.9) from the measured Stereo-PIV data is almost 1.5 times larger than the ϵ value calculated from Eq. (4.8), which shows that the local isotropy assumption to replace $\overline{\left(\frac{\partial u_2'}{\partial x_1}\right)^2}$ and $\overline{\left(\frac{\partial u_2'}{\partial x_3}\right)^2}$ is too conservative in this case. This confirms that the structure of the turbulence is anisotropic, as previously mentioned. It is shown in Figure 4.15b that the values of ϵ is 1.5 times larger compared to values shown in Figure 4.15a in the regions with relatively higher mean velocity gradient. For instance, the value of ϵ is $0.4 \times 10^{-3}\ m^2/s^3$ and $0.6 \times 10^{-3}\ m^2/s^3$ at $(x/W = 21,\ z/W = 3)$ in Figure 4.15a-b, respectively. The maximum magnitudes of ϵ calculated with both methods occurred in the regions where the flow was highly turbulent ($z/W = 2$) at the beginning of the measurement zone ($x/W = 12$). The maximum magnitudes of k and ϵ arise in the same regions with the highest mean velocity gradient values, which indicates the close connection between the turbulence production, turbulence dissipation, and mean shear flows.

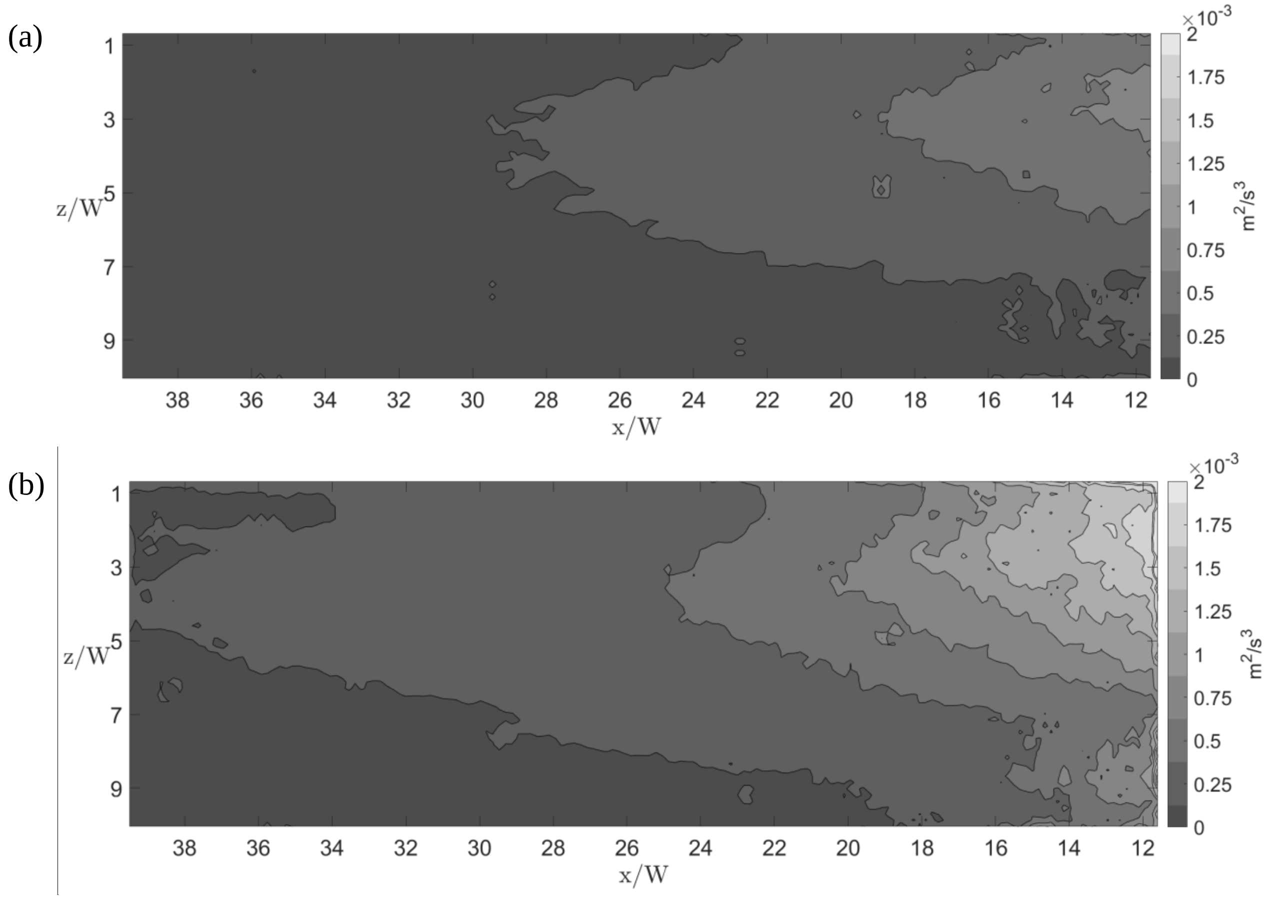

Figure 4.15 Variation of ϵ at plane (C) using **a** in-plane data and **b** Stereo-PIV data

The turbulent eddy viscosity (υ_t) can be calculated from k and ϵ from:

$$\upsilon_t = c_\mu \frac{k^2}{\epsilon} \tag{4.10}$$

where $c_\mu = 0.09$ is a constant in the closure.

The distribution of the calculated turbulent eddy viscosity at plane (C) is illustrated in Figure 4.16. The maximum value of υ_t is $5 \times 10^{-4}\ m^2/s$ in the measurement zone, and it occurred in the center of the mixing zone (between planes (B) and (C)) as a result of the highly turbulent flow. The minimum values of υ_t occurred outside this region, in planes (A) and (F).

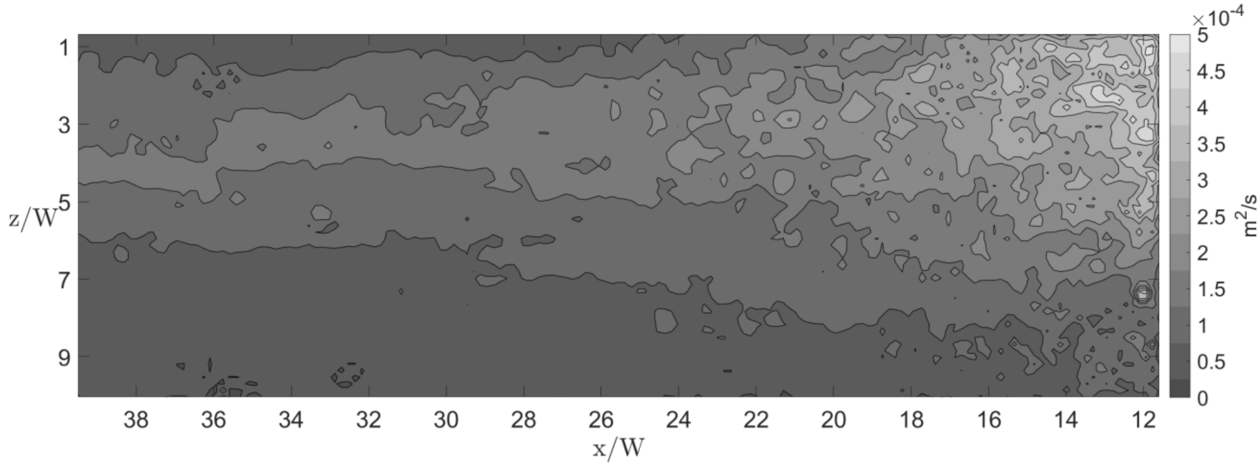

Figure 4.16 Contours of υ_t at plane (C)

Table 4.4 summarizes the maximum values of k, ϵ, and υ_t derived for each of the planes of measurement investigated. A rough estimation of turbulent length scale (0.013 m) and time scale (0.45 s) showed that the data measurement frequency and spatial resolution was sufficient for the purpose of this study.

Table 4.4 Maximum values of turbulent flow parameters derived for the investigated planes of measurement

Plane	k (m^2/s^2)	ϵ (m^2/s^3)	$\upsilon_t (m^2/s)$
(A)	0.70E-03	0.40E-03	1.50E-04
(B)	2.50E-03	1.00E-03	5.00E-04
(C)	3.00E-03	2.00E-03	4.00E-04
(D)	3.00E-03	3.00E-03	2.50E-04
(E)	2.50E-03	1.50E-03	2.50E-04
(F)	1.50E-03	1.00E-03	1.50E-04

The maximum values of ϵ varied from $4 \times 10^{-4}\ m^2/s^3$ at plane (A) to $3 \times 10^{-3}\ m^2/s^3$ at plane (D), located in the middle of the mixing zone. Turbulent flow characteristics such as k, ϵ, and υ_t typically reached their highest magnitude in the central region of the mixing zone (located between planes (B) and (D)). This is the same region in which the centers of the two vortices occurred (Figure 4.10), and where the flow is highly turbulent. The range of non-dimensional turbulent eddy viscosity ($\upsilon_t/(u_0 W)$) reported by Coletti et al. (2013) for an inclined jets in crossflows changes from 0 to 0.03. In this study, $\upsilon_t/(u_0 W)$ ranges between 0 and 0.09 in the measurement planes.

4.6 Conclusions

The present study attempted to investigate the flow characteristics of turbulent mixing regimes of surface buoyant jets in crossflow conditions. To the best knowledge of the authors, it is the first time Stereo-PIV measurement was used to study the mixing and flow structure of the surface jets in crossflows. The novelty of this study is that mean and turbulent flow characteristics of the jets were extracted in the mixing zone, which is useful for the study and design of the jet dispersion systems. For this purpose, Stereo-PIV measurements were conducted at several planes downstream of the discharge point. Measurements were conducted at six longitudinal ($x - z$) planes, perpendicular to the jet axis, downstream of the discharge point. The Stereo-PIV measurement planes covered a volume of water delineated by water depth of up to $9.8W$ and a width of up to $39W$ (see Table 4.2 for more details). Using the Stereo-PIV technique in this field made it possible to detect two types of circulations observed in the flow structure which were not previously mentioned in the literature related to the surface jets in crossflows. Also, the turbulent flow characteristics (such as the turbulent kinetic energy dissipation rate and turbulent stresses) extracted directly from the Stereo-PIV measurements could be of interest for the computational fluid dynamics community as it can help improve the numerical modelling of the surface jets in crossflows, useful for the study of the jet dispersion systems.

A downstream-propagating vortex (see Figure 4.10b) was observed at the transverse planes in the flow structure, inside the mixing zone of surface jet. Mean velocity streamlines showed the existence of this vortex occurring up to a distance of $35W$ downstream of the discharge point. Additionally, mean excess velocity streamlines (see Figure 4.10a) showed a circulation in the middle of the mixing zone at the longitudinal planes. The isosurfaces of streamwise velocity showed a slow-moving flow zone in the regions closer to the water surface and higher streamwise velocity underneath the surface jet. The distribution of the normal stress terms showed that the dominant component of $\overline{\mathrm{k}}$ was $\overline{u_2'^2}$, which was one of the main velocity components of the vortex in transverse planes. This confirms that the structure of the turbulence is anisotropic in the y-direction compared to the x- and z- directions. The calculated values of ϵ from the measured Stereo-PIV data showed that the inclusion of the transversal component of the velocity ($\overline{u'_2}$) led to 1.5 times larger values for ϵ compared to the ones calculated from the in-plane components of the velocity. This demonstrates that that the local isotropy assumption is too conservative for the estimation of the terms $\overline{\left(\frac{\partial u_2'}{\partial x_1}\right)^2}$ and $\overline{\left(\frac{\partial u_2'}{\partial x_3}\right)^2}$ in this complex flow structure, where x_1 and x_3 are the streamwise and vertical length components. Center of the vortex in the transverse plane occurred between planes (B) and (D), in the middle of the mixing zone. As a result of the highly turbulent flow in the middle of the measurement zone, flow characteristics such as k, ϵ, and υ_t typically reached their highest values in this region. Considerable variations of normal shear stress, from a large negative value in the regions closer to the water surface to a high positive value deeper in the water, showed the existence of the span-wise vorticity in the flow mainly caused by Kelvin-Helmholtz instability.

5 Numerical Simulations of Surface Discharges into Crossflows[2]

Abstract

Three-dimensional (3-D) Computational Fluid Dynamics (CFD) models were developed in OpenFOAM for the surface discharge of buoyant jets into crossflows. Two different experimental cases were used for the validation of numerical results for temperature and velocity distributions and flow structures inside the mixing zone. Reynolds stress turbulence models and spatially filtered Large Eddy Simulation (LES) approach were used in the numerical models. Smagorinsky and Dynamic Smagorinsky approaches in the LES models were implemented. The effects of inclusion of free surface water in the CFD models on the performance of the numerical model results were investigated for one of the cases. A comparison of the numerical modelling results with the existing experimental works demonstrated the capability of the models to predict the behaviour of the surface jet discharging into crossflows.

5.1 Introduction

Mixing of discharging jets into water bodies is an important field of study for hydraulics scientists and engineers because of the complications in the physics of the mixing phenomenon. Surface discharges are designated as the most environmentally critical types of discharge as a result of the lower mixing capabilities. One of the main topics of interest in the literature on surface discharges is related to rivers reaching the lakes or oceans (Hetland, 2010). A more common solution to enhance the mixing of surface discharges is to release a jet into a flowing ambient stream. The interaction between the surface jet and the flowing receiving ambient water produces a sophisticated three-dimensional flow structure that creates various vortices and secondary currents in the flow structure.

---

[2] This technical article will be submitted to the *Journal of Environmental Fluid Mechanics* as a continuation of the previous study published in the same journal

In order to assess the environmental impacts of discharging jets, different predictive models have been developed and used. Generally, these models can be categorized into three different groups: length scale models (Chu and Goldberg, 1974; Knudsen, 1988; Wright, 1977), integral models (Cheung et al., 2000; Chu and Lee, 1996; Jirka, 2004, 2007; Wood, 1993) and hybrid models that use the combination of both length-scale and integral techniques (Davidson and Pun, 1998, 2000). Kim et al. (2002) used the jet integral-particle tracking hybrid model for single buoyant submerged jets. Different types of mixing scenarios can occur in the mixing of surface discharges. Arita et al. (1986) studied the classification and mixing of two-dimensional buoyant surface jets. Jones et al. (2007) introduced a comprehensive method of flow classification for positively buoyant jets. Abessi et al. (2011) recommended another flow classification for negatively buoyant surface discharges.

These predictive methods were used in some of the commercial models such as CorMix (Doneker, 1990), CorJet (Jirka, 2004) and VisJet (Cheung et al., 2000). The simplicity and accuracy of these models has led to widespread usage by consulting engineers in the field of mixing of jets in ambient water. However, the uses of these predictive tools are limited to simple problems. In the case of complex problems (complex geometry or hydrodynamic conditions) the results are not reliable. In these cases, it is necessary to perform computational fluid dynamics (CFD) simulations.

Most of the CFD simulations in the field of mixing are related to submerged jets in stationary ambient. Based on the ratio of jet density (ρ_0) to ambient water density (ρ_a), the physics of the jet is categorized as either negatively ($^{\rho_0}/_{\rho_a} > 1$) or positively ($^{\rho_0}/_{\rho_a} < 1$) buoyant. Horizontal positively buoyant submerged jets have been numerically investigated by scientists (Kheirkhah Gildeh et al., 2014; Kim et al., 2002; Van Maele and Merci, 2006). In addition, numerical studies of vertical negatively buoyant submerged jets in stagnant water have been conducted in the literature (Mier-Torrecilla et al., 2012; Yu-hong and Wen-xin, 2005). Recent numerical simulations focus on the mixing characteristics of inclined negatively buoyant submerged jets (Gildeh et al., 2015; Kheirkhah Gildeh et al., 2015; Oliver et al., 2008; Palomar et al., 2012; Vafeiadou et al., 2005; Zhang et al., 2016, 2017). Yan and Mohammadian (2017) investigated the performance of the buoyancy modified $k - \epsilon$ turbulence model in the mixing of a vertical buoyant jet subjected to lateral confinement. They introduced a new method that links the Prandtl number to the densimetric Froude number. Additionally, Pilechi et al. (2016; 2015) performed field measurements of transverse dispersions of desalination plant outfalls and wastewater effluent discharged into the surface of receiving water such as rivers and coastal waters.

McGuirk and Rodi (1978) developed a depth-averaged mathematical model to estimate the temperature and concentration distribution for the near field of the side discharges into crossflow in open channels. The model was able to predict two-dimensional flow characteristics such as size of the recirculation zone, jet trajectory, dilution and isotherms. They compared the results of the depth-averaged model with experimental measured data for a wide range of jet to crossflow velocity ratios. One of the first three-dimensional numerical simulations of surface buoyant jets in stagnant water was conducted by McGuirk and Rodi (1979). They used the finite difference method to solve the continuity, lateral and longitudinal momentum and thermal energy equations. They implemented the $k - \epsilon$ turbulence model to determine the turbulent shear stresses and fluxes. Kim and Chu (2006) used the commercially available CFD package FLOW-3D to numerically study the three-dimensional mixing characteristics of the surface and submerged buoyant flow discharging into crossflow in shallow and deep water. They assessed the applicability of the model to predict the jet trajectory, the dimensions of the recirculation zone and the isotherms.

The effect of crossflow on jet mixing is a complex three-dimensional phenomenon that has been studied by scientists for a long time, experimentally and numerically. The physics of jets in crossflow was extensively studied by scientists, numerically and experimentally, for vertical free submerged jets (Karagozian, 2014; Ruiz et al., 2015) and inclined submerged jets (Dai et al., 2016). Large Eddy Simulation (LES) has been widely used by scientists to study the mixing of submerged jets. LES models were recognized as an efficient tool for the assessment of jets in crossflow for compressible and incompressible flow (Denev et al., 2009; Esmaeili et al., 2015; Haven and Kurosaka, 1997; Jones and Wille, 1996; Kalita et al., 2002; Ma et al., 2007; Saha and Yaragani, 2012; Yuan et al., 1999). The numerical investigation of the three-dimensional LES model extracted the turbulent flow characteristics. The existence of the counter-rotating vortex pair (CVP), the horseshoe-vortex (HSV), the wake vortices (WV), the upright-vortices (UV) and the ring-like vortices (RLV) was investigated numerically for different jet-to-crossflow velocity ratios (R) and different Reynolds numbers. Peng and Davidson (2001) used the LES approach with dynamic Smagorinsky sub-grid scale (SGS) model to study the mixing of positively buoyant jets. Zhang et al. (2016) used the same approach for negatively buoyant submerged jets and compared the results with the SGS model and $k - \epsilon$ turbulence model as well as the experimental works.

The main difference with vertical submerged jets in the case of surface discharges is the existence of the water surface, which leads to the elimination of one of the CVP in the typical known flow structure of the vertical submerged jet in crossflow cases. This change in the structure was reported in experimental studies by Gharavi et al. (2020).

The numerical study of surface discharges has not been investigated extensively, and it is necessary to assess the numerical model's capabilities and different modelling approaches. In recent years, Khosravi and Javan (2020, 2022) numerically investigated the lateral thermal plume flow structures by modelling the experimental research conducted by Abdelwahed (1981). They used the *buoyantBoussinesqPimpleFoam* solver with realizable $k - \epsilon$ turbulence model in OpenFOAM. They also showed the effectiveness of using dynamic adaptive mesh refinement in OpenFOAM on the computational time and modelling results. They compared the numerical results with the experimental works conducted by Abdelwahed (1981) and concluded that the modelling approach is capable of predicting the experimental measured results of recirculation zone size, time-averaged excess temperature, half-width and half-thickness of the maximum time-averaged excess temperature, and jet trajectory along the mixing zone. Their modelling results were in good agreement with reported experimental data. Numerical simulations help extract the results for the entire field and evaluate the phenomenon accurately. Validations are necessary to ensure the results are valid and compatible with experimental studies.

In this study, numerical modelling work for two different cases (associated with a surface buoyant jet discharging into crossflow) were used to validate the numerical simulations. The first case (Case 1) was related to experimental measurements of the flow parameters conducted by Anwar (1987). It involved a warm water jet discharged from a rectangular open channel perpendicular to a crossflow in ambient water. The rectangular channel was projected $0.30\,m$ into the flume with upstream and downstream transition walls. The second case (Case 2) was the experimental study of a surface buoyant jet discharging into a crossflow ambient conducted by Gharavi et al. (2020). The warm water jet discharged normal to a crossflow ambient through a square shaped nozzle in such a way that the top of the nozzle was right at the water surface. The nozzle was projected 0.10

m into the flume and moved with a constant velocity along the flume to represent the crossflow ambient.

5.2 Computational Methodology

5.2.1 RANS Models

As the focus of this research is on the mixing of jets, which mainly represent outfalls, the main governing equations for the CFD modelling of buoyant surface jets are Navier-Stokes Equations for incompressible Newtonian fluids. The Reynolds Average Navier-Stokes (RANS) equations after time-averaging are described in Einsteinian notation as follows (Pope, 2001):

$$\frac{\partial \overline{u_i}}{\partial x_i} = 0 \tag{5.1}$$

$$\rho \frac{\partial \overline{u_i}}{\partial t} + \rho \frac{\partial \left(\overline{u_i}\,\overline{u_j}\right)}{\partial x_j} = -\frac{\partial p}{\partial x_i} + \frac{\partial}{\partial x_j}\left[\mu \left(\frac{\partial \overline{u_i}}{\partial x_j}\right) + \tau_{ij}^R\right] + \rho g_i \tag{5.2}$$

$$\rho \frac{\partial \overline{\phi}}{\partial t} + \rho \frac{\partial \left(\overline{\phi}\,\overline{u_i}\right)}{\partial x_i} = \frac{\partial}{\partial x_i}\left(\Gamma \frac{\partial \overline{\phi}}{\partial x_i}\right) + \frac{\partial Q_i}{\partial x_i} \tag{5.3}$$

where x_i represents the coordinates in a Cartesian frame, u is velocity, p is the pressure, ρ is the fluid density, t is time, μ is the fluid viscosity, ϕ is the scalar concentration, Γ is molecular diffusivity, g is gravitational acceleration and the overbar designates time-average variables. $\tau_{ij}^R = -\rho\overline{u_i' u_j'}$ are Reynolds stresses and $Q_i = -\rho\overline{\phi' u_i'}$ are turbulent scalar fluxes. The tensor index notation ($\overline{u_i' u_j'}$) includes six unknowns. To estimate these terms, LRR turbulence model is used.

The Launder-Reece-Rodi (LRR) turbulence model was used in the numerical modelling of Case 1. The LRR turbulence model is a Reynolds Stress Turbulence Model (RSTM). In this method, there is a main transport equation for Reynolds stress derived from subtracting the averaged momentum equation from the instantaneous one as:

$$\frac{D\overline{u_i u_j}}{Dt} = \frac{\partial \overline{u_i' u_j'}}{\partial t} + \overline{u}_k \frac{\partial \overline{u_i' u_j'}}{\partial x_k} = D_{ij}^{\nu} + D_{ij}^{T} + \phi_{ij} + P_{ij} + \epsilon_{ij} \tag{5.4}$$

where P_{ij} is the production term, D_{ij} is the diffusion term, ϕ_{ij} is the pressure strain rate correlation term, and ϵ_{ij} is the turbulent dissipation rate term. For more information about LRR turbulence model reader is referred to Launder et al. (1975).

5.2.2 Large Eddy Simulation (LES)

In addition to the mentioned method, the LES approach is also considered in the CFD modelling in this study. In the LES approach, eddies are filtered by the local grid size into large and small sizes. In order to calculate the larger eddies, instantaneous Navier-Stokes equations are solved. Smaller eddies on the other hand are handled by using turbulent model techniques in RANS equations. The filtered continuity, momentum conservation and advection-diffusion equations are described as follows:

$$\frac{\partial \widetilde{u_i}}{\partial x_i} = 0 \tag{5.5}$$

$$\rho\frac{\partial \widetilde{u_i}}{\partial t} + \rho\frac{\partial\left(\widetilde{u_i}\,\widetilde{u_j}\right)}{\partial x_j} = -\frac{\partial p}{\partial x_i} + \frac{\partial}{\partial x_j}\left[\mu\left(\frac{\partial \widetilde{u_i}}{\partial x_j}\right) + \tau_{ij}^{SGS}\right] + \rho g_i \tag{5.6}$$

$$\rho\frac{\partial \tilde{\phi}}{\partial t} + \rho\frac{\partial\left(\tilde{\phi}\widetilde{u_i}\right)}{\partial x_i} = \frac{\partial}{\partial x_i}\left(\Gamma\frac{\partial \tilde{\phi}}{\partial x_i}\right) + \frac{\partial Q_i}{\partial x_i} \tag{5.7}$$

where the tilde indicates spatially filtered variables $\tau_{ij}^{SGS} = \rho\widetilde{u_i}\widetilde{u_j} - \rho\widetilde{u_i u_j}$ are Smagorinsky sub-grid scale (SGS) Reynolds stresses and $Q_i = \rho\tilde{\phi}\widetilde{u_j} - \rho\,\widetilde{\phi u_i}$ are SGS scalar fluxes.

The Smagorinsky SGS model is one of the most popular approaches to estimate τ_{ij}^{SGS} (Dejoan and Leschziner, 2005; Zhiyin, 2015). The SGS stress tensor and turbulent concentration flux for incompressible flows (Erlebacher et al., 1992) are modelled by:

$$\tau_{ij}^{SGS} = 2\mu_t^{SGS}\,\widetilde{S_{ij}} \tag{5.8}$$

$$Q_i = \frac{\mu_t^{SGS}}{Pr_t^{SGS}}\frac{\partial \tilde{\phi}}{\partial x_i} \tag{5.9}$$

where μ_t^{SGS} is SGS eddy viscosity, $\widetilde{S_{ij}} = \frac{1}{2}\left(\frac{\partial \widetilde{u_i}}{\partial x_j} + \frac{\partial \widetilde{u_j}}{\partial x_i}\right)$ is the filtered or resolved scale strain rate tensor and Pr_t^{SGS} is the SGS Prandtl number (or Schmidt number) and is considered to be 0.7 (Law, 2006; Yimer et al., 2002). The unsolved SGS eddy viscosity, μ_t^{SGS}, can be stated in the Smagorinsky method (Smagorinsky, 1963) as:

$$\mu_t^{SGS} = \rho \, (C_s \Delta)^2 \, |\tilde{S}| \tag{5.10}$$

$$|\tilde{S}| = \sqrt{2 \, \widetilde{S_{ij}} \, \widetilde{S_{ij}}} \tag{5.11}$$

where $\Delta = (\Delta x_1 \, \Delta x_2 \, \Delta x_3)^{1/3}$ is the LES filter width and C_s is the Smagorinsky constant, which can be chosen between 0.1 and 0.24. The C_s value could be considered as a constant value in the model; however, to better estimate μ_t^{SGS}, a localized dynamic approach was considered, known as the "Dynamic Smagorinsky" SGS model proposed by Germano et al. (1991). Lilly (1992) suggested a least square method to minimize the error to improve the evaluation of C_s as:

$${C_s}^2 = \frac{\langle L_{ij} M_{ij} \rangle}{2 \, \langle M_{ij} M_{ij} \rangle} \tag{5.12}$$

$$L_{ij} = \widehat{\tilde{u}_i \tilde{u}_j} - \hat{\tilde{u}}_i \hat{\tilde{u}}_j \tag{5.13}$$

$$M_{ij} = \Delta^2 \widehat{|\tilde{S}| \, \widetilde{S_{ij}}} - \tilde{\Delta}^2 \, |\hat{\tilde{S}}| \, \hat{\tilde{S}}_{ij} \tag{5.14}$$

where $\langle \, \rangle$ indicates a spatial averaging over directions of statistical homogeneity and indicates a spatial filtered quantity on the test-filter. The Pr_t^{SGS} shall be adjusted as:

$$Pr_t^{SGS} = \frac{{C_s}^2}{{C_\phi}^2} \tag{5.15}$$

$${C_\phi}^2 = \frac{\langle \epsilon_i R_i \rangle}{\langle R_i R_i \rangle} \tag{5.16}$$

$$\epsilon_i = \widehat{\tilde{\phi} \tilde{u}_i} - \hat{\tilde{\phi}} \hat{\tilde{u}}_i \tag{5.17}$$

$$R_i = \Delta^2 \widehat{|\tilde{S}| \frac{\partial \tilde{\phi}}{\partial x_i}} - \tilde{\Delta}^2 \, |\hat{\tilde{S}}| \frac{\partial \hat{\tilde{\phi}}}{\partial x_i} \tag{5.18}$$

In this study, two different approaches were implemented for modelling of a jet in crossflow. For Case 1, a rigid water surface was considered in the model to represent the interaction between the water and atmosphere. This approach was mostly used in the modelling works for submerged jets (Zhang et al., 2017; Zhao et al., 2021) and recently implemented by Khosravi and Javan (2020, 2022) for the surface discharges into crossflow. For Case 2, a free surface was considered for the first time in the simulation of surface buoyant jets in crossflow. More details are provided later in this study.

5.2.3 Length Scales and Non-Dimensional Parameters

Important length scale parameters in the mixing of a surface jet discharging into crossflow has been widely used for the classification of surface discharges into crossflows (Abessi et al., 2011; Jones et al., 2007). The relevant non-dimensional parameters in this study are introduced in Table 5.1 and shown in Figure 5.1.

Table 5.1 Dynamic length scales and non-dimensional parameters

Type of scale	Length scale
Discharge length scale	$L_Q = Q_0 / M_0^{1/2}$
Jet-to-plume length scale	$L_M = M_0^{3/4} / J_0^{1/2}$
Jet-to-crossflow length scale	$L_m = M_0^{1/2} / \overline{u_a}$
Plume-to-crossflow length scale	$L_b = J_0 / \overline{u_a}^3$
Velocity Ratio	$R = \overline{u_0} / \overline{u_a}$
Densimetric Froude Number	$Fr_0' = \dfrac{\overline{u_0}}{\left(g_0' \, a_0^{1/2}\right)^{1/2}} = \dfrac{L_M}{L_Q}$

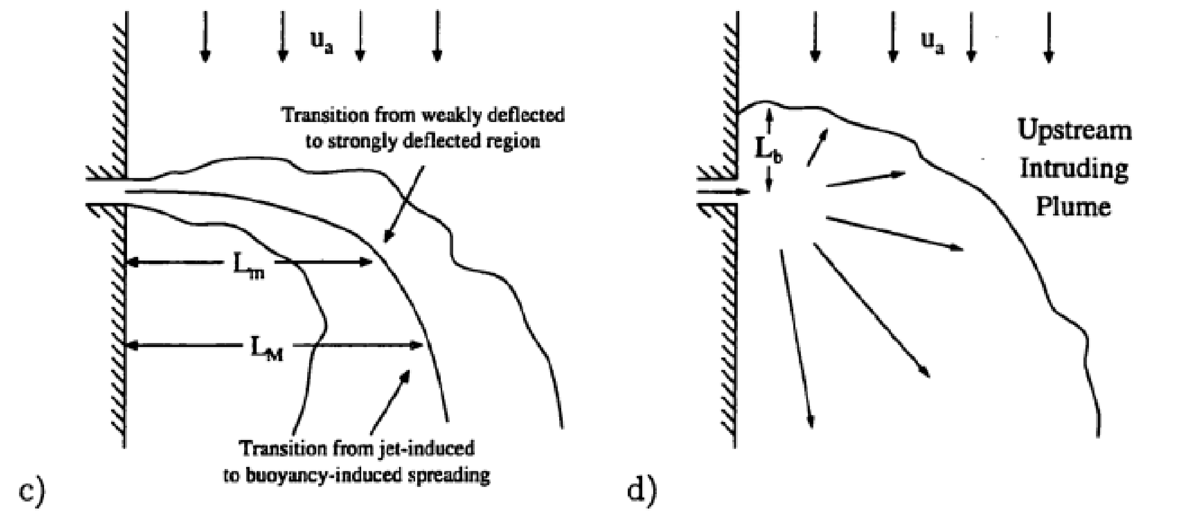

Figure 5.1 Important length scales in the mixing of surface discharges into crossflow

The temperature dilution factor is calculated as follows:

$$S_T = \frac{T - T_a}{T_0 - T_a} \tag{5.19}$$

where T is the mean temperature value at each point, subscripts a and 0 represent the receiving ambient water and discharged jet, respectively.

Finite volume method was used to solve the equations in the open-source software named OpenFOAM. Simulations were performed by modifying the pisoFoam and interFoam solvers. The modified version of the PisoFoam solver was first introduced by Gildeh et al. (2015) for incompressible flows. The equations of state (Millero and Poisson, 1981) and the Boussinesq term in the momentum equations were added to these solvers.

5.3 Experimental Study Case 1

Case 1 of the modelling works in this study is related to the experimental works conducted by Anwar (1987). Flow characteristics of the buoyant jet and crossflow are listed in Table 5.2. A warm surface jet with a temperature (T_0) of 73° C and average velocity ($\overline{u_0}$) of 0.26 m/s was discharged into a crossflow with a temperature (T_a) of 15° C and average velocity ($\overline{u_a}$) of 0.29 m/s.

Table 5.2 Flow characteristics of experimental study Case 1 (Anwar, 1987)

				Dimensions		
		Velocity (m/s)	Temperature (°C)	Width (m)	Length (m)	Height (m)
Case 1	Jet	0.26	73	0.25	3.8	0.153
	Crossflow	0.29	15	3.66	40	0.320

A surface jet with the height (h_0) of 0.153 m is almost half of the depth of crossflow ambient (h_a). The Reynolds number (Re) of the turbulent buoyant jet is 11×10^4 and the crossflow is 7.4×10^4 with a densimetric Froud number (Fr_0') of 1.7 and velocity ratio (R) of 0.9.

5.3.1 Model Domain and Boundary Conditions

The 3-D schematic view of the modelling geometry for Case 1 is shown in Figure 5.2. The surface buoyant jet, crossflow and outlet flow directions are shown in Figure 5.2 by red arrows.

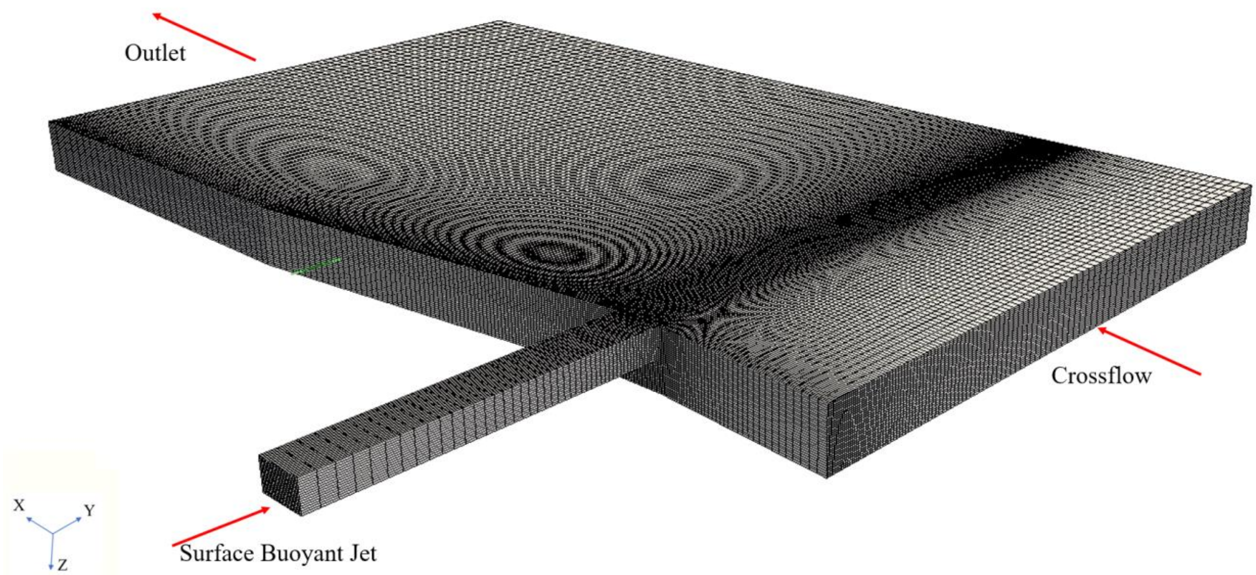

Figure 5.2 Schematic view of jet in crossflow

The geometry for Case 1 included 706,000 cells. Mesh sizes are shown in Figure 5.3. The smallest cell size was 10 × 8 × 9 mm (point A) and the largest mesh size was the one farthest from the jet inlet with the dimensions of 125 × 87 × 10 mm (point B). The aspect ratio of the cells varied from 1.11 to 12.5 with the minimum value existing in front of the jet close to the location of three-dimensional flows and maximum value near the outlet of the flume (point C). The discharge channel was 1.8 m long and projected 0.3 m into the flume. A uniform fixed value boundary condition was chosen for the crossflow and surface buoyant jet. The boundary condition for the water surface was set to the symmetry plane and Zero gradient for the outlet. Additionally, initial values for parameters such as density, temperature and velocity were the same as experimental conditions (Figure 5.4). LES dynamic Smagorinsky method was implemented for Case 1.

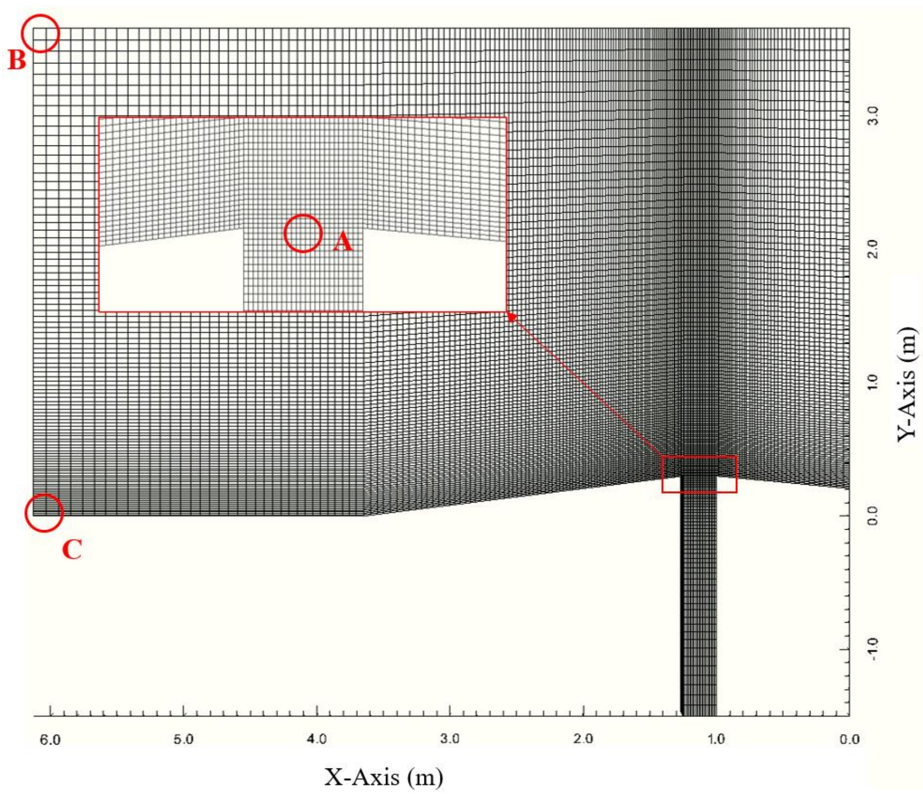

Figure 5.3 Mesh details for geometry of Case 1

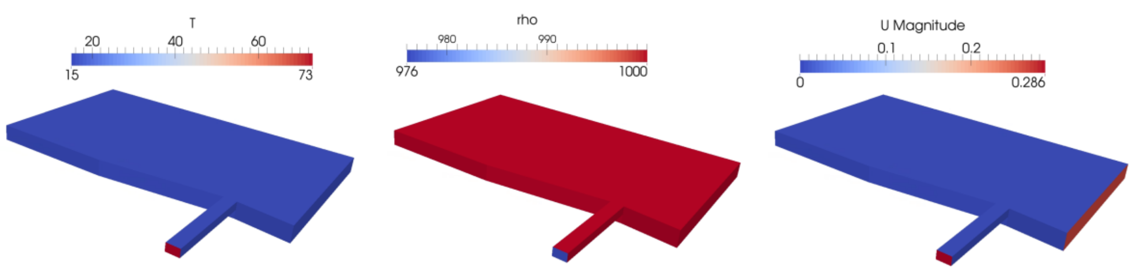

Figure 5.4 Initial conditions in the model for temperature, density and velocity

5.3.2 Results and Discussions

Mean temperature (T) isotherms on different horizontal (X-Y) planes in the flume were extracted from the numerical simulation results. These planes were chosen in a similar location to compare the results with the experimental data introduced by Anwar (1987), shown in Figure 5.5. Anwar measured the temperature in the mixing zone every 0.25 s for 150 s with the temperature resolution of 0.1° C. The red line in Figure 5.5 represents the experimental assessment of the jet centerline in the mixing zone introduced by Anwar (1987). The red line was determined by connecting the locations of the peak of the T isotherms on the plan view at several depths in the flume. The LES numerical results were able to predict the general trend and alignment of the jet axis in the plan view shown by the solid white arrow in Figure 5.5. The maximum distance of the predicted location of the jet axis in the numerical results was almost 0.25 m away from the experimental data closer to the surface ($\Delta Z = 0.02\ m$). Δ is the distance from the discharge point located on the water surface in the middle of the jet. In the deeper sections, jet axis prediction was closer to the experimental results. The LES numerical results replicated the secondary jet axis shown by the dashed white arrow between the main jet centerline and the inner wall of the flume, similar to the observations introduced by Anwar (1987). Here, jet axis is defined as a line created by connecting the locus of maximum concentration.

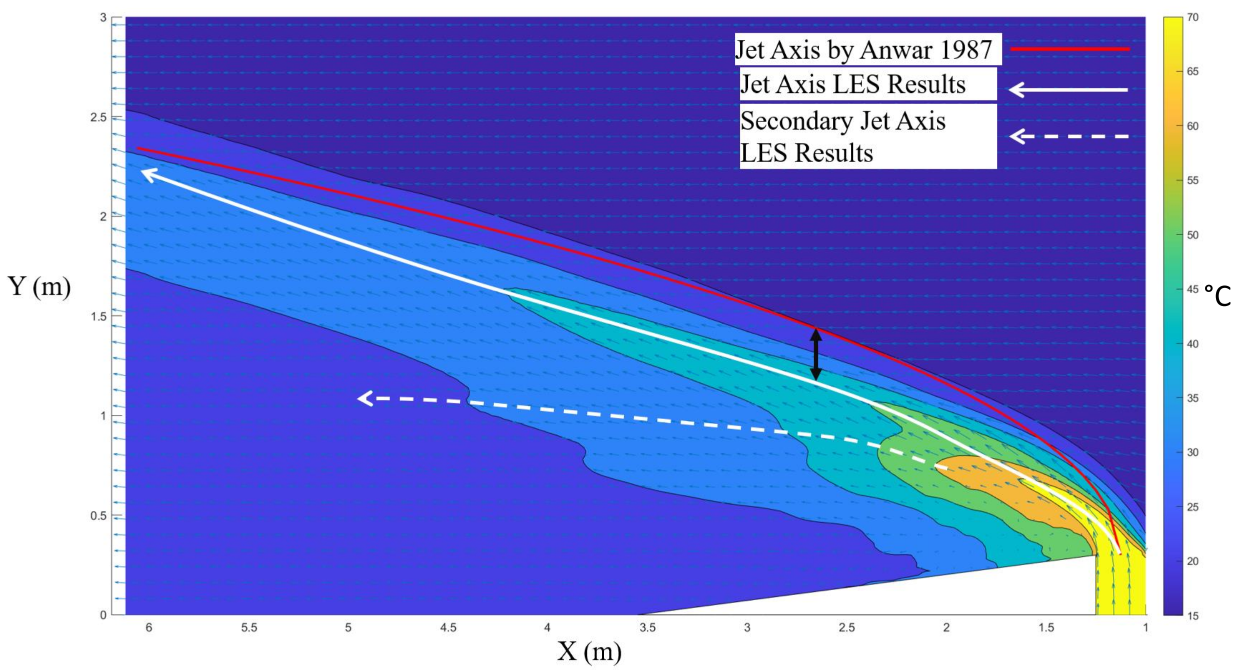

(a)

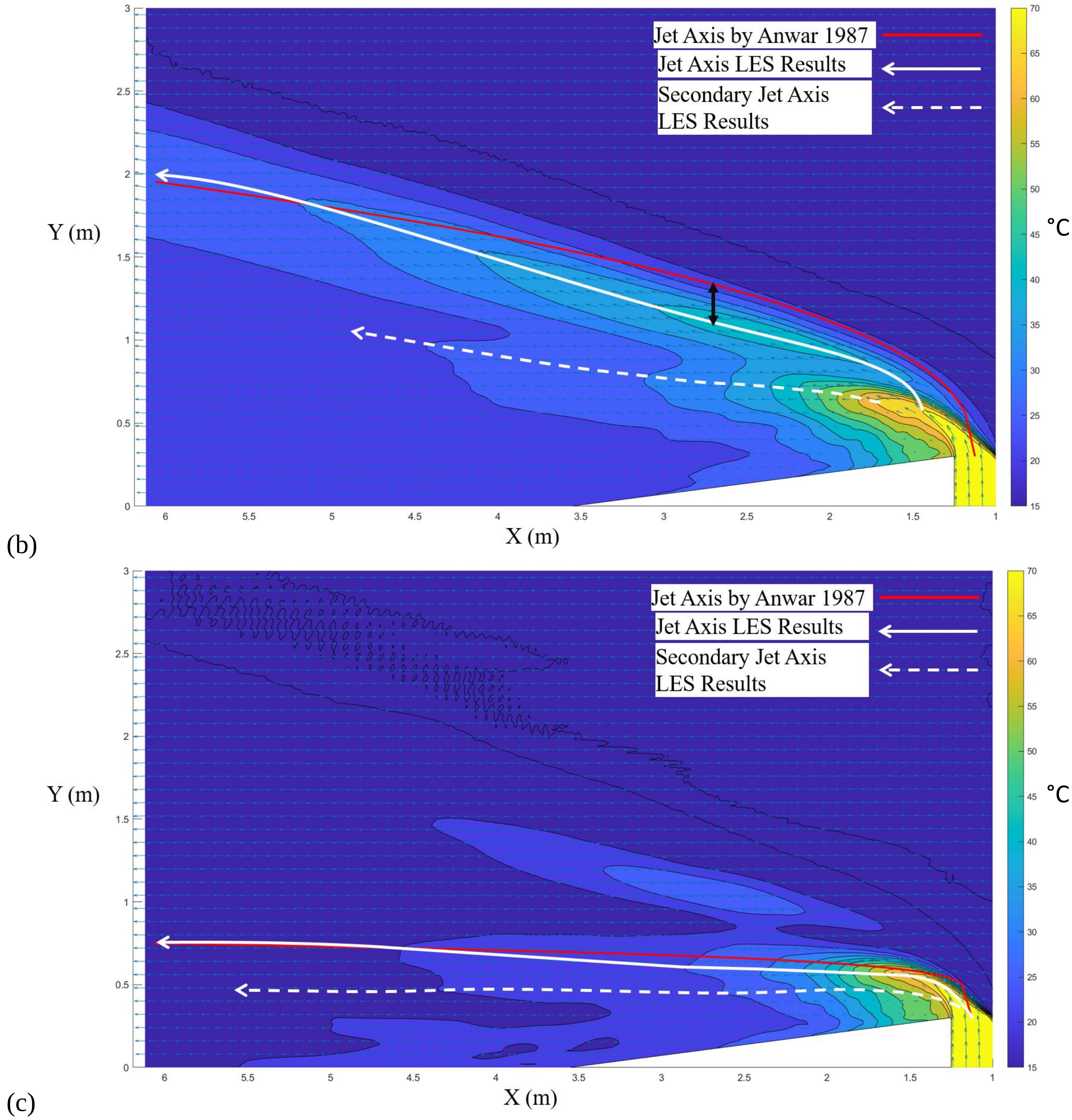

Figure 5.5 Mean temperature contours from LES results at depths (a) $\Delta Z = 0.02\ m$; (b) $\Delta Z = 0.05\ m$ and (c) $\Delta Z = 0.10\ m$

T isotherms were extracted on several vertical X-Z sections to show the development of the jet in the crossflow. Figure 5.6(a) to (c) present the T isotherms on the surface jet centerline and two sections 0.5 m and 2.0 m downstream of the discharge point in the flume. As the jet entered the crossflow, the maximum temperature gradient was in the vertical direction because of the buoyancy of the flow as shown in Figure 5.6(a).

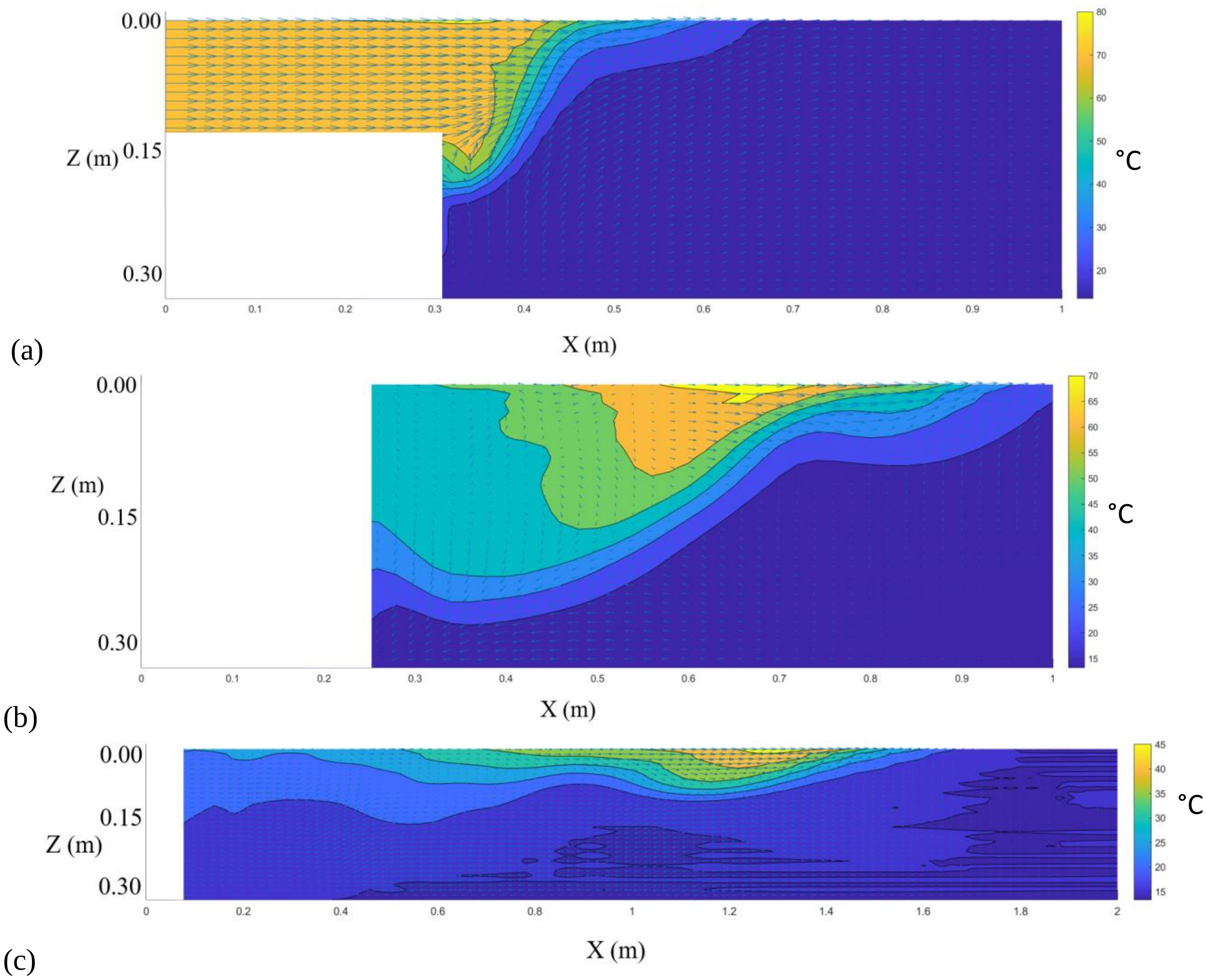

Figure 5.6 Mean temperature contours from LES results on the vertical sections along the flume at (a) $\Delta x = 0\ m$; (b) $\Delta x = 0.5\ m$ and (c) $\Delta x = 2.0\ m$

The minimum development of the jet in the crossflow was shown by the T isotherms in Figure 5.6(a). Although the jet momentum in the Y direction reached a maximum at the discharge point, jet and crossflow interaction prevented the jet progress in the Y direction and rapidly bent the jet towards downstream. The general trend of T isotherms showed that the surface jet stretched much further in the crossflow closer to the surface with shallower affected depth. The flow structure in the mixing zone was heavily affected by the interaction of the jet and crossflow. This interaction acted similar to a barrier in the crossflow, right in front of the discharge point.

A plan view of the mean velocity component in the X direction (Ux) is shown in Figure 5.7. As stated in Table 5.2, the velocities of the surface jet and crossflow were less than 0.29 *m/s*. Surface jet and crossflow interaction produced greater Ux values (0.35 m/s) at the jet centerline. Ux values increased to 0.40 m/s deeper in the crossflow as shown in Figure 5.7(c). Negative values of Ux in Figure 5.7 indicated the return flow towards upstream. This observation was reported in the experimental study of Anwar (1987) and LES results successfully captured this phenomenon. Similar to maximum Ux values, the return flow values were also increased from 0.05 to 0.10 m/s deeper in the flume. This observation is in agreement with the experimental velocity measurements conducted by Gharavi et al. (2020).

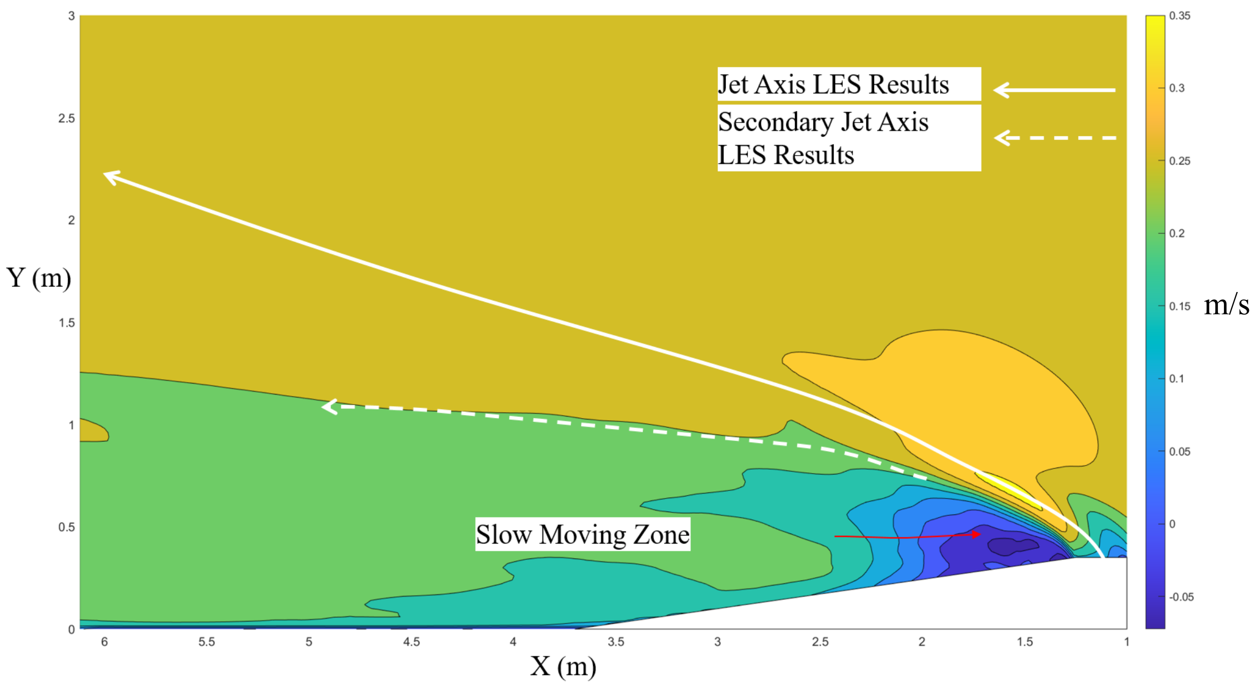

(a)

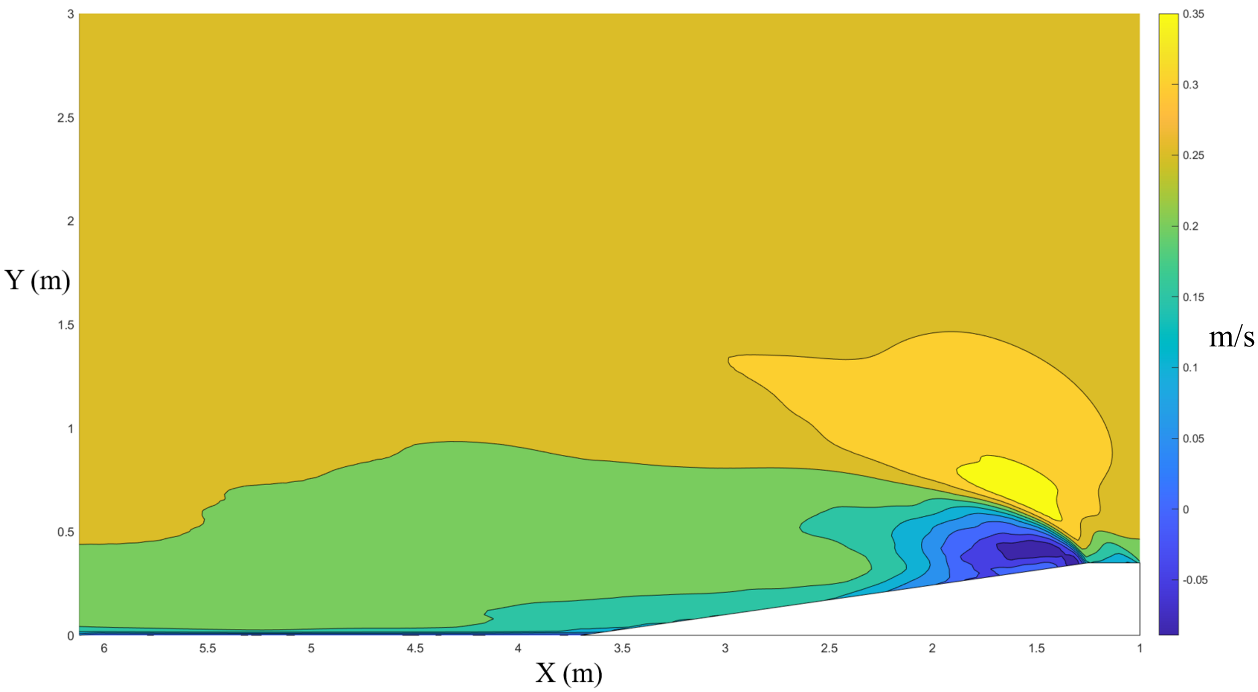

(b)

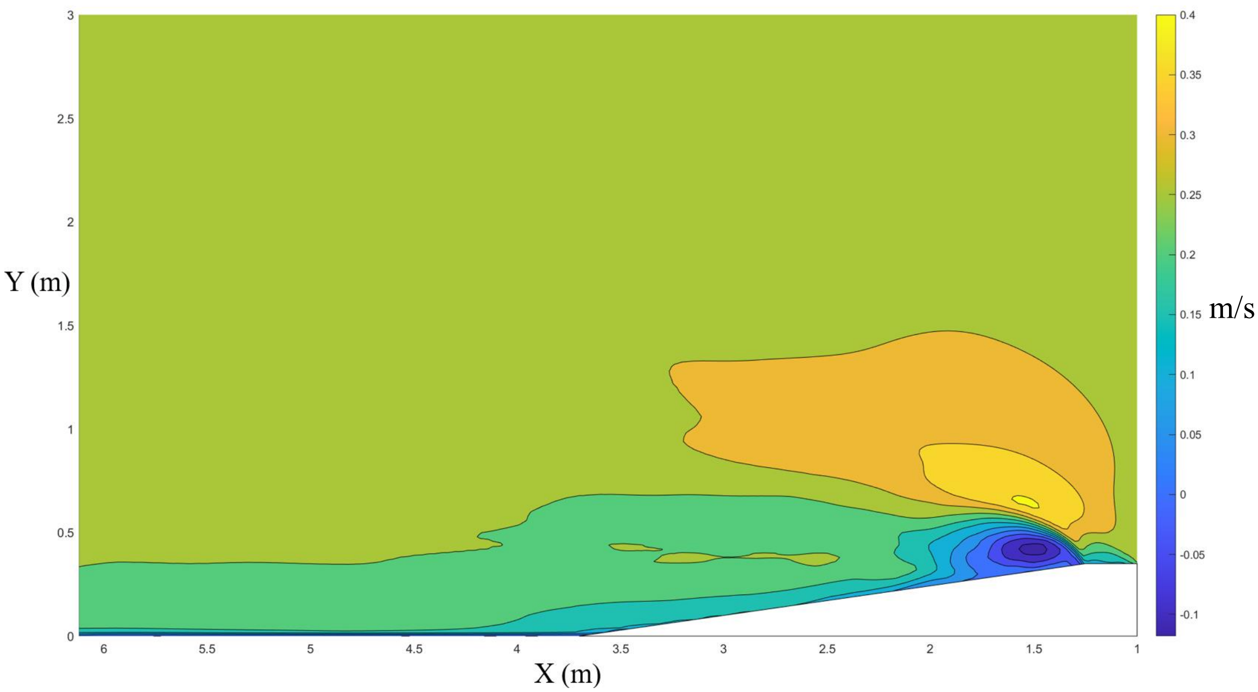

(c)

Figure 5.7 Plan view of the Ux distribution at depth (a) $\Delta Z = 0.02\ m$; (b) $\Delta Z = 0.05\ m$ and (c) $\Delta Z = 0.10\ m$

A plan view of the mean velocity component in the X direction (Ux) is shown in Figure 5.7. As stated in Table 5.1, the velocities of the surface jet and crossflow were less than 0.29 m/s. Surface jet and crossflow interaction produced greater Ux values (0.35 m/s) at the jet centerline. Ux values increased to 0.40 m/s deeper in the crossflow as shown in Figure 5.7(c).

Discharging of the strong jet with a high Reynolds number in the crossflow created a slow-moving zone downstream of the jet discharge point and between of the jet centerline and the inner wall. This zone is shown in Figure 5.7 (with crossflow velocity less than 0.29 m/s). The slow-moving zone created a wake type region between the jet axis and the inner wall of the flume. The wake type region included the secondary jet axis and decreases in water depth. The temperature gradient was much higher at the outer edge of the jet axis because crossflow-jet interaction causes rapid mixing at the interface.

In addition to the circulations inside the horizontal X-Y planes, in the slow-moving zone, vertical circulations of flow also existed in the numerical results. The mean velocity component in the Z direction (Uz) is shown in Figure 5.8. A negative and positive Uz explains the existence of this circulation. A similar observation was reported in the study by Gharavi et al. (2020).

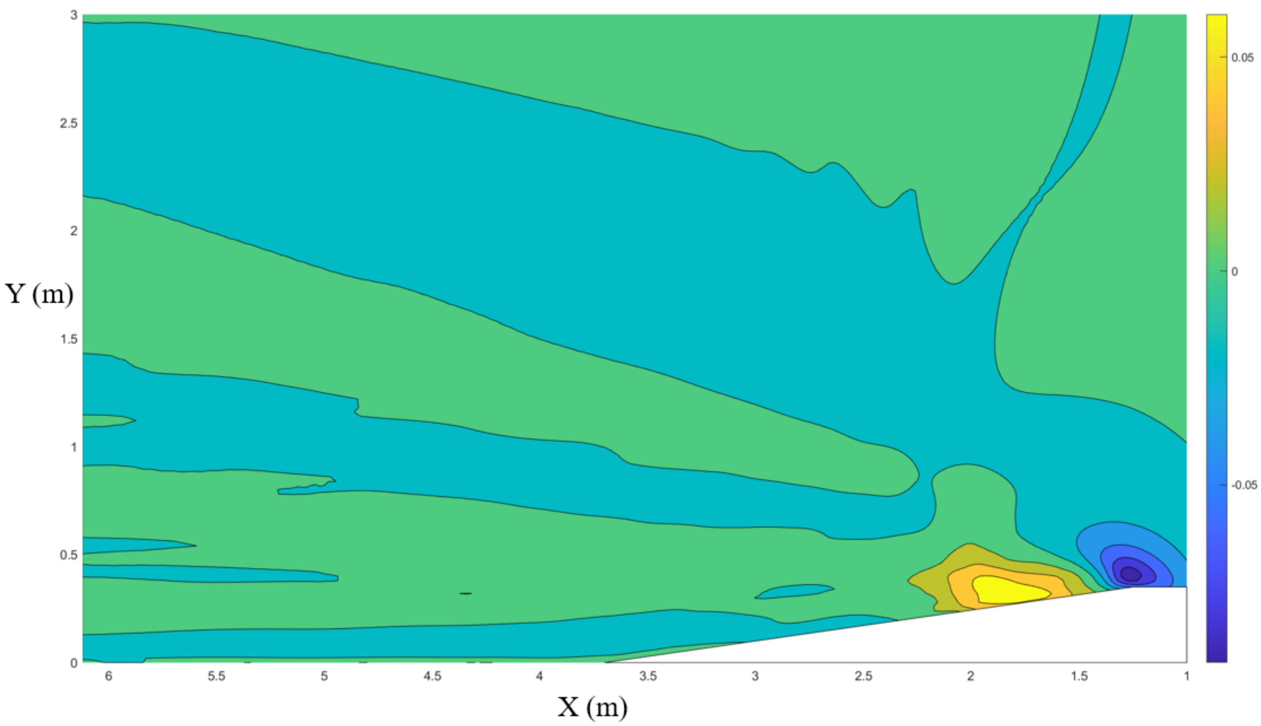

Figure 5.8 Plan view of the Uz distribution at $\Delta Z = 0.05\ m$;

LRR modelling results predicted the general trend in the flow structure and concentration distributions. Figure 5.9 shows the LRR modelling results compared with experimental data by Anwar (1987) and the white solid and dashed lines of LES modelling results.

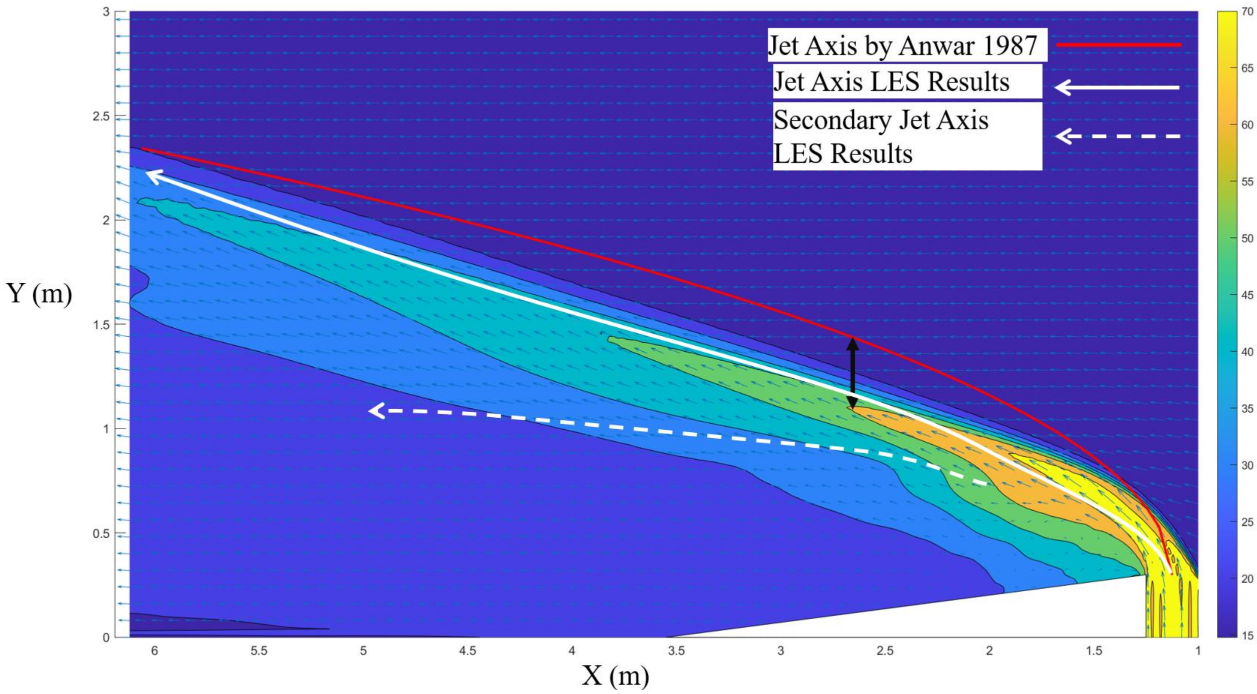

Figure 5.9 LRR simulation results for mean temperature contours at $\Delta Z = 0.02\ m$;

In addition to the LRR turbulent model, the $k - \epsilon$ turbulent model models were also considered in for Case 1. However, here the LRR turbulent model results are presented as they relatively performed well in the prediction on the jet axis.

5.4 Experimental Study Case 2

Case 2 of the modelling works in this study is related to the experimental works conducted by Gharavi et al. (2020). Flow characteristics of the buoyant jet and crossflow are listed in Table 5.3. A warm horizontal surface jet with a temperature (T_0) of 42.5° C and average velocity ($\overline{u_0}$) of 0.69 m/s was discharged into a crossflow with a temperature (T_a) of 22.4° C and average velocity ($\overline{u_a}$) of 0.11 m/s.

Table 5.3 Flow characteristics of experimental study Case 2 (Gharavi et al., 2020)

				Dimensions		
		Velocity (m/s)	Temperature (°C)	Width (m)	Length (m)	Height (m)
Case 2	Jet	0.69	42.5	0.008	0.1	0.008
	Crossflow	0.11	22.4	1.1	2.4	0.5

5.4.1 Model Domain and Boundary Conditions

The Smagorinsky LES approach was used for the modelling of Case 2. The crossflow water level was maintained at a constant elevation using a weir downstream of the flume. The location of the weir (shown in Figure 5.10) in the flume was chosen in a way that had no impact on the velocity distributions in the mixing zone of the surface jet discharging into the crossflow. The buoyancy modified *interFoam* solver was used for the modelling in OpenFOAM. The velocity boundary condition was set to *variableHeightFlowRateInletVelocity* upstream of the flume with a constant flow of 0.041 m^3/s in an iterative procedure to ensure the appropriate water elevation was obtained in the flume. The water level in the flume reached to the top of the nozzle. The buoyant surface jet boundary condition was set to uniform with a constant value of 0.69 m/s. A projected nozzle in the flume was modelled in the geometry to replicate the conditions in the laboratory.

The flume size in the modelling geometry was set to 0.9 m wide, 0.4 m deep and 3.0 m long with 460,000 cells. The minimum cell size was 2.7×2.7×2.7 mm in the surface jet nozzle. Sensitivity analyses was performed for the size of the flume to ensure that the weir was far enough from the nozzle and would not affect the mixing zone. The simulation ran for 40 s of warmup time to ensure that the water level was stable in the flume and reached the top of the nozzle. All the data extracted and post-processed in this study was after this warmup time.

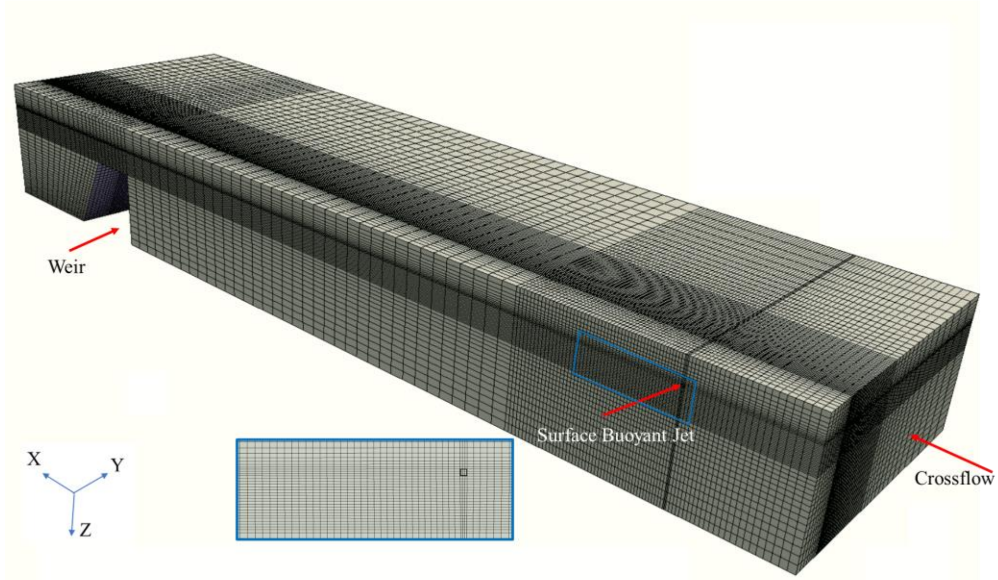

Figure 5.10 Schematic view of the jet in the crossflow

Mesh cell sizes were checked to ensure that the cell sizes were fine enough to capture turbulent flow characteristics. Resolved turbulent kinetic energy ($\bar{k}$) in the mixing zone were calculated using the oscillatory velocity components (u' in $u = U+u'$).

$$\bar{k} = {}^{1}\!/_{2}\left(\overline{{u'_x}^2} + \overline{{u'_y}^2} + \overline{{u'_z}^2}\right) \tag{5.20}$$

In Smagorinsky LES model, unresolved turbulent kinetic energy in Smagorinsky method were calculated using

$$k_{SGS} = \left(\frac{\mu_t^{SGS}}{\rho\,(C_s\Delta)}\right)^2 \tag{5.21}$$

In general, grid resolution used in LES method should be able to resolve more than 80% of total turbulent kinetic energy. Meaning the ratio of $\frac{\bar{k}}{k_{SGS}+\bar{k}}$ should be greater than 0.8. Calculations of this ratio indicated that in average 94% of the turbulent kinetic energy is resolved inside the mixing zone. Figure 5.11 shows the distribution of $\frac{\bar{k}}{k_{SGS}+\bar{k}}$ on Plane (C).

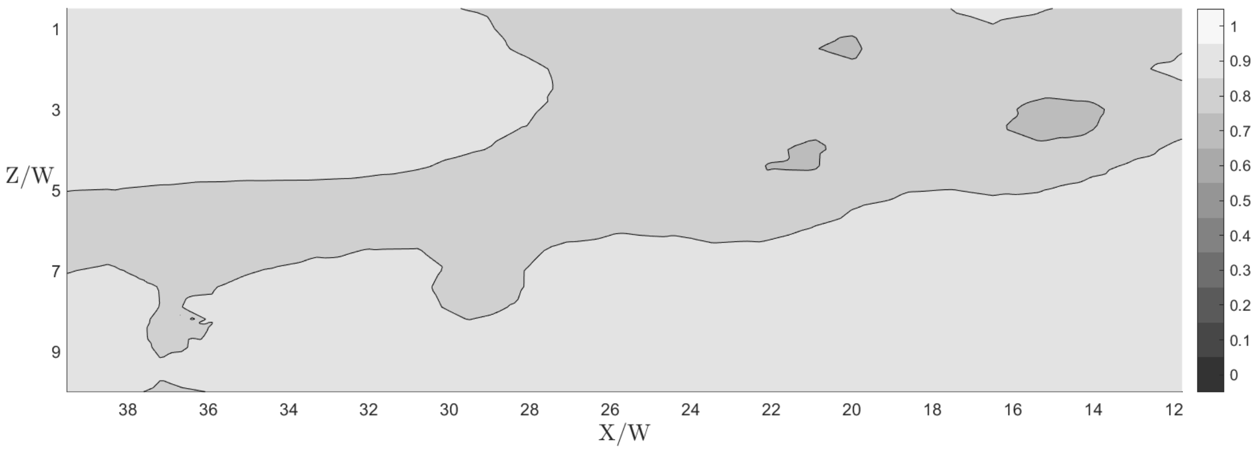

Figure 5.11 Mean temperature distributions in the mixing zone at Plane (C)

This is also aligned with the turbulent model length scale calculated from the experimental works done by Gharavi et al. (2020). Maximum values of k and ϵ was reported by Gharavi et al. (2020) as 3.00E-03 and 2.00E-03, respectively. Turbulent length scale (l) is calculated using

$$l = c_{\mu}^{3/4} \frac{k^{3/2}}{\epsilon} \qquad (5.22)$$

where $c_{\mu} = 0.09$ is a constant in the closure. l is calculated as 0.013 m here.

5.4.2 Results and Discussion

Mean temperature (T) distributions on X-Y planes are shown in Figure 5.12. These X-Z planes correspond to Planes (A) to (F) of Gharavi et al. (2020) introduced in their experimental study inside the mixing zone of a surface buoyant jet. Higher values of jet momentum closer to the nozzle exit point led to a lesser dilution in T. All the axes are non-dimensionalized by dividing by the width of the square shaped nozzle (W=0.008 mm). As shown in Figure 5.12(a), the maximum value of T is almost 31° C at Plane (A) and the area affected in ambient water T by the discharged jet is limited to a width of 7W and a depth of 3W. The affected area in Plane (B) stretches over the area with a width of 18W and a depth of 5W. Consequently, the temperature dilution factor S_T jumps to 0.71 on Plane (B) from 0.56 on Plane (A). Table 5.4 shows the values of S_T at different planes in the mixing zone.

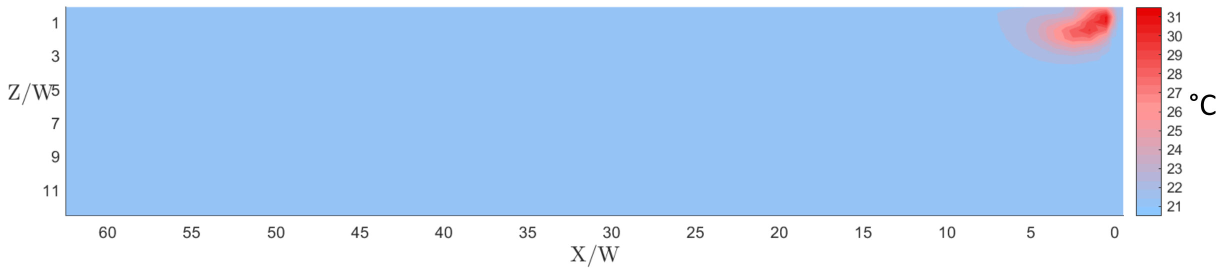
Z/W
1 3 5 7 9 11
X/W
60 55 50 45 40 35 30 25 20 15 10 5 0
31 30 29 28 27 26 25 24 23 22 21
°C

(a)

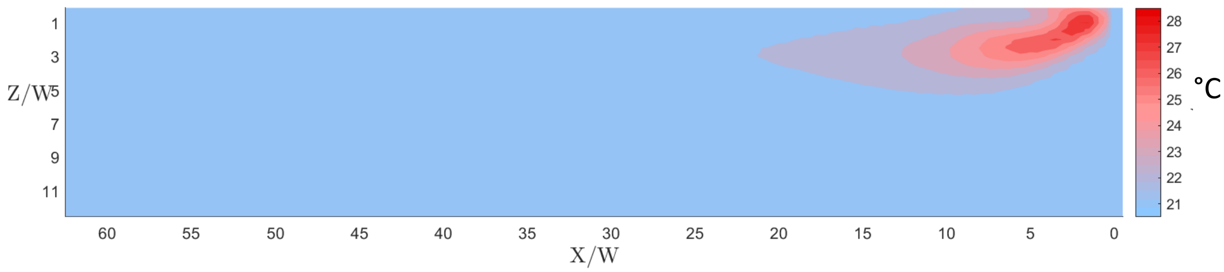
Z/W
1 3 5 7 9 11
X/W
60 55 50 45 40 35 30 25 20 15 10 5 0
28 27 26 25 24 23 22 21
°C

(b)

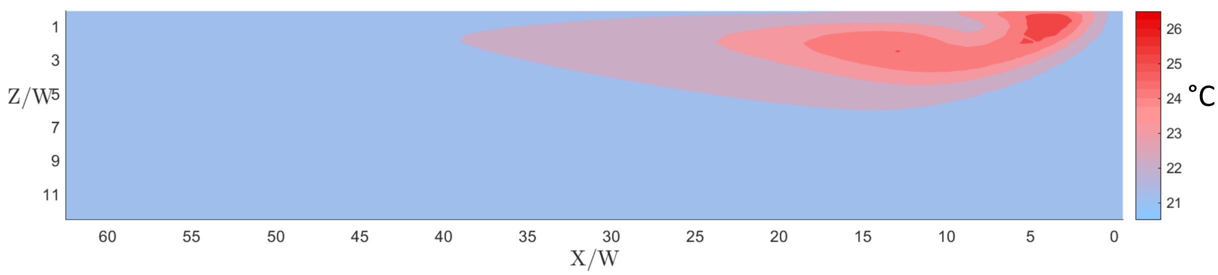
Z/W
1 3 5 7 9 11
X/W
60 55 50 45 40 35 30 25 20 15 10 5 0
26 25 24 23 22 21
°C

(c)

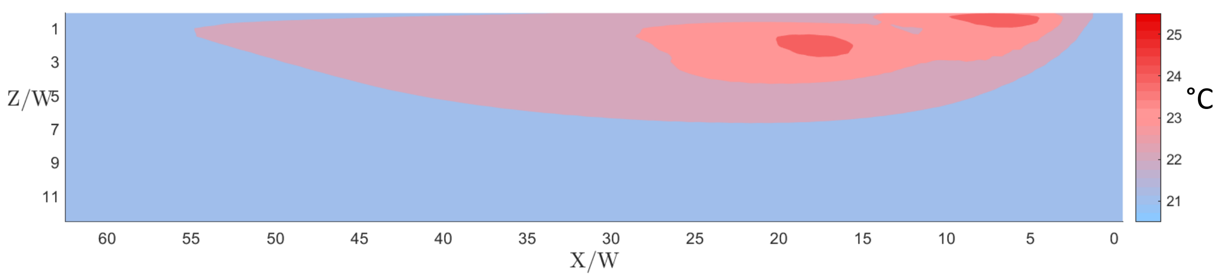
Z/W
1 3 5 7 9 11
X/W
60 55 50 45 40 35 30 25 20 15 10 5 0
25 24 23 22 21
°C

(d)

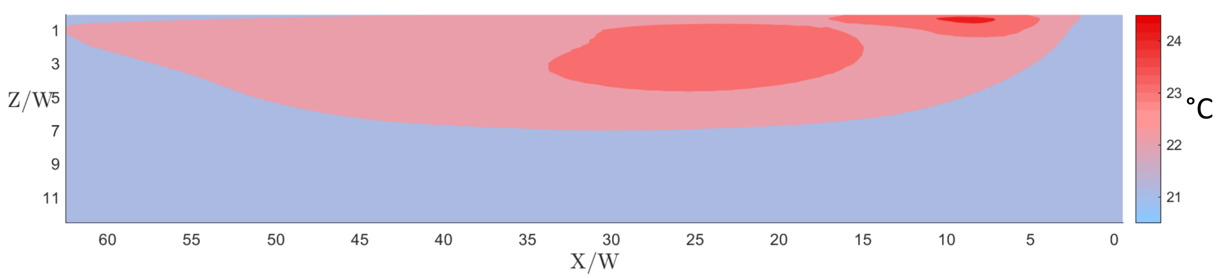
Z/W
1 3 5 7 9 11
X/W
60 55 50 45 40 35 30 25 20 15 10 5 0
24 23 22 21
°C

(e)

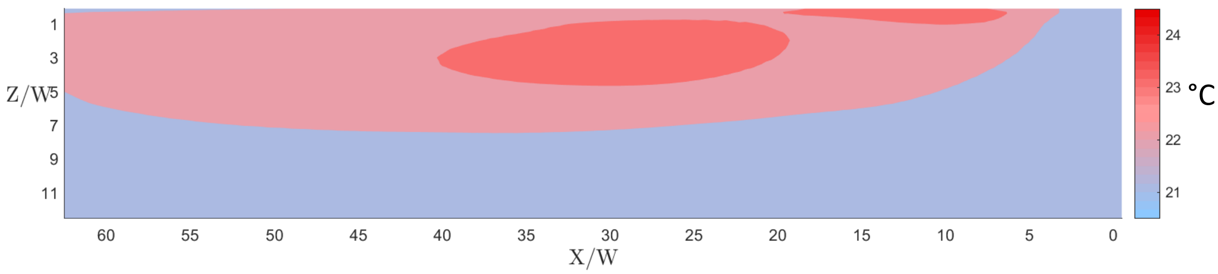

(f)

Figure 5.12 Mean temperature distributions in the mixing zone: (a) at Y/W = 7.8; (b) at Y/W = 11.1; (c) at Y/W = 14.3; (d) at Y/W = 17.3; (e) at Y/W = 19.1; and (f) at Y/W = 21.0

Table 5.4 Temperature dilution factor in the mixing zone

Plane	A	B	C	D	E	F
Y/W	7.8	11.1	14.3	17.3	19.1	21.0
S_T	0.56	0.71	0.81	0.86	0.91	0.91

A plan view of T distributions on X-Y planes are shown in Figure 5.13. The jet axis center lines in Figure 5.13 (a) and (b) are shown with a solid blue arrow. The secondary jet centerline within the slow-moving zone was also captured in the results, shown with a dashed blue arrow. Similar observations were reported in the study by Anwar (1987).

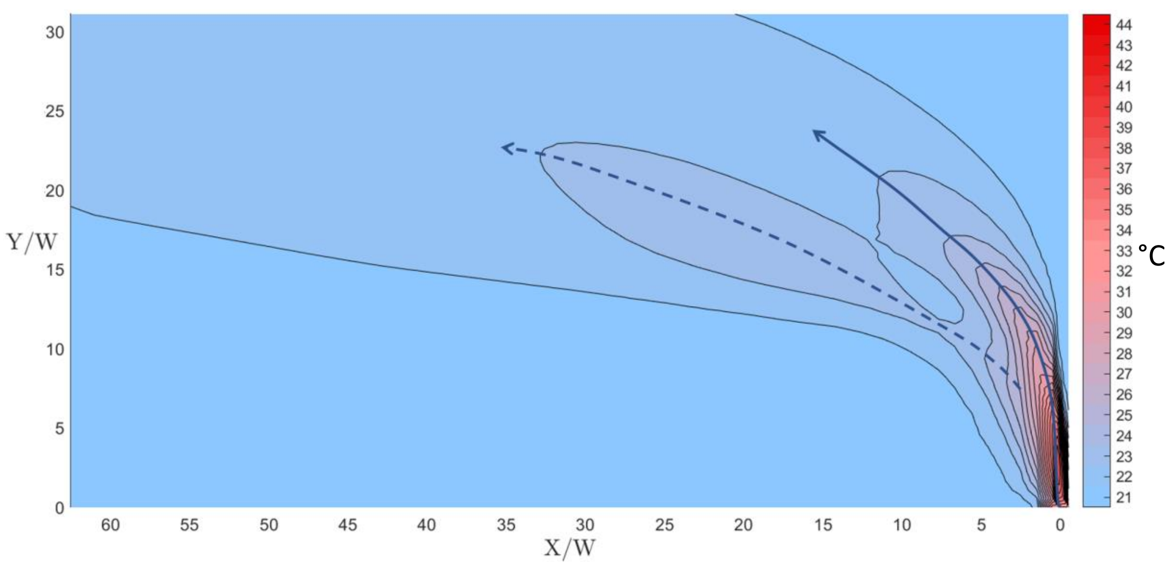

(a)

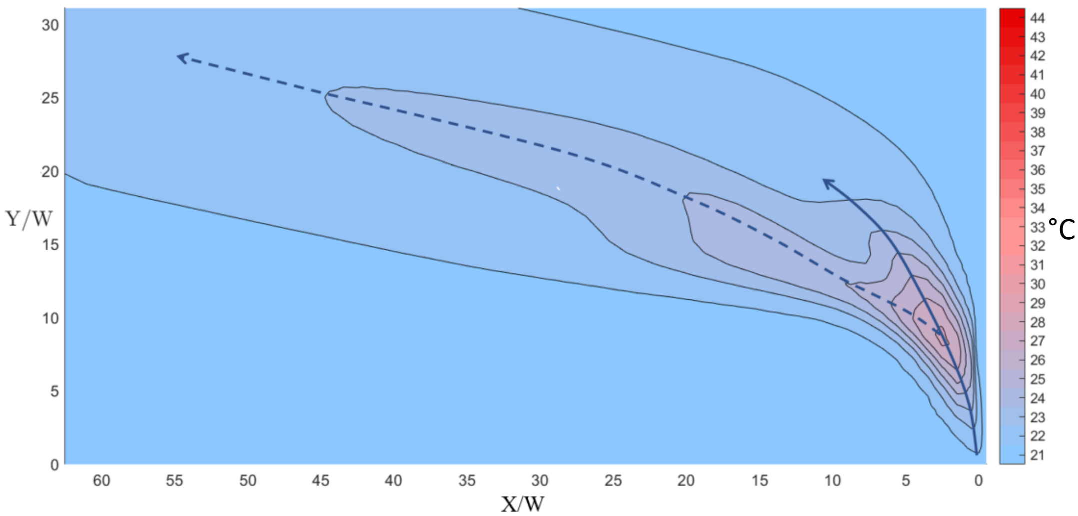

(b)

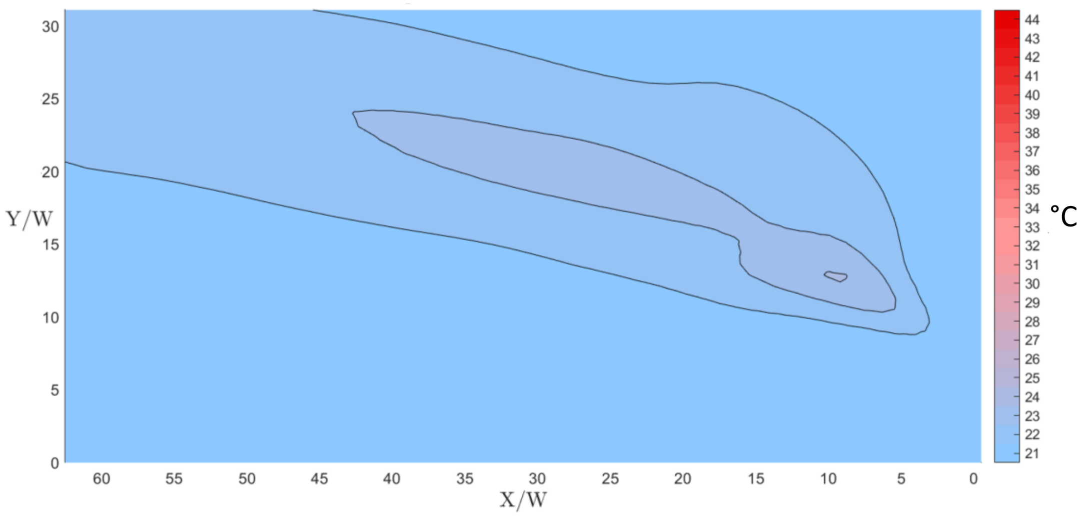

(c)

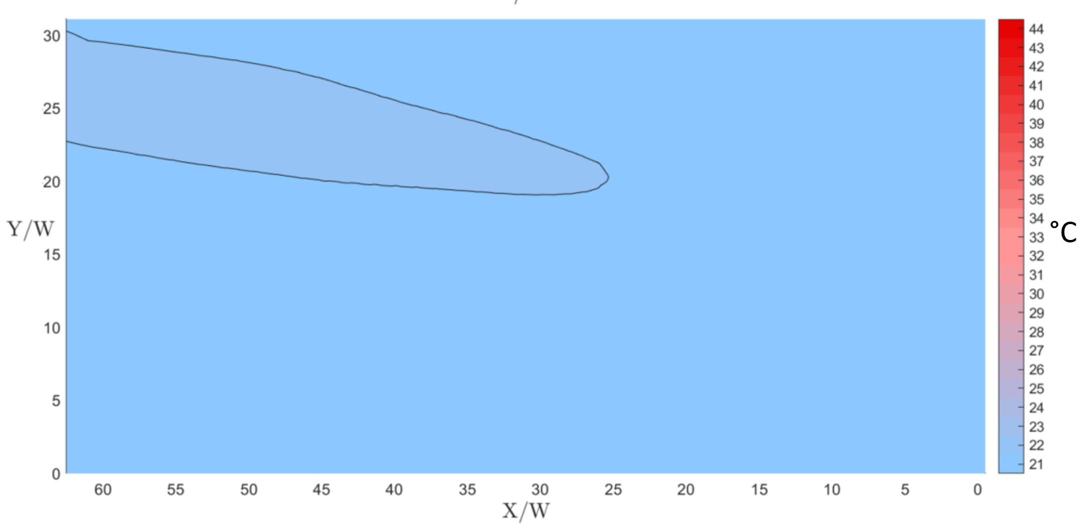

(d)

Figure 5.13 Plan view of mean temperature variation distributions in the mixing zone: (a) at Z/W = 1; (b) at Z/W = 2; (c) at Z/W = 4; and (d) at Z/W = 7;

The mean velocity distributions extracted from the numerical modelling results in the mixing zone are shown in Figure 5.14. The dotted contour line in Figure 5.14 represents the contour line related to the mean velocity in the Y direction equal to zero. Positive values are shown in darker gray shades.

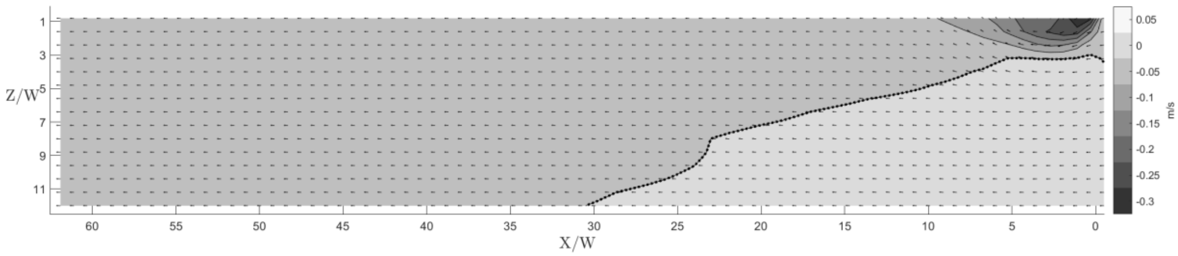

(a)

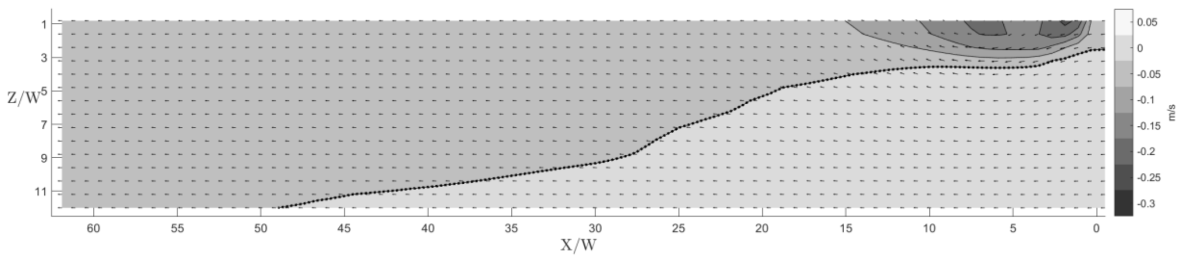

(b)

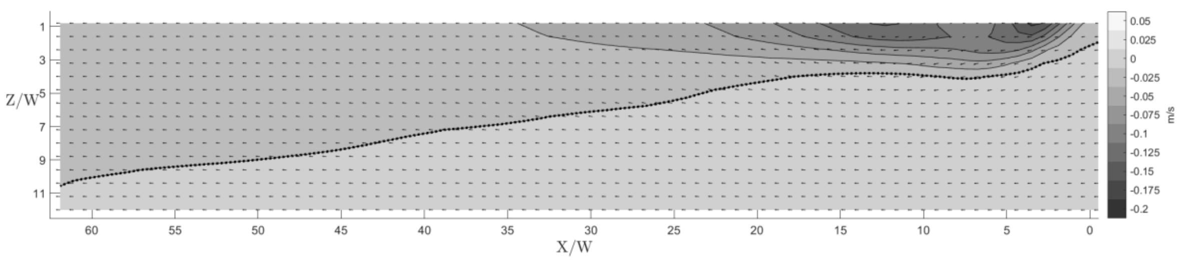

(c)

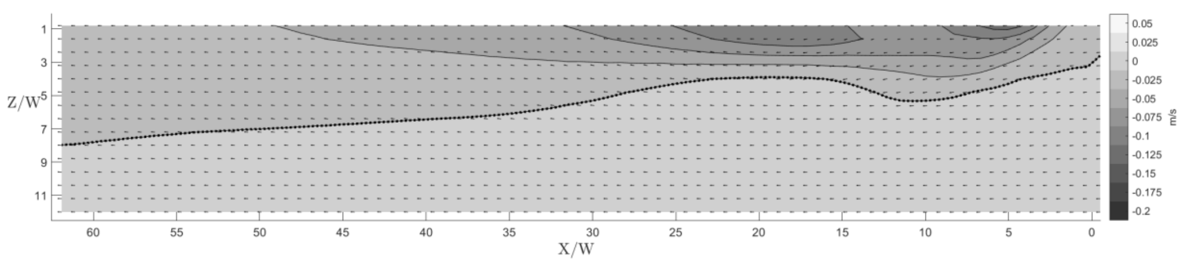

(d)

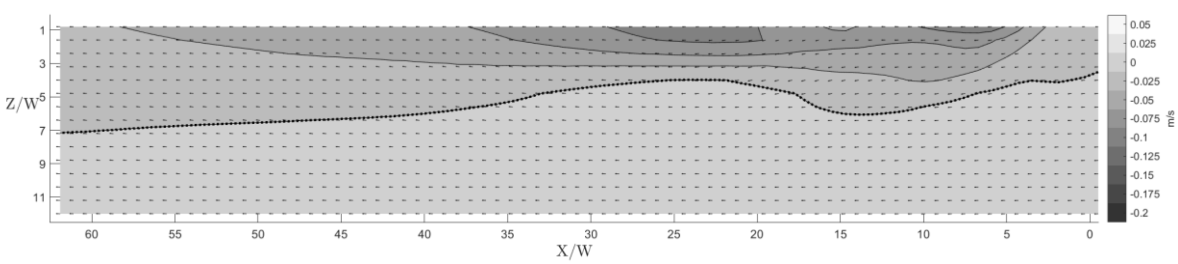

(e)

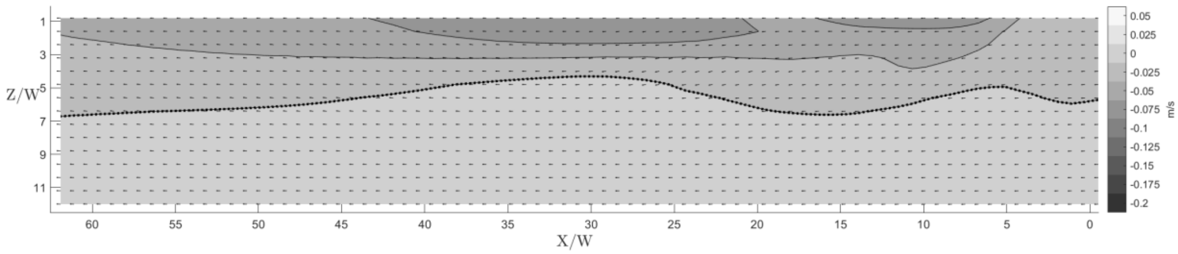

(f)

Figure 5.14 Mean velocity distribution in the mixing zone: (a) at Y/W = 7.8; (b) at Y/W = 11.1; (c) at Y/W = 14.3; (d) at Y/W = 17.3; (e) at Y/W = 19.1; and (f) at Y/W = 21.0

A comparison of the velocity components from numerical modelling results with experimental reported data showed a similar jet flow structure in the mixing zone. For example, the vertical mean velocity component distribution at Plane (B) is shown in Figure 5.15(a) with upward velocity values with a maximum of 0.05 m/s.

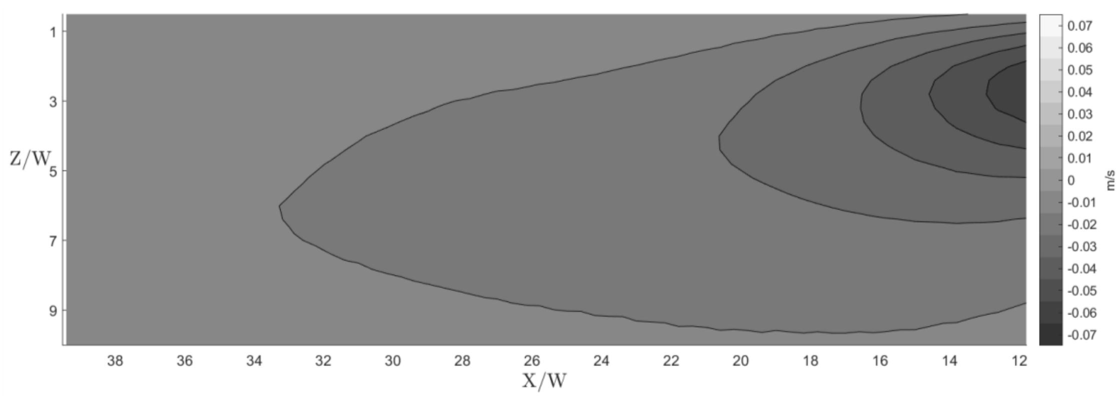

(a)

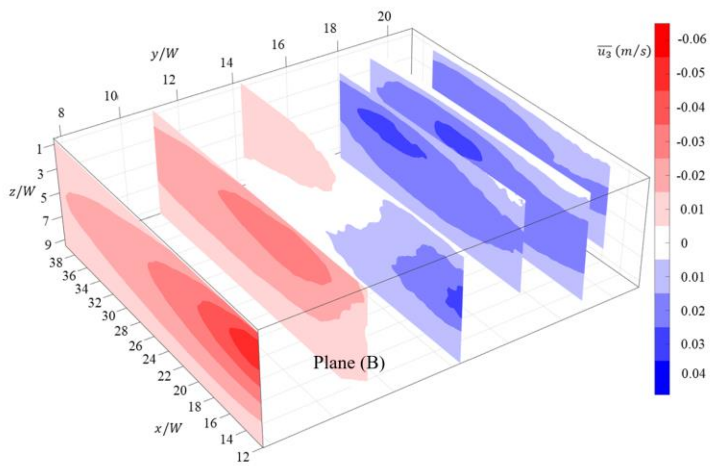

(b)

Figure 5.15 Mean vertical velocity component distribution: (a) numerical simulation on Plane (B); (b) experimental study by Gharavi et al. (2020)

The mean velocity distribution for Plane (C) is shown in Figure 5.16. The zero-velocity contour line for the velocity component in the Y direction is shown with a dotted line. Positive values are shown in darker gray shades with contour intervals of 0.01 m/s. The dotted line is approximately horizontal up to the length of 20W from the discharge point at $Y/W \approx 4$ in Figure 5.16(a). This matches with the experimental data shown in Figure 5.16 (b)

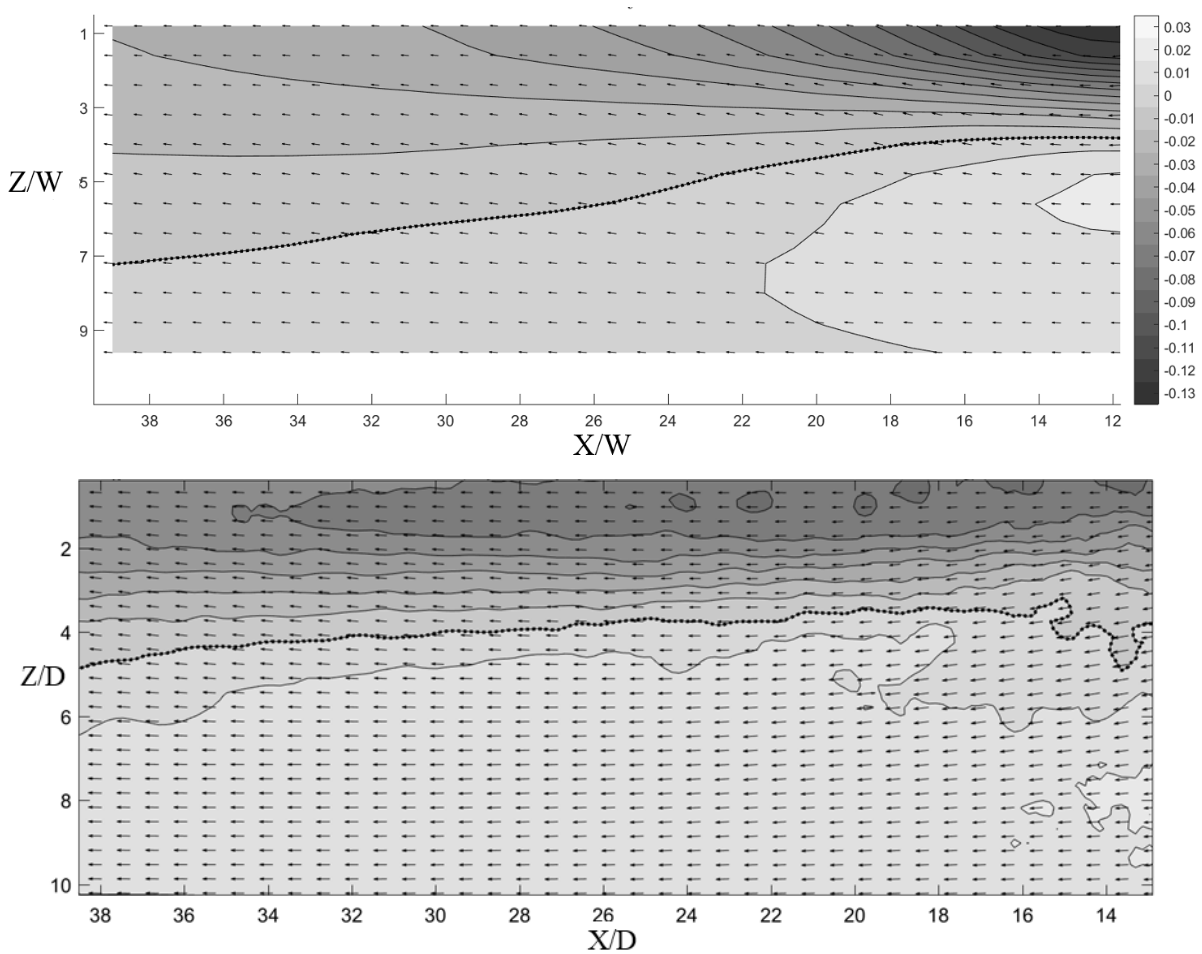

(a)

(b)

Figure 5.16 Mean velocity distribution on Plane (C) extracted from: (a) numerical simulation; (b) experimental study by Gharavi et al. (2020)

Mean turbulent kinetic energy ($\bar{k}$) was extracted from numerical model on Plane C. The results are shown in Figure 5.17 (a). Lower values of $\bar{k}$ were observed in the numerical model compared to the experimental measurement. The general trend of the in the $\bar{k}$ distributions is the same as observed experimental data. Lower reported values from numerical modelling work might be because of coarser mesh resolution in the numerical model (almost 0.01 m in Plane (C)) compared with the measured experimental PIV data 0.004 m.

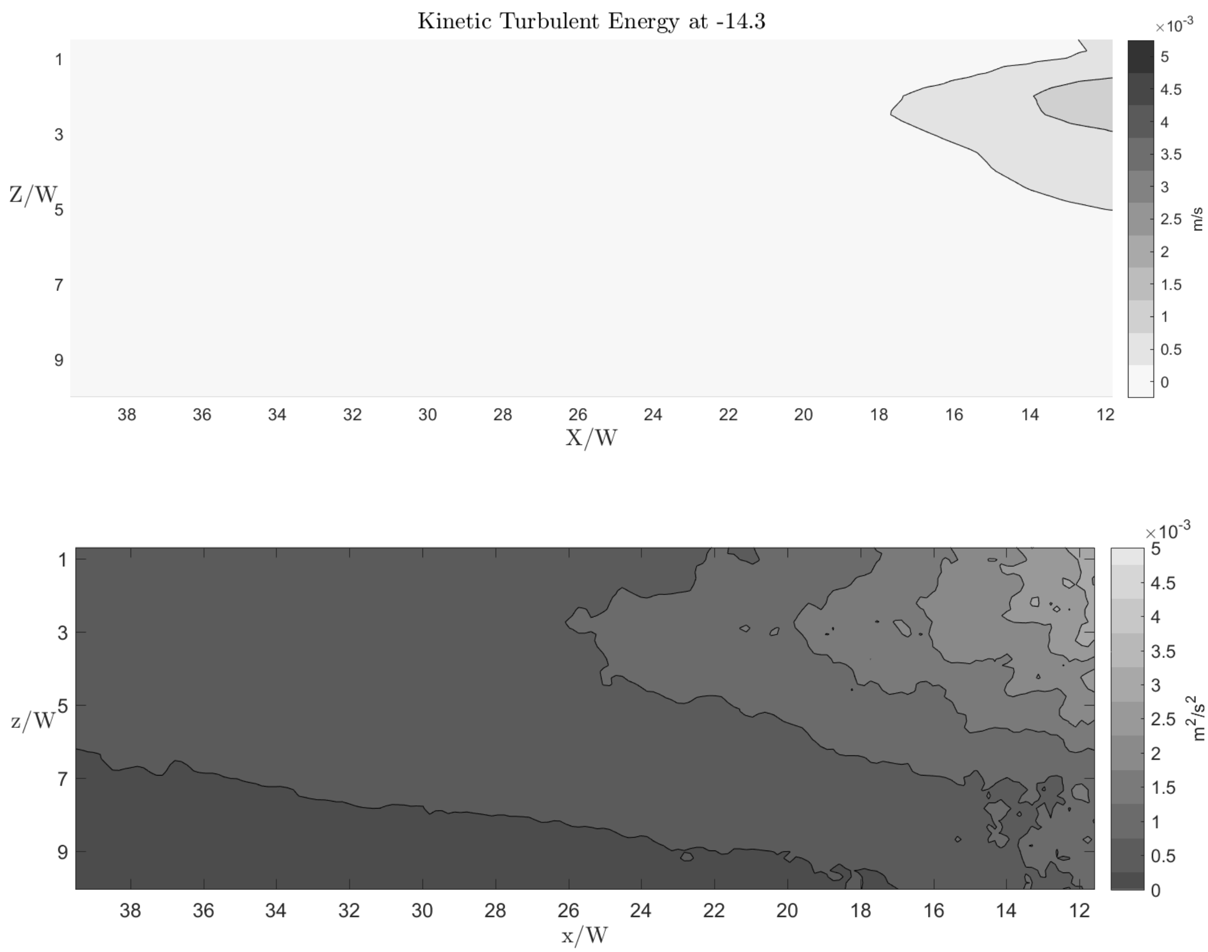

(a)

(b)

Figure 5.17 Mean Turbulent Kinetic Energy on Plane (C) extracted from: (a) numerical simulation; (b) experimental study by Gharavi et al. (2020)

5.5 Summary and Conclusions

Numerical modelling simulations for two cases of a surface buoyant jet in crossflow were investigated in this study. Mean temperature and velocity distributions were extracted from the numerical results and compared with the experimental works of Anwar (1987) and Gharavi et al. (2020). Numerical models were capable of predicting the flow structures and jet centerline in the mixing zone similar to the experimental measurements. Flow structure characteristics were observed as follows:

1. Numerical modelling results for both cases showed that the surface jet and crossflow interaction created a region with higher velocity (Ux) in outer edge of the jet. The increase in longitudinal velocity strengthen in depth ranging from 0.35 m/s in the surface to 0.40 m/s deeper in the water. These values shall be compared with the crossflow velocity of 0.29 m/s.
2. The flow structure in the mixing zone was heavily affected by the interaction of the jet and crossflow. This interaction acted similar to existence of a barrier in the crossflow, right in front of the discharge point. Numerical model was able to capture a wake-type slow-moving zone between the jet centerline and the inner wall of the flume.
3. Additionally, secondary jet axis in the slow-moving region was observed in the numerical modelling results for both cases. Values of temperature peaked on this secondary axis in the slow-moving zone. Numerical models for both of the cases were able to capture this slow-moving zone in the flow structure of the mixing zone.
4. Secondary flows (in plan view) were observed in the flow structure of the jet in the mixing zone for Case 1. This secondary flow appeared in the form of return flow downstream of the discharge point and closer to inner walls. Numerical model was able to successfully replicate and quantify the amount of the return flow. Maximum longitudinal velocities (Ux) in the return flow varied from 0.05 m/s closer to water surface to 0.10 m/s deeper in the water.
5. A vortex was observed in the vertical sections of the jet flow structure in mixing zone. The changes in the direction of the vertical velocity (Uz) component captured the magnitude of this circulation. Maximum values of Uz was reported close to 0.10 m/s towards the bottom of the flume and 0.06 m/s towards the surface of the water in the numerical modelling results.
6. A comparison of LRR and LES model in Case 1 showed that the LES model was able to predict the location of jet axis better than LRR model using the same number of mesh in the numerical model.
7. Numerical model with the free surface assumption was able to successfully replicate the experimental data of Gharavi et al. (2020) for average velocity components in the flow structure of the jet in mixing zone. However, turbulent characteristics of the flow was not exactly replicated. The reason might be because of the finer resolution of the experimental data measurement compared to the numerical grid cell sizes. The numerical model was able

to replicate the same distribution for the turbulent kinetic energy with higher values closer to the discharge point.

6 Conclusions and Recommendations

6.1 Summary of the Findings

This study aimed to improve the understanding of the mixing phenomenon and flow structure of surface jets in crossflows and stagnant water bodies. A lack of comprehensive numerical studies in the field of surface jets in crossflows was the main motivation for this study. In order to assess the reliability of the results obtained from numerical studies, the numerical results were compared with existing measured data. Most of the experimental data in this field were focused on the thermal and concentration distributions in the mixing zone of the surface jets in crossflows. In this study, Stereo-PIV technique was used to measure 3-D velocity components on 2D sections in the mixing zone of surface jets in crossflows and stagnant water bodies. Additionally, numerical modelling works were performed using OpenFOAM.

The flow characteristics of turbulent mixing regimes of surface buoyant jets in crossflow conditions were obtained using Stereo-PIV for the first time. The mean and turbulent flow characteristics (such as the turbulent kinetic energy dissipation rate ϵ and turbulent stresses) extracted directly from the Stereo-PIV measurements could be of interest for the computational fluid dynamics community as it may help improve the numerical modelling of surface jets in crossflows, useful for the study of the jet dispersion systems. Measurements were conducted at six longitudinal planes, perpendicular to the surface jet axis, downstream of the discharge point. The Stereo-PIV measurement planes covered a volume of water delineated by a water depth of up to $9.8W$ ($W = 8$ mm) and a width of up to $39W$. The following observations were obtained from the experimental works in the current study:

- Using the Stereo-PIV technique in this field made it possible to detect two types of circulations observed in the flow structure that were not previously stated in the literature related to the surface jets in crossflows.
- A downstream-propagating vortex was observed at the transverse planes in the flow structure, inside the mixing zone of the surface jet. Mean velocity streamlines showed the existence of this vortex occurring up to a distance of $35W$ downstream of the discharge

point. Mean excess velocity streamlines showed a circulation in the middle of the mixing zone at the longitudinal planes.

- The isosurfaces of streamwise velocity showed a slow-moving flow zone in the regions closer to the water surface and higher streamwise velocity underneath the surface jet.
- The distribution of the normal stress terms showed that the dominant component of turbulent kinetic energy ($\bar{k}$) was $\overline{u_2'^2}$, which was one of the main velocity components (jet velocity) of the vortex in transverse planes. This confirms that the structure of the turbulence is anisotropic in the transverse (y) direction compared to the x- and z- directions.
- The calculated values of ϵ from the measured Stereo-PIV data showed that the inclusion of the transversal component of the velocity ($\overline{u'_2}$) led to 1.5 times larger values for ϵ compared to the ones calculated from the in-plane components of the velocity. This demonstrates that the local isotropy assumption produces smaller values for the terms $\overline{\left(\frac{\partial u_2'}{\partial x_1}\right)^2}$ and $\overline{\left(\frac{\partial u_2'}{\partial x_3}\right)^2}$ in this complex flow structure, where x_1 and x_3 are the streamwise and vertical length components.
- As a result of the highly turbulent flow in the middle of the measurement zone, flow characteristics such as k, ϵ, and υ_t (turbulent eddy viscosity) typically reached their highest values in this region. Considerable variations of normal shear stress, from a large positive value in the regions closer to the water surface to a high positive value deeper in the water, showed the existence of the span-wise vorticity in the flow, mainly caused by Kelvin-Helmholtz instability.

Numerical modelling simulations for two cases of surface buoyant jets in crossflows were investigated in this study using OpenFOAM. Mean temperature and velocity distributions were extracted from the numerical results and compared with the experimental works of Anwar (1987) and Gharavi et al. (2020). The following observations were obtained from the numerical modelling works for surface buoyant jets in crossflows in the current study:

- Numerical models predicted the flow structures and jet axis in the mixing zone similar to the observations reported in the experimental study.
- Surface jet and crossflow interaction created a region with higher longitudinal velocity magnitudes, which was caused by the mutual deflection of the surface jet and crossflow.

- A wake type slow-moving zone was created between the jet axis and the inner wall of the flume.
- A secondary jet axis was observed in the slow-moving zone. This secondary jet axis was obtained by connecting the locations of the peak isotherms in the plan view in that region. Numerical modelling results were capable of reproducing the existence of the secondary jet axis.
- Secondary flows were captured in the flow structure of the jet in the mixing zone. The magnitudes of the secondary current velocities were measured based on the distribution of the mean velocity components in each direction.
- A comparison of LRR and LES model in Case 1 showed that the LES model was able to predict the location of jet axis better than LRR model using the same number of mesh in the numerical model

6.2 Limitations of the Current Study

The following are the key limitations in the experimental works of this study:

- Moving the discharge nozzle and camera on a cart to simulate the crossflow velocity was a challenge. The main reason was that each experimental measurement could only last approximately 10 seconds because of the limited length of the flume and laser light intensity in the field of view. Additionally, stagnant water does not include the background eddies and turbulence as in a crossflow, which may have some effects on flow structures and mixing of the jets in crossflows.
- Data measurement frequency was limited based on the Stereo-PIV equipment used. There is balance between the frequency of measured data and the scope of work. For example, some investigation of the turbulent flow characteristics such as flow instability analysis needs a data measurement with higher frequency.
- The spatial resolution of the measured data was limited because of the discharge nozzle size and camera lenses. A larger nozzle would change the water level in the flume significantly, which would change the amount of flow in one experiment.

- Reflections of the laser from the surface of the water made it impossible to do experimental measurements closer to the water surface.
- The density difference between jet and crossflow water was limited in this study because the warm water temperature was limited to 45° C due to the image quality required for PIV. When the temperature difference between jet and ambient was more than 30° C, the PIV captured blurry images, which were not useful for image processing.

Limitations of the conducted numerical simulations are as follows:

- Investigations of different turbulence models were limited to LRR Reynolds stress turbulence models and LES approach in this study. Numerical simulations were conducted on two Lenovo PCs with Intel Core i7-4970 CPU @ 3.6 GHz x 8. Post-processing of each modelling approach was time consuming and produced a large quantity of data. For example, the LES modelling work for Case 1 took 4 days (100 hours) to finalize the simulation. The extracted processed files in CSV file format were 143 GB for 1300 snapshots. This caused a limitation on the number of turbulence models investigated in the current study.

6.3 Recommendations for Future Work

The list of recommendations for potential future studies are summarized as follows:

- Conduct Stereo-PIV experiments for negatively buoyant surface jets in crossflows and stagnant water bodies.
- Conduct Stereo-PIV experiments for horizontal submerged buoyant and negatively buoyant jets in crossflows and stagnant water bodies.
- Perform experimental assessment of the concentration (or temperature) distributions for surface jets in crossflows using nonintrusive methods such as LIF.
- Perform velocity and concentration (or temperature) distribution measurements using the coupled PIV-LIF technique for surface jets in crossflows.

- Use the tomographic PIV for velocity measurement in a volume of water in the mixing zone of surface jets in crossflows.
- Expand the current study to a different jet to crossflow velocity ratio, jet discharge angle, jet height to crossflow depth ratio and investigate the effects on the flow structures.
- Expand the current study using different turbulence models such as dynamic kinetic energy sub-grid-scale model. Use the hybrid RANS-LES models such as detached eddy simulation (DES) and delayed detached eddy simulation (DDES).
- Investigate numerically and experimentally the effects of uniform crossflow versus the use of stagnant water as crossflow (moving a surface jet in stagnant water) and the impacts on the flow structures.
- Undertake a numerical investigation of the limitations on the use of rigid surface assumption in surface jets in crossflows. For example, using a discharge nozzle in different depths of water.

References

Abdelwahed, M.S.T. 1983. *Surface jets and surface plumes in cross-flows*.

Abdelwahed, M.S.T. 1981. Surface jets and surface plumes in cross-flows.

Abessi, O. and Roberts, P.J.W. 2016. Dense Jet Discharges in Shallow Water. *J. Hydraul. Eng.*, **142**: 04015033.

Abessi, O., Saeedi, M., Davidson, M. and Zaker, N.H. 2011. Flow classification of negatively buoyant surface discharge in an ambient current. *J. Coast. Res.*, **28**: 148–155.

Adams, E.E., Harleman, D.R. and Stolzenbach, K.D. 1975. *Near and far field analysis of buoyant surface discharges into large bodies of water*.

Andreopoulos, J. and Rodi, W. 1984. Experimental investigation of jets in a crossflow. *J. Fluid Mech.*, **138**: 93–127.

Anwar, H.O. 1987. Flow of Surface Buoyant Jet in Cross Flow. *J. Hydraul. Eng.*, **113**: 892–904.

Arita, M., Jirka, G.H. and Tamai, N. 1986. Classification and mixing of two-dimensional buoyant surface discharges. *J. Hydraul. Res.*, **24**: 333–345.

Brouwer, R.L., de Schipper, M.A., Rynne, P.F., Graham, F.J., Reniers, A.J.H.M. and MacMahan, J.H. 2015. Surfzone Monitoring Using Rotary Wing Unmanned Aerial Vehicles. *J. Atmospheric Ocean. Technol.*, **32**: 855–863.

Camussi, R., Guj, G. and Stella, A. 2002. Experimental study of a jet in a crossflow at very low Reynolds number. *J. Fluid Mech.*, **454**: 113–144.

Cheung, S.K.B., Leung, D.Y.L., Wang, W., Lee, J.H.W. and Cheung, V. 2000. VISJET-a computer ocean outfall modelling system. In: *Computer Graphics International, 2000. Proceedings*, pp. 75–80.

Chu, V.H. and Goldberg, M.B. 1974. Buoyant forced-plumes in cross flow. *J. Hydraul. Div.*, **100**: 1203–1214.

Chu, V.H. and Jirka, G.H. 1986. Chapter 25: surface buoyant jets, encyclopedia of fluid mechanics. *Houst. Tex. Gulf Publ. Co. 155p*.

Chu, V.H. and Lee, J.H. 1996. General integral formulation of turbulent buoyant jets in cross-flow. *J. Hydraul. Eng.*, **122**: 27–34.

Coletti, F., Benson, M.J., Ling, J., Elkins, C.J. and Eaton, J.K. 2013. Turbulent transport in an inclined jet in crossflow. *Int. J. Heat Fluid Flow*, **43**: 149–160.

Cortelezzi, L. and Karagozian, A.R. 2001. On the formation of the counter-rotating vortex pair in transverse jets. *J. Fluid Mech.*, **446**: 347–373.

Cortelezzi, Luca and Karagozian, A.R. 2001. On the formation of the counter-rotating vortex pair in transverse jets. *J. Fluid Mech.*, **446**: 347–373.

Coussement, A., Gicquel, O. and Degrez, G. 2012a. Large eddy simulation of a pulsed jet in cross-flow. *J. Fluid Mech.*, **695**: 1–34.

Coussement, A., Gicquel, O. and Degrez, G. 2012b. Large eddy simulation of a pulsed jet in cross-flow. *J. Fluid Mech.*, **695**: 1–34.

Cutler, P.R.E. 2002. On the Structure and Mixing of a Jet in Cross-Flow.

Davidson, M.J. and Pun, K.L. 1998. Hybrid model for prediction of initial dilutions from outfall discharges. *J. Hydraul. Eng.*, **124**: 1188–1197.

Davidson, M.J. and Pun, K.L. 2000. Locating discharge trajectories in still and moving ambient fluids. *J. Hydraul. Eng.*, **126**: 513–524.

Dejoan, A. and Leschziner, M.A. 2005. Large eddy simulation of a plane turbulent wall jet. *Phys. Fluids*, **17**: 025102.

Delafosse, A., Collignon, M.-L., Crine, M. and Toye, D. 2011. Estimation of the turbulent kinetic energy dissipation rate from 2D-PIV measurements in a vessel stirred by an axial Mixel TTP impeller. *Chem. Eng. Sci.*, **66**: 1728–1737.

Denev, J.A., Fröhlich, J. and Bockhorn, H. 2009. Large eddy simulation of a swirling transverse jet into a crossflow with investigation of scalar transport. *Phys. Fluids*, **21**: 015101.

Doneker, R.L. 1990. CORMIX1: An expert system for hydrodynamic mixing zone analysis of conventional and toxic submerged single port discharges.

Doron, P., Bertuccioli, L., Katz, J. and Osborn, T.R. 2001. Turbulence characteristics and dissipation estimates in the coastal ocean bottom boundary layer from PIV data. *J. Phys. Oceanogr.*, **31**: 2108–2134.

Dunn, W.E., Policastro, A.J. and Paddock, R.A. 1975. *Water Resources Research Program. Surface thermal plumes: evaluation of mathematical models for the near and complete field*.

Erlebacher, G., Hussaini, M.Y., Speziale, C.G. and Zang, T.A. 1992. Toward the large-eddy simulation of compressible turbulent flows. *J. Fluid Mech.*, **238**: 155–185.

Esmaeili, M., Afshari, A. and Jaberi, F.A. 2015. Turbulent mixing in non-isothermal jet in crossflow. *Int. J. Heat Mass Transf.*, **89**: 1239–1257.

Fincham, A.M., Maxworthy, T. and Spedding, G.R. 1996. Energy dissipation and vortex structure in freely decaying, stratified grid turbulence. *Dyn. Atmospheres Oceans*, **23**: 155–169.

Fric, T.F. and Roshko, A. 1994a. Vortical structure in the wake of a transverse jet. *J. Fluid Mech.*, **279**: 1–47.

Fric, T.F. and Roshko, A. 1994b. Vortical structure in the wake of a transverse jet. *J. Fluid Mech.*, **279**: 1–47.

Gawad, S.T.A., McCorquodale, J.A. and Gerges, H. 1996a. Near-field mixing at an outfall. *Can. J. Civ. Eng.*, **23**: 63–75.

Gawad, S.T.A., McCorquodale, J.A. and Gerges, H. 1996b. Near-field mixing at an outfall. *Can. J. Civ. Eng.*, **23**: 63–75.

Germano, M., Piomelli, U., Moin, P. and Cabot, W.H. 1991. A dynamic subgrid-scale eddy viscosity model. *Phys. Fluids Fluid Dyn.*, **3**: 1760–1765.

Gharavi, A., Mohammadian, A., Nistor, I., Peña, E. and Anta, J. 2020. Experimental study of surface buoyant jets in crossflow. *Environ. Fluid Mech.*, **20**: 1007–1030.

Gildeh, H.K., Mohammadian, A., Nistor, I., Qiblawey, H. and Yan, X. 2015. CFD modeling and analysis of the behavior of 30 and 45 inclined dense jets—New numerical insights. *J Appl Water Eng Res*, **4**: 1–16.

Han, D. and Mungal, M.G. 2003. Simultaneous measurements of velocity and CH distribution. Part II: deflected jet flames. *Combust. Flame*, **133**: 1–17.

Han, D., Orozco, V. and Mungal, M.G. 2000. Gross-entrainment behavior of turbulent jets injected obliquely into a uniform crossflow. *AIAA J.*, **38**: 1643–1649.

Hasselbrink, E.F. and Mungal, M.G. 2001a. Transverse jets and jet flames. Part 1. Scaling laws for strong transverse jets. *J. Fluid Mech.*, **443**: 1–25.

Hasselbrink, E.F. and Mungal, M.G. 2001b. Transverse jets and jet flames. Part 2. Velocity and OH field imaging. *J. Fluid Mech.*, **443**: 27–68.

Haven, B.A. and Kurosaka, M. 1997. Kidney and anti-kidney vortices in crossflow jets. *J. Fluid Mech.*, **352**: 27–64.

Hetland, R.D. 2010. The effects of mixing and spreading on density in near-field river plumes. *Dyn. Atmospheres Oceans*, **49**: 37–53.

Hoque, M.M., Sathe, M.J., Mitra, S., Joshi, J.B. and Evans, G.M. 2015. Comparison of specific energy dissipation rate calculation methodologies utilising 2D PIV velocity measurement. *Chem. Eng. Sci.*, **137**: 752–767.

Jirka, G.H. 2007. Buoyant surface discharges into water bodies. II: Jet integral model. *J. Hydraul. Eng.*, **133**: 1021–1036.

Jirka, G.H. 2004. Integral Model for Turbulent Buoyant Jets in Unbounded Stratified Flows. Part I: Single Round Jet. *Environ. Fluid Mech.*, **4**: 1–56.

Jirka, G.H., Stolzenbach, K.D. and Adams, E.E. 1981. Buoyant surface jets. *J. Hydraul. Div.*, **107**: 1467–1487.

Jones, G.R., Nash, J.D., Doneker, R.L. and Jirka, G.H. 2007. Buoyant surface discharges into water bodies. I: Flow classification and prediction methodology. *J. Hydraul. Eng.*, **133**: 1010–1020.

Jones, G.R., Nash, J.D. and Jirka, G.H. 1996. *CORMIX3: An expert system for mixing zone analysis and prediction of buoyant surface discharges*.

Jones, J.M. 1983. A numerical technique for steady two-dimensional transcritical stratified flow problems. *Diss. Abstr. Int. Part B Sci. Eng. ABST INT PT B- SCI ENG*, **44**.

Jones, W.P. and Wille, M. 1996. Large-eddy simulation of a plane jet in a cross-flow. *Int. J. Heat Fluid Flow*, **17**: 296–306.

Kalita, K., Dewan, A. and Dass, A.K. 2002. Prediction of turbulent plane jet in crossflow. *Numer. Heat Transf. Part Appl.*, **41**: 101–111.

Keffer, Jf. and Baines, W.D. 1963. The round turbulent jet in a cross-wind. *J. Fluid Mech.*, **15**: 481–496.

Kelso, R.M., Lim, T.T. and Perry, A.E. 1996. An experimental study of round jets in cross-flow. *J. Fluid Mech.*, **306**: 111–144.

Kheirkhah Gildeh, H., Mohammadian, A., Nistor, I. and Qiblawey, H. 2015. Numerical modeling of 30° and 45° inclined dense turbulent jets in stationary ambient. *Environ. Fluid Mech.*, **15**: 537–562.

Kheirkhah Gildeh, H., Mohammadian, A., Nistor, I. and Qiblawey, H. 2014. Numerical modeling of turbulent buoyant wall jets in stationary ambient water. *J. Hydraul. Eng.*, **140**: 04014012.

Khosravi, M. and Javan, M. 2022. Three-dimensional features of the lateral thermal plume discharge in the deep cross-flow using dynamic adaptive mesh refinement. *Theor. Comput. Fluid Dyn.*, **36**: 405–422.

Khosravi, M. and Javan, M. 2020. Three-dimensional flow structure and mixing of the side thermal buoyant jet discharge in cross-flow. *Acta Mech.*, **231**: 3729–3753.

Kim, D.G. and Cho, H.Y. 2006. Modeling the buoyant flow of heated water discharged from surface and submerged side outfalls in shallow and deep water with a cross flow. *Environ. Fluid Mech.*, **6**: 501–518.

Kim, Y.D., Seo, I.W., Kang, S.W. and Oh, B.C. 2002. Jet integral–particle tracking hybrid model for single buoyant jets. *J. Hydraul. Eng.*, **128**: 753–760.

Knudsen, M. 1988. Buoyant horizontal jets in an ambient flow.

Lai, C.C. and Lee, J.H. 2014. Initial mixing of inclined dense jet in perpendicular crossflow. *Environ. Fluid Mech.*, **14**: 25–49.

Launder, B.E., Reece, G.J. and Rodi, W. 1975. Progress in the development of a Reynolds-stress turbulence closure. *J. Fluid Mech.*, **68**: 537–566.

Law, A.W.K. 2006. Velocity and Concentration Distributions of Round and Plane Turbulent Jets. *J. Eng. Math.*, **56**: 69–78.

Lilly, D.K. 1992. A proposed modification of the Germano subgrid-scale closure method. *Phys. Fluids Fluid Dyn.*, **4**: 633–635.

Ma, F., Satish, M. and Islam, M.R. 2007. Large eddy simulation of thermal jets in cross flow. *Eng. Appl. Comput. Fluid Mech.*, **1**: 25–35.

Mahesh, K. 2013. The Interaction of Jets with Crossflow. *Annu. Rev. Fluid Mech.*, **45**: 379–407.

Malcangio, D., Ben Meftah, M., Chiaia, G., De Serio, F., Mossa, M. and Petrillo, A.F. 2016. Experimental studies on vertical dense jets in a crossflow. In: *River Flow 2016 (Constantinescu G., Garcia, M., & Hanes, D. Eds.)*, pp. 890–897.

Malcangio, D., Ben Meftah, M. and Mossa, M. 2016. Physical modelling of buoyant effluents discharged into a cross flow. In: *2016 IEEE Workshop on Environmental, Energy, and Structural Monitoring Systems (EESMS)*, pp. 192–197.

McCorquodale, J.A. 2007. Storm-water jets and plumes in rivers and estuaries. *Can. J. Civ. Eng.*, **34**: 691–702.

McGuirk, J.J. and Rodi, W. 1978. A depth-averaged mathematical model for the near field of side discharges into open-channel flow. *J. Fluid Mech.*, **86**: 761–781.

McGuirk, J.J. and Rodi, W. 1979. Mathematical modelling of three-dimensional heated surface jets. *J. Fluid Mech.*, **95**: 609–633.

Meftah, M.B., Malcangio, D., De Serio, F. and Mossa, M. 2018. Vertical dense jet in flowing current. *Environ. Fluid Mech.*, **18**: 75–96.

Mier-Torrecilla, M. de, Geyer, A., Phillips, J.C., Idelsohn, S.R. and Onate, E. 2012. Numerical simulations of negatively buoyant jets in an immiscible fluid using the Particle Finite Element Method. *Int. J. Numer. Methods Fluids*, **69**: 1016–1030.

Miller, D.S. and Brighouse, B.A. 1984. *Thermal discharges: a guide to power and process plant cooling water discharges into rivers, lakes, and seas*.

Millero, F.J. and Poisson, A. 1981. International one-atmosphere equation of state of seawater. *Deep Sea Res. Part Oceanogr. Res. Pap.*, **28**: 625–629.

Nash, J.D. and Jirka, G.H. 1995. Buoyant Discharges in Reversing Ambient Currents. Experimental Investigation and Prediction. *Md. Dep. Nat. Resour. Jan 1995*.

Oliver, C.J., Davidson, M.J. and Nokes, R.I. 2008. k-ε Predictions of the initial mixing of desalination discharges. *Environ. Fluid Mech.*, **8**: 617.

Palomar, P., Lara, J.L. and Losada, I.J. 2012. Near field brine discharge modeling part 2: Validation of commercial tools. *Desalination*, **290**: 28–42.

Peng, S.-H. and Davidson, L. 2001. Large eddy simulation for turbulent buoyant flow in a confined cavity. *Int. J. Heat Fluid Flow*, **22**: 323–331.

Pilechi, A. 2016. Numerical Modelling and Field Study of Thermal Plume Dispersion in Rivers and Coastal Waters.

Pilechi, A., Rennie, C.D., Mohammadian, A. and Zhu, D.Z. 2015. In situ spatially distributed field measurements of transverse dispersion of a wastewater effluent in an extended natural meandering river. *J. Hydraul. Res.*, **53**: 20–35.

Pope, S.B. 2001. *Turbulent flows*.

Pratte, B.D. and Baines, W.D. 1967. Profiles of the round turbulent jet in a cross flow. *J. Hydraul. Div.*, **93**: 53–64.

Saha, A.K. and Yaragani, C.B. 2012. Three-dimensional numerical study of jet-in-crossflow characteristics at low Reynolds number. *Heat Mass Transf.*, **48**: 391–411.

Shan, J.W. and Dimotakis, P.E. 2006. Reynolds-number effects and anisotropy in transverse-jet mixing. *J. Fluid Mech.*, **566**: 47–96.

Shao, D. and Law, A.W.K. 2010. Mixing and boundary interactions of 30 and 45 inclined dense jets. *Environ. Fluid Mech.*, **10**: 521–553.

Shao, D. and Law, A.W.-K. 2009. Turbulent mass and momentum transport of a circular offset dense jet. *J. Turbul.*, N40.

Shirazi, M.A. and Davis, L.R. 1974. *Workbook of thermal plume prediction. Volume 2. Surface discharge*.

Smagorinsky, J. 1963. General circulation experiments with the primitive equations: I. The basic experiment. *Mon. Weather Rev.*, **91**: 99–164.

Smith, S.H. and Mungal, M.G. 1998. Mixing, structure and scaling of the jet in crossflow. *J. Fluid Mech.*, **357**: 83–122.

Song, C.G., Seo, I.W. and Do Kim, Y. 2012. Analysis of secondary current effect in the modeling of shallow flow in open channels. *Adv. Water Resour.*, **41**: 29–48.

Su, L.K. and Mungal, M.G. 2004. Simultaneous measurements of scalar and velocity field evolution in turbulent crossflowing jets. *J. Fluid Mech.*, **513**: 1–45.

Taherian, M. and Mohammadian, A. 2021. Buoyant jets in cross-flows: review, developments, and applications. *J. Mar. Sci. Eng.*, **9**: 61.

Thompson, L., Natsui, G., Velez, C., Kapat, J. and Vasu, S.S. 2016. Planar Laser-Induced Fluorescence Experiments and Modeling Study of Jets in Crossflow. *J. Fluids Eng.*, **138**: 081201.

Vafeiadou, P., Papakonstantis, I. and Christodoulou, G. 2005. Numerical simulation of inclined negatively buoyant jets. In: *The 9th international conference on environmental science and technology, September*, pp. 1–3.

Van Maele, K. and Merci, B. 2006. Application of two buoyancy-modified k–ε turbulence models to different types of buoyant plumes. *Fire Saf. J.*, **41**: 122–138.

Weber, L.J., Schumate, E.D. and Mawer, N. 2001. Experiments on flow at a 90 open-channel junction. *J. Hydraul. Eng.*, **127**: 340–350.

Weller, H.G., Tabor, G., Jasak, H. and Fureby, C. 1998. A tensorial approach to computational continuum mechanics using object-oriented techniques. *Comput. Phys.*, **12**: 620–631.

Westerweel, J. 1994. Efficient detection of spurious vectors in particle image velocimetry data. *Exp. Fluids*, **16**: 236–247.

Wieneke, B. 2005. Stereo-PIV using self-calibration on particle images. *Exp. Fluids*, **39**: 267–280.

Wood, I.R. 1993. Asymptotic solutions and behavior of outfall plumes. *J. Hydraul. Eng.*, **119**: 553–580.

Wright, S.J. 1977. Effects of ambient crossflows and density stratification on the characteristic behavior of round turbulent buoyant jets.

Wright Steven J. 1984. Buoyant Jets in Density-Stratified Crossflow. *J. Hydraul. Eng.*, **110**: 643–656.

Xu, D. and Chen, J. 2013. Accurate estimate of turbulent dissipation rate using PIV data. *Exp. Therm. Fluid Sci.*, **44**: 662–672.

Yan, X. and Mohammadian, A. 2017. Numerical Modeling of Vertical Buoyant Jets Subjected to Lateral Confinement. *J. Hydraul. Eng.*, **143**: 04017016.

Yimer, I., Campbell, I. and Jiang, L.-Y. 2002. Estimation of the turbulent Schmidt number from experimental profiles of axial velocity and concentration for high-Reynolds-number jet flows. *Can. Aeronaut. Space J.*, **48**: 195–200.

Yuan, L.L., Street, R.L. and Ferziger, J.H. 1999. Large-eddy simulations of a round jet in crossflow. *J. Fluid Mech.*, **379**: 71–104.

Yu-hong, Z. and Wen-xin, H. 2005. Numerical study on the stability and mixing of vertical round buoyant jet in shallow water. *Appl. Math. Mech.*, **26**: 92–100.

Zhang, L. and Yang, V. 2017. Flow Dynamics and Mixing of a Transverse Jet in Crossflow—Part I: Steady Crossflow. *J. Eng. Gas Turbines Power*, **139**: 082601.

Zhang, S., Jiang, B., Law, A.W.-K. and Zhao, B. 2016. Large eddy simulations of 45 inclined dense jets. *Environ. Fluid Mech.*, **16**: 101–121.

Zhang, S., Law, A.W.-K. and Jiang, M. 2017. Large eddy simulations of 45° and 60° inclined dense jets with bottom impact. *J. Hydro-Environ. Res.*, **15**: 54–66.

Zhao, Z., Wen, F., Tang, X., Luo, Y., Hou, R. and Wang, Z. 2021. Large Eddy Simulation of an Inclined Jet in Crossflow with Vortex Generators. *Int. J. Heat Mass Transf.*, **170**: 121032.

Zhiyin, Y. 2015. Large-eddy simulation: past, present and the future. *Chin. J. Aeronaut.*, **28**: 11–24.

Appendix A: Surface Jets in Stagnant Water

Appendix A: Surface Jets into Stagnant Water

In this Appendix effects of free surface on mixing is considered for surface jets in stagnant water. A series of experiments have been conducted in the lab for surface discharge into stagnant water. In this case water surface can oscillate freely. As the jet discharged at the surface of the water, surface oscillations were clearly observed particularly in the zones closer to the nozzle outlet. In order to simulate the surface oscillations, it was needed to define two phase flow in addition to including air.

A.1 Experimental Procedure

In this case there is no crossflow. The jet discharges flow with the same density (non-buoyant mixing) to study velocity vectors and secondary currents generated as a result of surface jet discharge into stagnant water. Same procedure as mentioned before in part 3.1.4, was used to capture Stereo-PIV and 2D-PIV images and perform necessary pre-processing. Experimental details are shown in Table A.1 for non-buoyant stagnant case.

Table A.1 Experimental details for non-buoyant stagnant case

	Stagnant-parallel with jet axis			
	$\Delta X(mm)$	Test Name	T_a℃	T_0℃
Case 1	from 0 to 176	Axis 1	18.4	18.7
Case 2	from 167 to 344	Axis 2	18.4	18.7
	Stagnant-perpendicular to jet axis			
	$\Delta Z(mm)$	Test Name	T_a℃	T_0℃
Case 3	173	C1T1	18.5	18.7
Case 4	232	C2T1	18.5	18.7

A.1.2 Experimental Results and Discussions

Velocity vector distributions are shown in this section. Experimental results of velocity on the jet axis were measured using 2D-PIV technique (Figure A.1). In this case average velocity of the nozzle was $0.69\, m/s$. However, as the velocity profile developed in the nozzle, higher value for velocity was created in front of the nozzle with the maximum values of $0.9\, m/s$. Figure A.1 shows a fully Gaussian distribution of the velocity in Point A. The mean velocity distribution shows the drop in velocity magnitude to $0.3\, m/s$ in the water surface at $\Delta X = 21.6$W (W = 8 mm) far from the nozzle.

Velocity vectors distribution and Ux contour line show that the velocity profile is almost half Gaussian distribution with the maximum at the surface (point A in Figure A.1(a)) and almost linear far from the nozzle. Transition from the jet-like flow (point A) to plume-like flow (point B) is clear in Figure A.1(a). Dark area in Figure A.1(a) shows the zone with average velocity of almost zero. It was observed that the jet expands vertically from point A to point B.

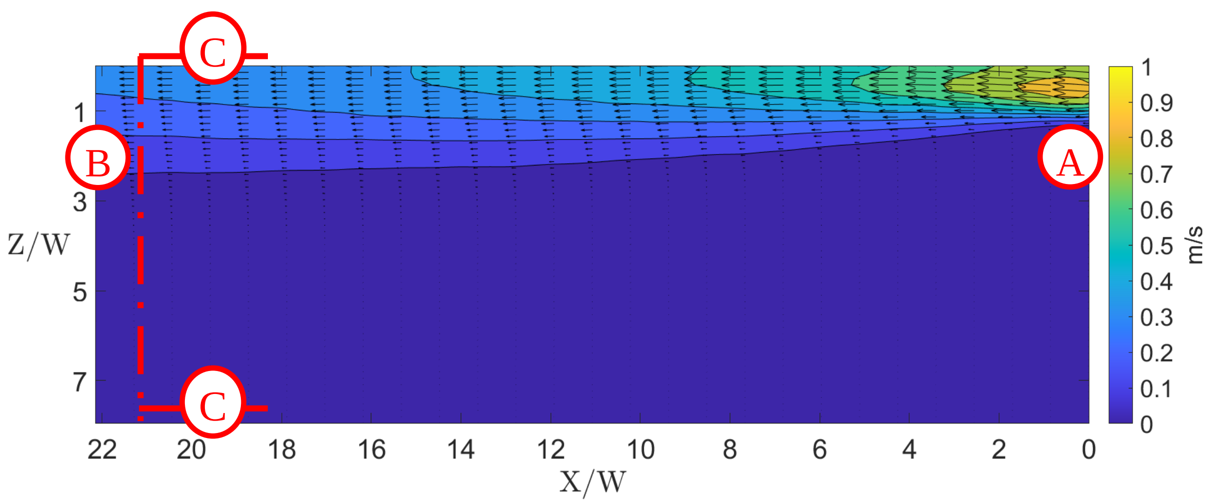

(a)

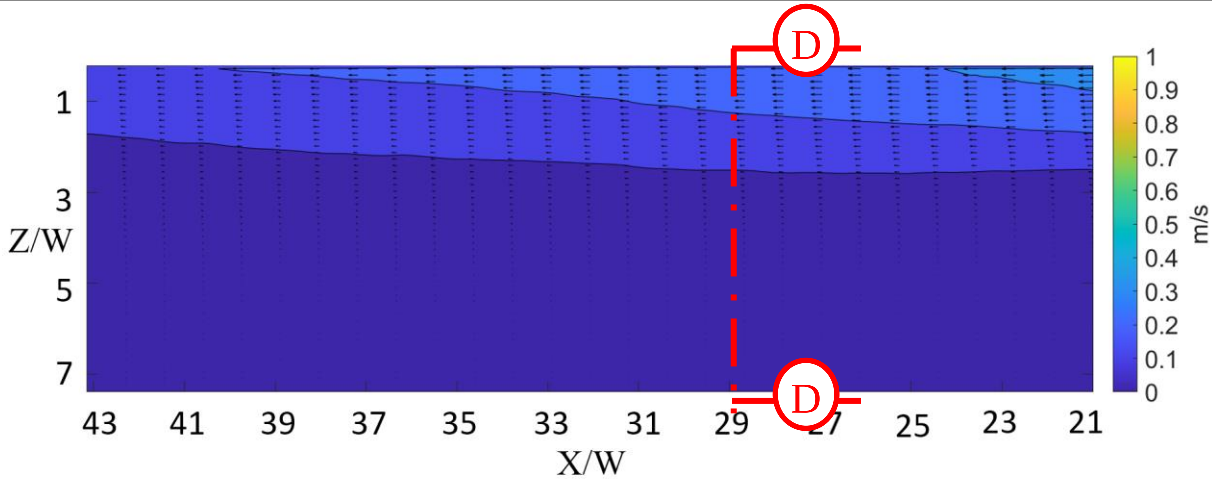

(b)

Figure A.1 The average velocity distribution on jet axis: (a) from 0 to 22W (b) from 21W to 43W

Section C-C in Figure A.1(a) was perpendicular to jet axis and 21.6W away from the nozzle outlet. Maximum value of the velocity is 0.31 *m/s* in the same direction as jet with minor return flow with the maximum magnitude of 0.006 *m/s* towards the jet. At this location the zero-velocity contour was 5W deep in water. Velocity distribution associated with section D-D is shown in Figure A.2 (b). Stereo-PIV technique was used to extract the velocity distributions. Maximum value of the velocity occurred on the jet axis and the values are well-matched with the results shown in Figure A.2. Velocity contours in Figure A.2 are symmetrical which was a challenge for the alignment of the setup especially cameras, laser and the nozzle.

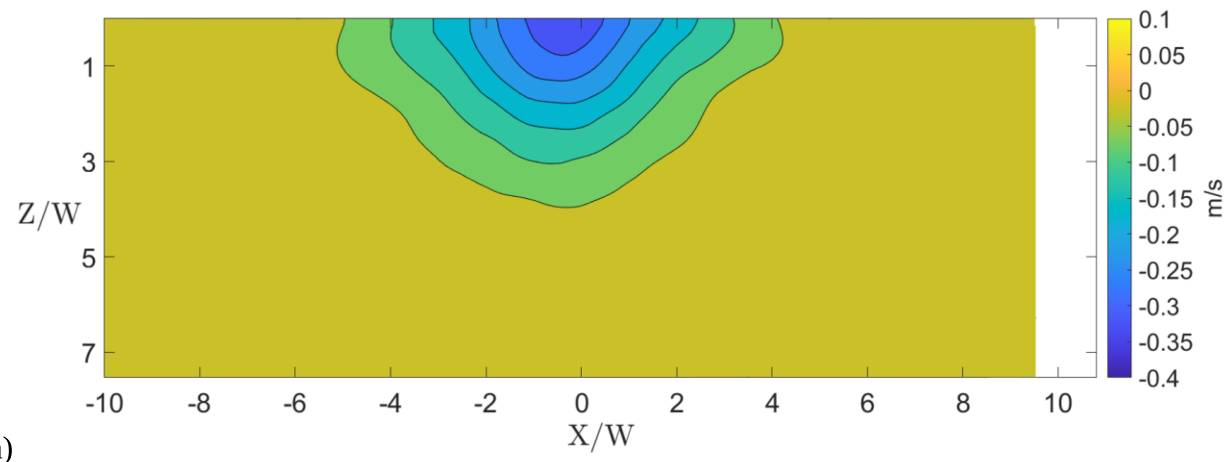

(a)

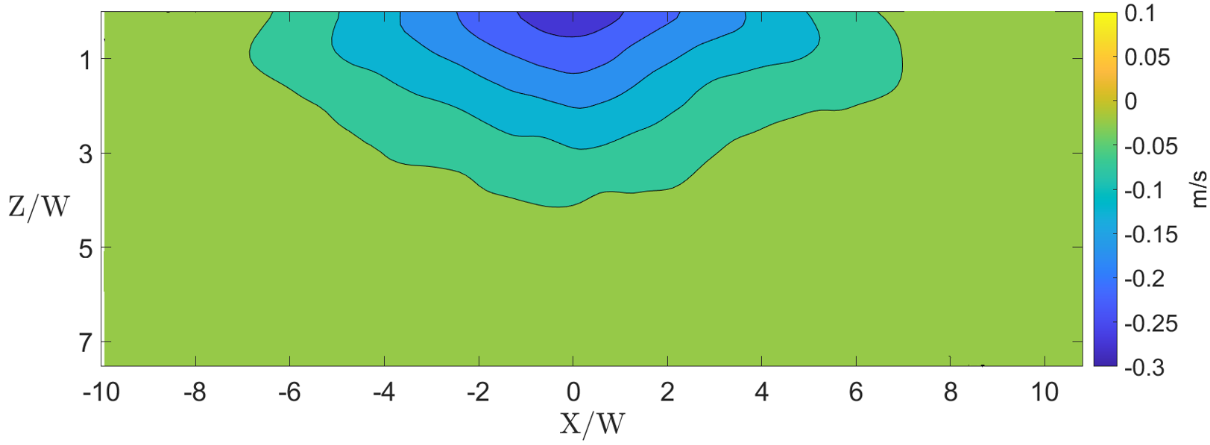

(b)

Figure A.2 Average jet velocity distribution perpendicular to jet axis at (a) section C-C (ΔZ=21.6W) (b) section D-D (ΔZ=29W)

Results shown in Figure A.2 are the average values of 700 measurements in 17.5 s with the frequency of 40 *Hz* which shows two secondary currents on either side of the jet axis. By averaging over smaller periods of time such as 0.25 s, eddies appear in the vector distribution. Figure A.3shows the average of 10 measurements with 0.25 s time difference. Eddies' movements are clear by comparison between Figure A.3(a) and (b) in the same direction as the jet expansion. Some eddies exist at the bottom of the jet which have been eliminated by averaging over the longer time.

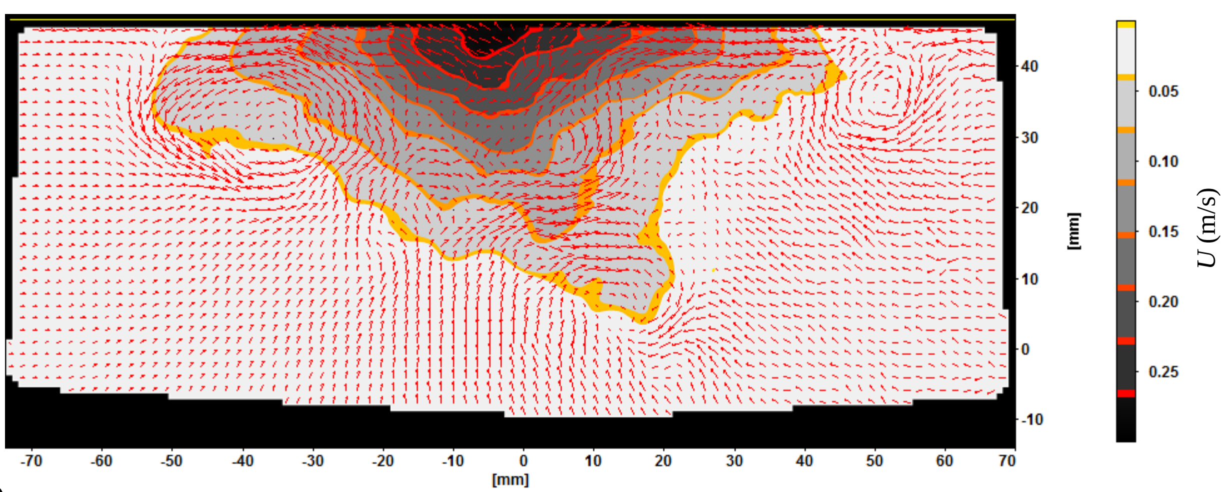

(a)

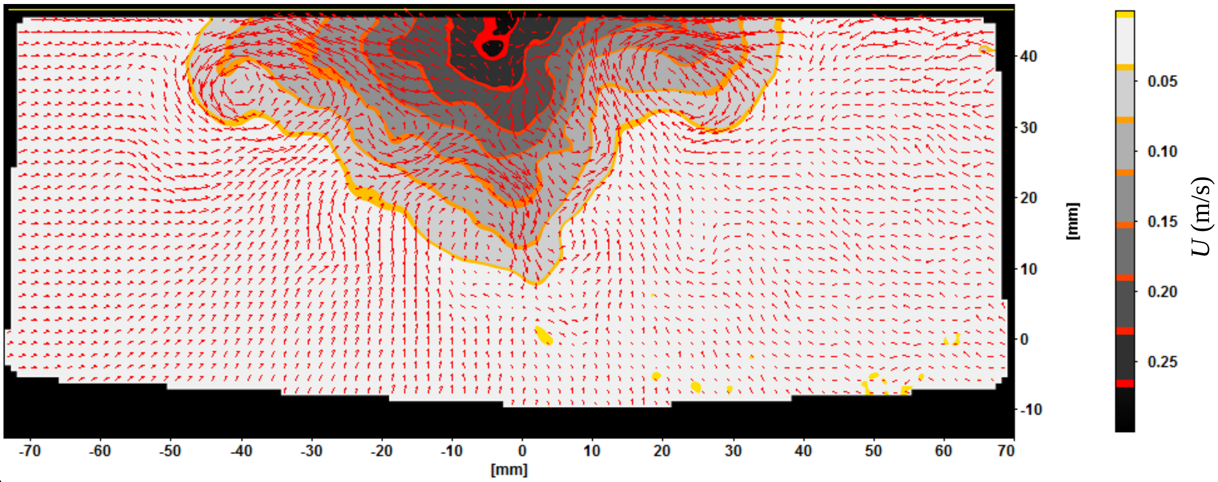

(b)

Figure A.3 Velocity distribution for the average of 10 consecutive measurements (a) measurements number 150 to 160 and (b) measurements number 160 to 170 and

Discharged jet expanded in the area with higher velocity and consequently in-plane velocity components indicated the expansion of the jet (moving away from the jet axis). On the other hand, jet flow created an entrainment which moved the ambient water towards the jet. Where these flows collide, a ripple in the water surface appears and a portion of the flow also moves downward which is shown by yellow contours in Figure A.4 (b). This may be the main reason for the existence of the counter-rotating vortex pair observed in Figure A.5.

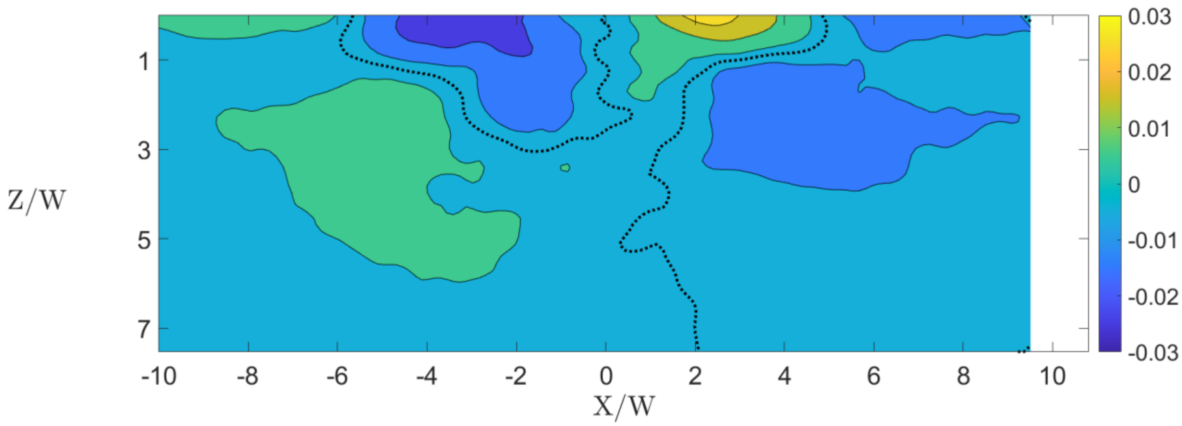

(a)

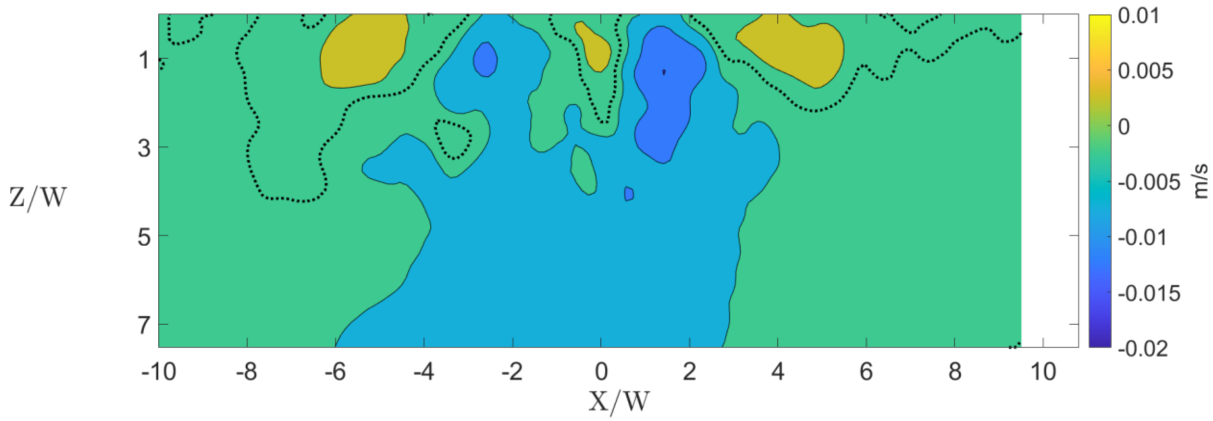

(b)

Figure A.4 The averaged velocity distributions at section C-C perpendicular to jet axis (ΔZ=21W): (a) velocity distribution in X direction and (b) velocity distribution in Z direction

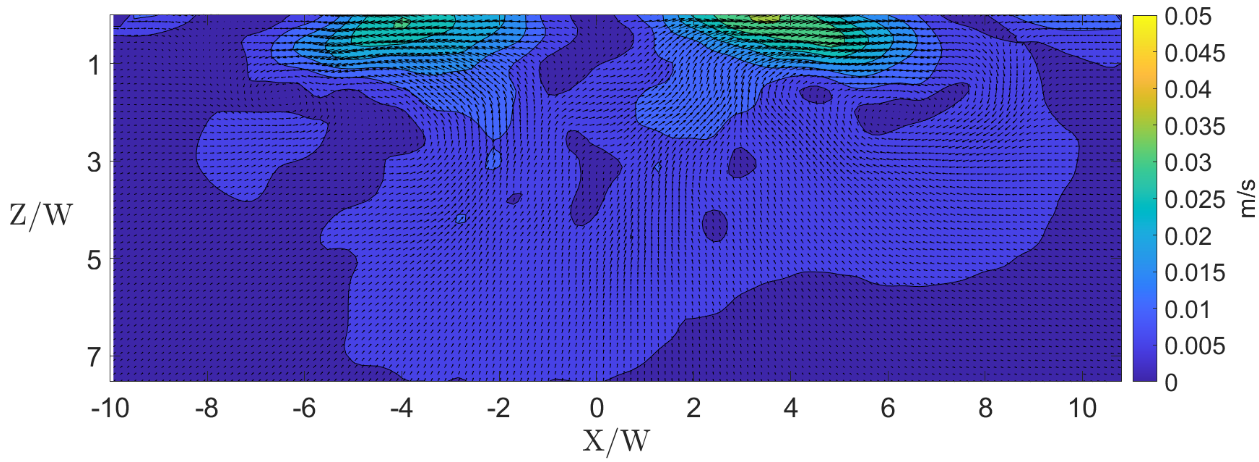

Figure A.5 The average in-plane velocity vectors with magnitude in the background at ΔZ=21.6W

Figure A.6(a) shows the Gaussian distribution of the velocity in 3D, perpendicular to the plane and half-Gaussian distribution in the vertical direction. Velocity vector arrows shown in Figure A.6 (a), shows the angle at which the jet is expanding.

(a)

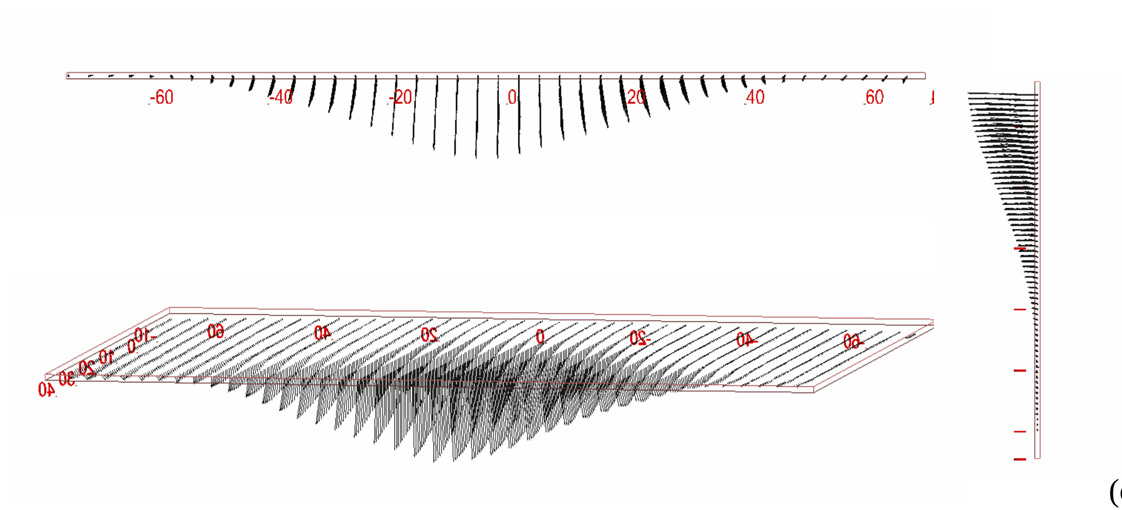

(b) (c)

Figure A.6 3D velocity distribution extracted from Stereo-PIV measurements C-C perpendicular to jet axis (ΔZ=21.6W)

A.2 Numerical Modelling Details

A common approach in dealing with free surface is to consider it as a rigid surface. However, this has been mostly in the studies of submerged jet that oscillations in the water surface have minimal effects on the jet structure and the mixing phenomenon. Here, two approaches were considered to investigate the effects of free surface in simulating the behavior of surface jets. First, *twoLiquidMixingFoam* solver in OpenFoam was used for the mixing of the non-buoyant jet in stagnant water. Second, *interMixingFoam* solver in OpenFoam, was used to study the effects of the free surface of water. Model domains for these two scenarios are shown in Figure A.7.

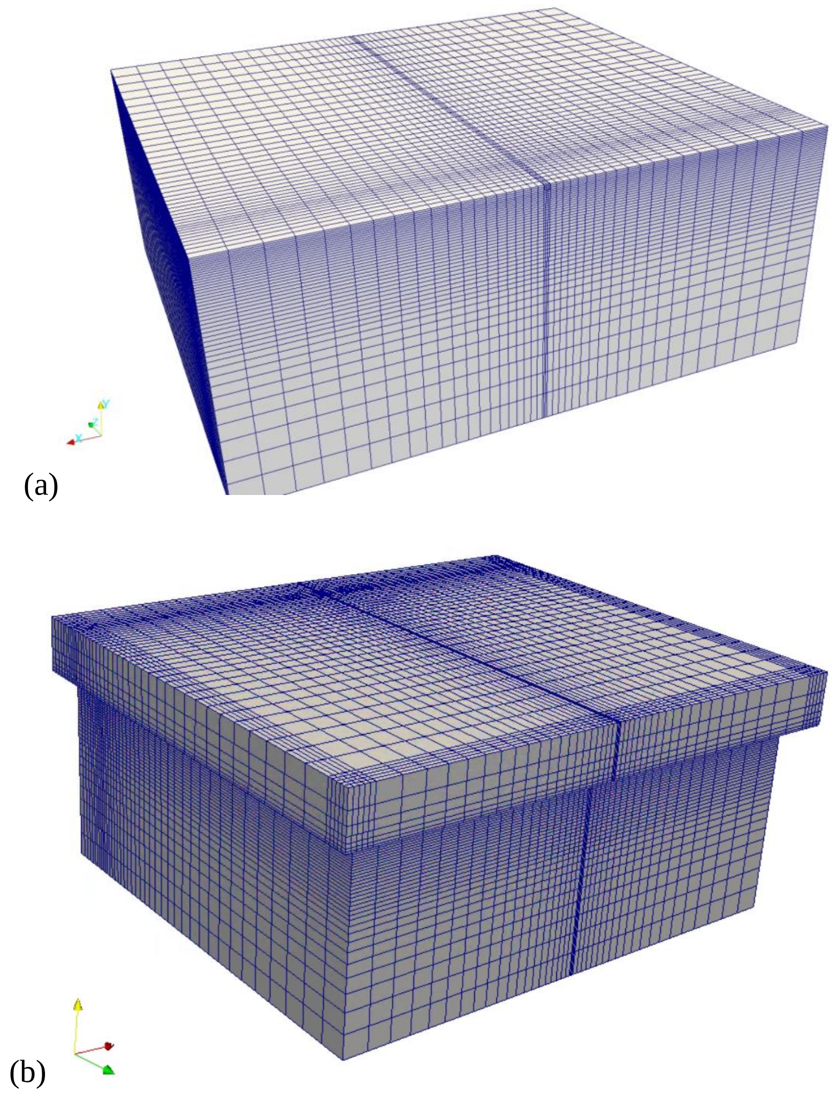

Figure A.7 Mesh cells in the geometry of jets in stagnant water

A.2.2 Preliminary Results

Preliminary modelling results shown in Figure A.8. A different instantaneous velocity magnitude distribution is shown as a results of air movement on top of nozzle exit for the case with free surface.

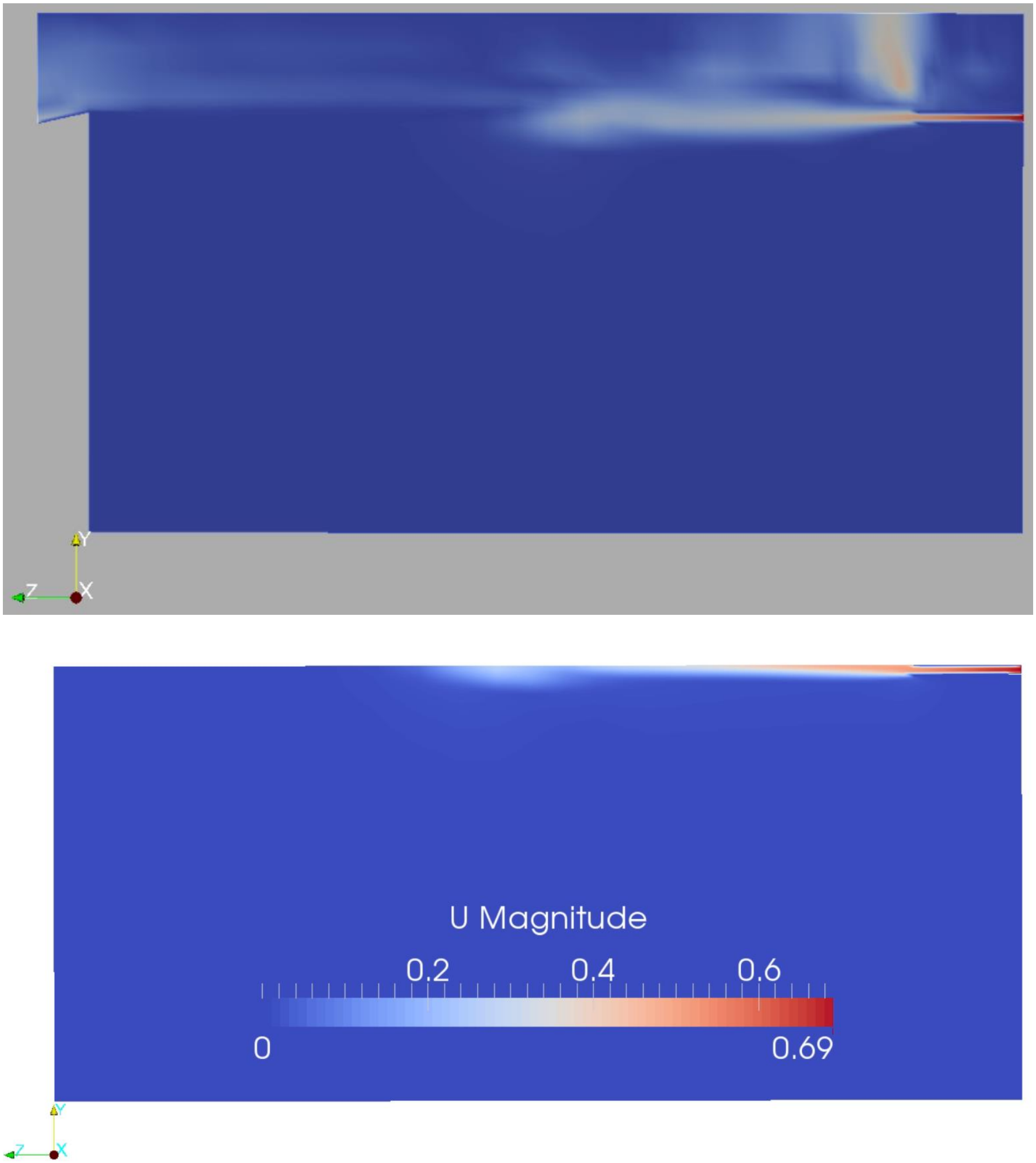

Figure A.8 Instantaneous velocity magnitude at time $t = 2.5\ s$ for (a) rigid surface; (b) free surface

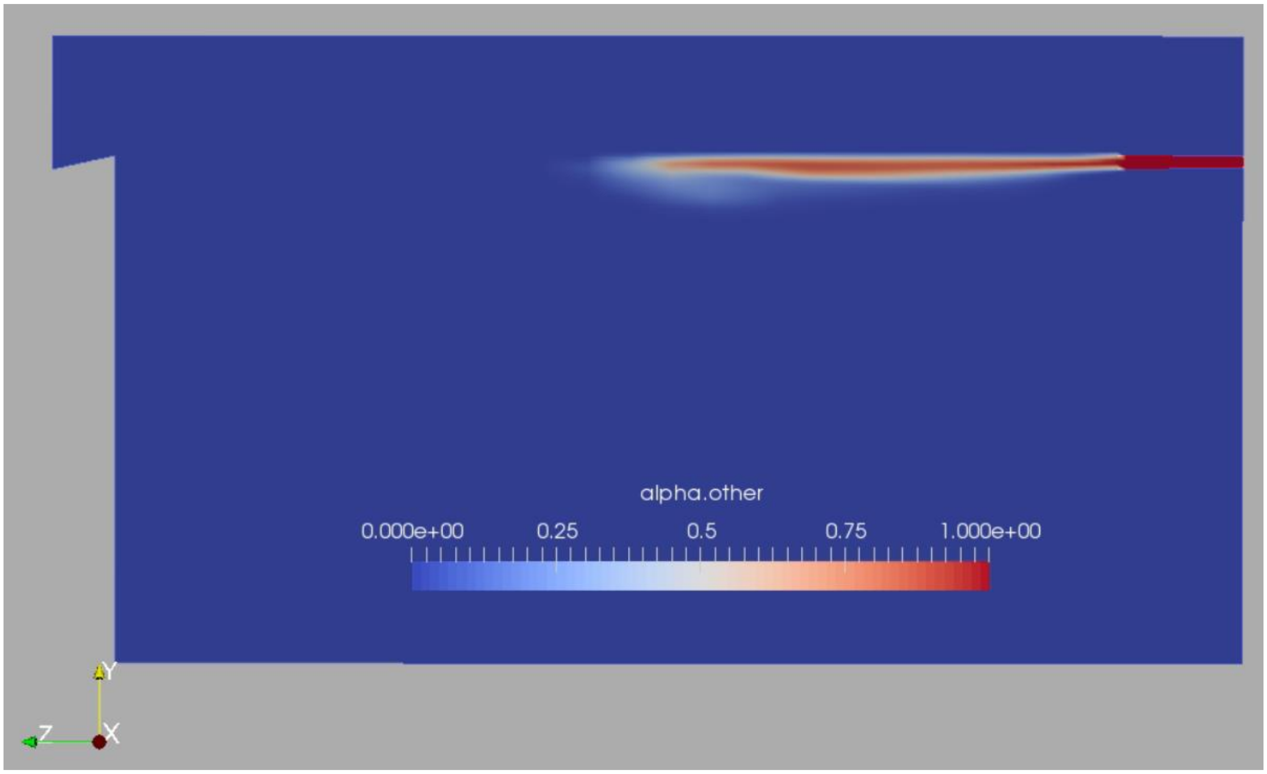

Figure A.9 Instantaneous jet concentration value at time $t = 2.5\ s$ for (a) rigid surface

A.3 Summary

Preliminary conclusions for this case can be summarized as:

- Experimental measurements captured the entrainment zone and expansion zone of the surface jets in stagnant water.
- A counter-rotating vortex pairs generated by the surface jet were observed in the experimental results.
- Gaussian distribution in horizontal plane and half Gaussian distribution in vertical plane are observed in the captured data.